POLITECNICO DI TORINO

SCUOLA DI DOTTORATO

DOTTORATO IN FISICA XXVIII CICLO

Physical behaviour and properties at the first order phase transition of magnetocaloric materials

Cecilia Bennati

Tutori:
Prof. Gianluca Ghigo
Dott. Vittorio Basso

Coordinatore di dottorato:
Prof. Arianna Montorsi

Tesi di dottorato

Febbraio 2015

“Nullum magnum ingenium sine mixtura dementiae fuit.”

Lucio Anneo Seneca

Abstract

This Ph.D. project was mainly devoted to the study of the connection between magnetocaloric properties and first order phase transitions in ferromagnetic materials based on the La(Fe,Si)$_{13}$ compound. The magneto caloric effect (MCE) and its application in magnetic cooling cycles rely on the reversible magnetization and demagnetization of a magnetic material by an external magnetic field, resulting in a temperature change that is maximal at temperatures close to a magnetic phase transition. The possibility to improve the performance of the active refrigerator materials, depends on many factors: the need of a Curie temperature close to ambient temperature, a low magnetic and thermal hysteresis and a high magnetic entropy variation for magnetic fields below two Tesla. The latter requisite can be found in first order magnetic phase transitions that, unfortunately, are accompanied by intrinsic thermo-magnetic hysteresis. This drawback for magneto cooling cycles, motivates the present study on the phase transitions kinetics. On the other hand, the investigation of magneto-thermal phenomena in magnetic materials is of great importance also for solving fundamental problems of magnetism and solid state physics, for example, it is recognised that the properties of interest of such functional materials are intimately linked to the detailed nanostructure, however, the nature of this link itself is not understood very often.

In this Ph.D. project, thermo-magnetic phase transitions in La(Fe,Si)$_{13}$ compounds were investigated through the comparison of various experimental techniques within a collaboration between the applied superconductivity group of Politecnico of Torino and the electromagnetism division of INRiM (National Institute of Metrological Research). To achieve a proper physical understanding of the connection between thermo-magnetic hysteresis at the microscopic level and the microstructure, a magneto optical method was applied to samples of La(FeSi)$_{13}$ with cobalt substitutions, so to allow the dynamical visualisation of the phase boundaries motion in a first order phase transition. These type of experiments have been compared with low rate calorimetry data and, from the experimental work, it has been found that the presence of avalanches is a characteristic feature of these alloys and it is related to their thermal hysteresis. The difference between first and second order phase transition kinetics were highlighted thanks to the employment of different techniques, which also favoured the separation of the general aspects of hysteresis, common to all irreversible processes, from features more strictly dependent on specific microstructural properties. For the aim of this Ph.D., other techniques were also used to observe temperature induced magnetic phase transitions in functional magnetic materials. Among them an in-temperature ferromagnetic resonance method was implemented for the study of the magnetization dynamics in canted spin structures.

The present research activity has been partially related to the European Project DRREAM [1] (a collaborative research project funded by the EC under the Seventh Framework Program 2013-2015), whose goal is to reduce the use of rare earth elements in the life cycle of technologies that use magnetic phase change materials, in particular magnetic refrigerators.

Acknowledgements

I aim to thank the applied superconductivity group of Politecnico of Torino in the person of Gianluca Ghigo, my Ph.D. supervisor, Laura Gozzelino, Francesco Laviano and Roberto Gerbaldo, for the opportunity to experience such intense research activities; the INRiM electromagnetism division, for the great collaboration and the possibility offered to me to improve my skills by exploring many experimental techniques with curiosity and with the help of many people, Elena Olivetti, Luca Martino, Marco Coisson, Michaela Kuepferling, Gianfranco Durin and Massimo Pasquale. In particular I want to thank Vittorio Basso, for his fundamental advices and for sharing his passion for physics, which strongly motivated my work. My Ph.D. wouldn't have been the same without the unique support of Sara, Ambra, Wendy and Carmen and many other people I met during this years at Politecnico and at INRiM, in particular Andrea for his strong support and practical advices. Because many of them would not understand this thesis, I especially thank Antonio, Mariella, Alessandro, Eli, Manu, Ila, Giulia, Johanna and David, Serena, Franz, my family in Torino and my every year wider family of Genova, who just appreciate and support my work without questions…

Contents

...to my uncle and to my aunt.

1

Introduction

MAGNETOCALORIC EFFECT AND ITS APPLICATION

The study of the magnetocaloric effect (MCE) is nowadays an interesting example of collaboration between industry and university. The physical reason which makes MCE attractive either for applications and for research is the existence of thermodynamic relations among the magnetisation change of a system and its temperature, that, in some cases, can be used to perform efficient thermodynamic cycles. With about 60 prototypes [2] [3] [4] being developed all over the world, and the involvement of different industries, magnetocaloric energy conversion is today on its way towards the first market applications [5]: a wine cooler, produced in 2015 [6] is one of the most advanced magnetic refrigerator prototype for room temperature applications. However, in order to obtain such a result, thirty years of dedicate experimental and theoretical research had passed [7]. A promising development of magneto cooling is to develop fully solid state magnetic refrigeration devices, combining the use of materials displaying the magnetocaloric effect and materials whose thermal conductivities are controlled by an external magnetic field [8]. One focus on materials research for MCE is the characterization of the thermodynamic quantities ΔS_{iso} and ΔT_{ad} as a function of an external applied magnetic field. These quantities represent respectively the isothermal entropy change and the adiabatic temperature change of a system when subjected to an external magnetic field. Several magnetic materials, which can produce large temperature changes, are thus subjected to intensive studies in order to improve their performances. This is attested by the large number of publications devoted to describe, through advance material engineering, the MCE properties of various classes of magnetic systems (see Fig.1.1): Heusler alloys [9], rare-earth based compounds [10] , Fe-Rh [11],... A drastic improvement on such materials research was achieved by the discovery of the giant MCE (GMCE) in $Gd_5(Si_2Ge_2)$ in 1997 [12]. It was shown that the change from orthorhombic to a monoclinic structure brings about a fundamental difference in the magnetic behaviour of this alloy.

According to this paradigm, among the promising candidates for magnetic cooling applications, those which have a magneto-structural phase transition of the first order [13] are believed to be the most interesting and are the most investigated one. The research interest on such systems is mainly due to their large (giant) MCE properties at the transition, but noteworthy these compounds represent a playground for study the interplay between spins, electrons and phonons in complex systems.

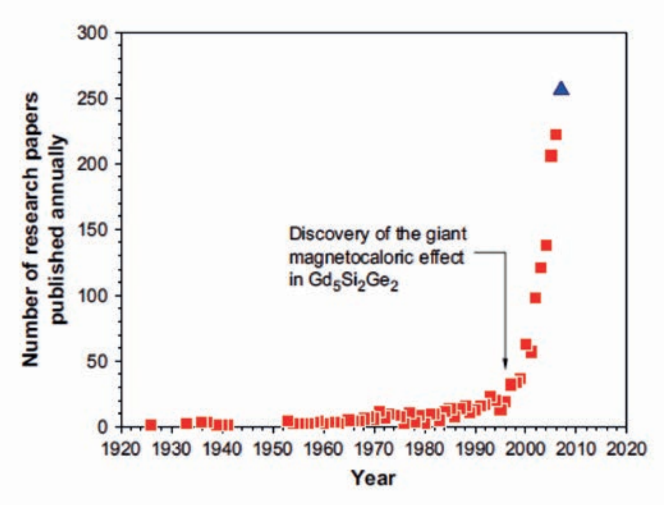

FIGURE 1.1: The number of research papers published annually over the past 80 years containing the word *magnetocaloric* in the title, abstract, or among the keywords [7].

FIRST ORDER MAGNETIC PHASE TRANSITION AS A REQUIREMENT

Thermodynamics provides a fundamental approach for the study of phase transitions [14] setting up relations among different parameters characterizing a systems at equilibrium; however, when the interest is devoted to first order phase transitions, the equilibrium vanishes and the experimental behaviour of a material may result difficult to study. The physical changes, which accompany these transitions, involve discontinuities in the electronic, magnetic and/or crystal structure and these three subsystems can either behave independently or not. Different approaches may have to be considered and, in some cases, the complex mechanisms of interactions at the microscale cannot be disregarded at all. A first order phase transition can thus be studied by comparing initial and final states, so that to highlight differences among physical properties of the two facing phases (electrical resistivity, magnetization, bulk and elastic moduli,...). In fact, the changes in the electronic, magnetic and crystal structure at the transition, originate entropic terms with different signs and magnitudes depending on the order types of the two phases. In some cases these entropy terms are coupled as, for example, in magneto-elastic processes for which the magnetic interaction strongly depend on the distance between atoms [15], thus that more subsystems contribute to the transition. The driving force of a first order phase transition can also be studied by looking at the transition kinetics, which concerns those mechanism by which a system attempts to reach the equilibrium state and how long does it takes. In analogy with a chemical reaction, the phase transformation is regarded as an activation process over an energy barrier (activated state) which separates two equilibrium states (phases). This construction is applicable to systems in transition from non equilibrium to equilibrium, or between two equilibrium states. Importantly, the kinetics factors which govern the transition, determines the velocity of the process, thus how fast or slow a transition can occur and, together with the thermodynamic observations, can furnish the details on the way on which a material reacts to external constrains. One of the most important challenge concerning first order phase transitions and thus GMCE compounds, is to understand the microscopic origin of the existing relation between spins, electrons and phonons, because it represents an opportunity to improve the functional properties of the materials.

With the aforementioned considerations, in order to understand the MCE origin in the details and successfully applied it to room temperature refrigeration cycles, a general discussion on the thermodynamic properties of phase transitions has to be applied to the magnetic / magnetocaloric systems under investigation [14]. The phase equilibrium diagram of the compounds needs to be constructed with attention, in order to improve the possibility to establish material classes with a tunable Curie temperature around room temperature. In fact, to efficiently employ different materials in different cross sections of an active magnetic regenerator, their Curie temperatures have to be close enough to each other and the changes in temperature produced at the transitions have to be sufficiently large for the purpose of refrigeration. Another requirement, which is important for magneto cooling application, is the absence of thermal hysteresis or its limited span, because in this sense, a first order phase transitions is in conflict with an efficient employment of the material. Since refrigeration devices may be cycled at a frequency of a few Hz, the active materials ability to perform the transition at these frequencies has to be checked by using theoretical and experimental investigations of the transition kinetics.

THE CHOICE OF LA(FE,SI)$_{13}$ BASED COMPOUNDS

With the purpose to understand such complexity and, in particular, the kinetics of first order phase transitions, this Ph.D. thesis aims at the investigation of a class of compounds based on the La(Fe,Si)$_{13}$ system. These materials posses a first order or a second order magneto-structural transition from a low temperature ferromagnetic phase to a high temperature paramagnetic phase, depending on the substitution elements at Fe sites and on the external applied magnetic fields. The main reason of interest for this class of compound was highlighted by the pioneering paper of Fujita [16] in 1999, on the presence of very large magneto caloric effect coupled with small thermal and magnetic hysteresis [17] [18] [19]. The last feature has been strongly investigated in the last decades and good results have been obtained to reduce the hysteresis by changing sample geometry [20], micro-structure [21] or preparation route [22]. Meanwhile, many research groups have focused their attention on the mechanism which underlays the origin of the hysteresis at the phase transition but, due to the complexity of the system, a complete picture of the predicted interaction between spin, lattice [23] and itinerant electrons [24] is still reason of debate [25], deserving further investigation.

Experimental investigation

In the thesis, in Ch.2, the classical thermodynamics of equilibrium systems is reviewed briefly and then applied to second or first order phase transitions between equilibrium states. The case of magnetic materials is treated separately, with the aim to introduce the necessary thermodynamic quantities suitable for La(Fe,Si)$_{13}$ based materials. A deeper description of these compounds is furnished on the basis of several theoretical and experimental works and with attention to the role of substitution and interstitial elements and to the intrinsic or extrinsic sources of hysteresis. Concerning the thermo-magnetic hysteresis and the first order nature of the phase transition, few kinetics studies are present in literature on these compounds, thus to motivate the experimental work, presented in Chs.4 and 5. Two different techniques, magneto optics and calorimetry, have been respectively used to observe and to quantify the avalanches of the first order phase transition of La(Fe,Si)$_{13}$ based compounds.

SPATIAL PROPAGATION OF THE TRANSITION FRONT

The use of a magneto optical imaging technique with indicator film (MOIF) [26] for visualize the first order phase transition in La(Fe$_{0.9}$Co$_{0.015}$Si$_{0.085}$)$_{13}$ is presented in Ch.4. The experimental setup in use and its physical principle are described in details. The MOIF technique permits to directly observe the magnetic response of a magnetized object and thus to dynamically follow the magnetic phase front across an entire surface of a sample, without loosing micro-scale resolution on single sites. The emerging aspect of this work discloses that the magnetic front propagation is reproducible while cycling the material across its transition temperature. The first order nature of the process produces fast and discontinuous transformations of volumes inside the bulk material, which interestingly are counteracted by the presence of a concomitant slow phase front motion. MOIF technique has been also used to clarify some aspects related to the local properties of the compound. Local inhomogeneities present at the surface of the sample (and observable by MOIF) are in fact slightly related to the aforementioned slow dynamics. The magneto-optical observations are compared to several calorimetric data presented in Ch.5.

LOW RATE CALORIMETRY AND AVALANCHES

A characteristic feature of first order phase transitions is the presence of an intrinsic latent heat of transformation, decoupled from the continuous variation in the specific heat of a material. Calorimetry techniques have been employed to observe this property, either in first and second order phase transitions. The samples suitable for this purpose were chosen from a series of LaFe$_x$Mn$_y$Si$_z$-H$_{1.65}$ compounds, which differ to each other mainly because of the amount of Mn atoms. The MCE properties of the series [27] were studied in order to obtain a complete phase diagram around room temperature as a function of external applied fields below two Tesla. On the other hand, the samples were also used to obtain more details about the interplay of the reversible specific heat and the characteristic latent heat under different external conditions. In the chapter, a wide motivation for the use of very low temperature scanning rate (1 mK/s) is furnished. Under such condition, it is shown that heat flux avalanches can be resolved in time when the transitions are of the first order and that the existence of such avalanches discriminates between possible irreversible and reversible contributions to the entropy change at the transition. The emerging aspect of this study is the coexistence of either latent heat and reversible heat which appears when approaching the critical point on the magnetic phase diagram of the compound.

PERSPECTIVES

A kinetic approach is showed to be necessary to explain the fast dynamics of the front motion observed by MOIF and the avalanche behaviour obtained by DSC experiments. The thermodynamics of equilibrium it is however used to explain the remaining properties of such transitions: the slower propagation of the front and the rising specific heat of the materials while approaching the critical point. The results of this experimental work may help to model the details of phase transitions in La(Fe,Si)$_{13}$ based compounds and to optimize their properties for magneto cooling applications. Moreover, since the experiments concern general features of phase transitions near the critical point, they may also be applied to other systems in the future. In Ch.6, other experimental techniques are applied to magnetic phase transitions. The reported results provide the basis for future experimental investigations either in bulk or in thin film samples, including the possibility to observe the evolution of the magnetization dynamics with temperature.

2

Thermodynamics of a phase transition

> "̧Classical thermodynamics is built around the concept of equilibrium states. If we leave a system undisturbed, it relaxes to an apparently quiescent state in which nothing much seems to be happening. From the late nineteenth century through much of the twentieth century, a comprehensive theoretical framework — informed by ever more precise experiments — was developed to explain how the macroscopic properties of these equilibrium states arise from interactions between their microscopic constituents [28].

This chapter is focused on the properties of a thermodynamic system and in particular to magnetic systems treated as composed by magnetic moments (spins), whose order is used to define the phase of the system. Considerations about the thermodynamic response of a magnetic system are extended to the case in which a change of phase is induced. Each phase of the system is regarded as a (meta)stable state, in which the equilibrium conditions of the classical thermodynamic determine the equation of state. By comparing these quantities for each phase, the related functional properties of the system can be studied during a phase transition.

2.1 Thermodynamics of equilibrium

All thermodynamic systems have a tendency to evolve toward equilibrium states, where they are characterized solely by the actual value of the state variables and not by the previous history. These states are by definition time independent and are in a stable thermodynamic equilibrium [14]. On the basis of that, a phase can be defined as a thermodynamic system (a physically distinct region of a system) which has attained thermodynamic equilibrium, and which has a specific set of order parameters which specify its physical properties. Such parameters can describe the composition, the structure, the atomic, magnetic and ferroelectric order, etc. However, the term phase is also frequently referred to a set of equilibrium states demarcated in terms of state variables such as pressure and temperature by a phase boundary on a phase diagram. For any system at equilibrium may exist an equation of state which relates the different thermodynamic state variables to each other. Such equation of states can be complex as far the interactions among the constituent elements of a system and the solution can be not easy to find.

2.1.1 Thermodynamic potentials

In order to describe a phase at equilibrium, a definition of its energy is required. In general, a thermodynamic system is described by its internal energy, U. Since only differences in energy rather then absolute values of energies have physical significance, it follows that the internal energy of a system can be only defined referring to the energy of the system in a confidential state arbitrary taken at zero value. On the basis of that, the internal energy might be thought as the energy required to create a system in the absence of changes in temperature or volume (adiabatic process). U represents the energy contained within the system, excluding the kinetic energy of motion of the whole system and the potential energy due to external force fields, but it keeps account of the gains and losses of energy of the system that are due to changes in its internal state. In a system which is a function of volume,V, pressure, p, and temperature, T, the Gibbs free energy of a system is used to represent the sum over different contributions of energies and can be defined as:

$$G = U - TS + pV, \tag{2.1}$$

where S denotes the entropy of the system. It has to be noted that, if the system is controlled at constant temperature and pressure, the sum over all contributions of the energy, G, is minimum at thermodynamic equilibrium where an equation of state holds. Other thermodynamic potentials can be used to describe a system, each of them describing a characteristic feature. The enthalpy, E, is useful in order to determine the heat absorbed (or released) by the system through a chemical reaction or by external heat transfer and is defined as:

$$E = E(S, p) = U + pV. \tag{2.2}$$

Finally, as in the case of the internal energy, the Helmholtz free energy can be used to define the amount of work obtainable from a system:

$$A = A(T, V) = U - TS \tag{2.3}$$

A mnemonic scheme of the existing relations among variables and state functions is represented in Fig.2.1. On each side of the square appears one of the thermodynamic potential, surrounded by its two natural independent state variables. An arrow pointing toward a thermodynamic potential has to be substituted by a negative coefficient (and vice-versa). The above definition holds

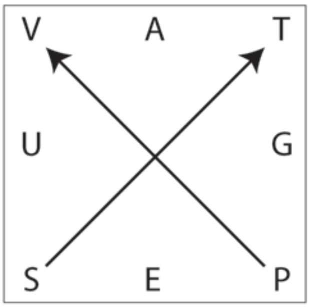

FIGURE 2.1: The thermodynamic square for a pVT system.

for a system which has a constant number of molecules, thus the chemical potential is fixed. In certain circumstance the work obtainable from a macroscopic system is related to the change in the appropriately defined thermodynamic potential, thus each of them may be differentiated resulting in a set of fundamental equations:

$$dU = TdS - pdV, \tag{2.4}$$

$$dE = TdS + Vdp, \tag{2.5}$$

$$dG = -SdT + Vdp, \tag{2.6}$$

$$dA = -SdT - pdV, \tag{2.7}$$

By the use of these definitions, the internal parameters S, p, T and V can be determined by the following equations of state, where the subscript, in each partial derivative, refers to the thermodynamic variable which is kept constant during a process.:

$$T = \left(\frac{\partial U}{\partial S}\right)_V ; -p = \left(\frac{\partial U}{\partial V}\right)_S \tag{2.8}$$

$$T = \left(\frac{\partial E}{\partial S}\right)_p ; V = \left(\frac{\partial E}{\partial p}\right)_S \tag{2.9}$$

$$-S = \left(\frac{\partial G}{\partial T}\right)_p ; V = \left(\frac{\partial G}{\partial p}\right)_T \tag{2.10}$$

$$-S = \left(\frac{\partial A}{\partial T}\right)_V ; -p = \left(\frac{\partial A}{\partial V}\right)_T \tag{2.11}$$

2.1.2 Maxwell relations

From the above considerations it is evident that, in spite of the complexity of a given system (microscopic behaviour), thermodynamics is able to capture some of the features which concern the dynamics inside a rigid body subjected to constrains or force. Moreover, by making use of the second derivative of the state functions described above, it is possible to obtain the Maxwell relations: a set of useful equations which trace the relation among the different thermodynamic variables (internal parameters) of the system. For a pVT system these are:

$$\left(\frac{\partial T}{\partial V}\right)_S = -\left(\frac{\partial p}{\partial S}\right)_V , \tag{2.12}$$

$$\left(\frac{\partial T}{\partial p}\right)_S = \left(\frac{\partial V}{\partial S}\right)_p , \tag{2.13}$$

$$\left(\frac{\partial S}{\partial p}\right)_T = -\left(\frac{\partial V}{\partial T}\right)_p , \tag{2.14}$$

$$\left(\frac{\partial S}{\partial V}\right)_T = \left(\frac{\partial p}{\partial T}\right)_V . \tag{2.15}$$

Finally, by crossing the state functions and performing the second derivatives of each thermodynamic potential, two types of response function can be introduced. The specific heats:

$$c_V = T\left(\frac{\partial S}{\partial T}\right)_V = -T\left(\frac{\partial^2 A}{\partial T^2}\right)_V ; \tag{2.16}$$

$$c_p = T\left(\frac{\partial S}{\partial T}\right)_p = -T\left(\frac{\partial^2 G}{\partial T^2}\right)_p ; \tag{2.17}$$

which measure the heat absorption from a temperature stimulus and the compressibilities:

$$K_T = -\frac{1}{V}\left(\frac{\partial V}{\partial p}\right)_T = \frac{1}{\rho}\left(\frac{\partial \rho}{\partial p}\right)_T = -\frac{1}{V}\left(\frac{\partial^2 G}{\partial p^2}\right)_T ; \tag{2.18}$$

$$K_S = -\frac{1}{V}\left(\frac{\partial V}{\partial p}\right)_S = \frac{1}{\rho}\left(\frac{\partial \rho}{\partial p}\right)_S = -\frac{1}{V}\left(\frac{\partial^2 E}{\partial p^2}\right)_S \tag{2.19}$$

which measure the response of the volume to a pressure stimulus. A further response function is represented by the thermal expansion coefficient, defined by:

$$\alpha_p = \frac{1}{V}\left(\frac{\partial V}{\partial T}\right)_p . \tag{2.20}$$

2.2 Phase transitions between equilibrium states

For the pVT system of the previous examples, the equation of states define a surface in the pVT three-dimensional space tracing the phase diagram of the system. Each of the points on this surface corresponds to equilibrium positions of the system where it can be described by classical thermodynamics. In order to understand such a surface, it is convenient to consider its projections on to planes. For example, the projection on to the pT plane of a pVT system (Fig.2.2 (a)), reveals three separate regions on the phase diagram. Using water as an example, these regions correspond to its three familiar forms: the solid, the liquid and the gaseous phase. Moreover, this representation implies that the solid and gaseous phase are in equilibrium along the sublimation curve, the solid and liquid phases are in equilibrium along the fusion curve and the liquid and gaseous phases are in equilibrium along the vapour pressure curve. In fact, in each point on these three curves the two phases can coexist while, the triple point represents an equilibrium state in which all three phases coexist. Among these description, the vapour pressure curve, Fig.2.2 (a), does not extend forever but rather it terminates in a point. This point is named the critical point, and its coordinates are denoted by the respective critical values of the parameters p_c and T_c.

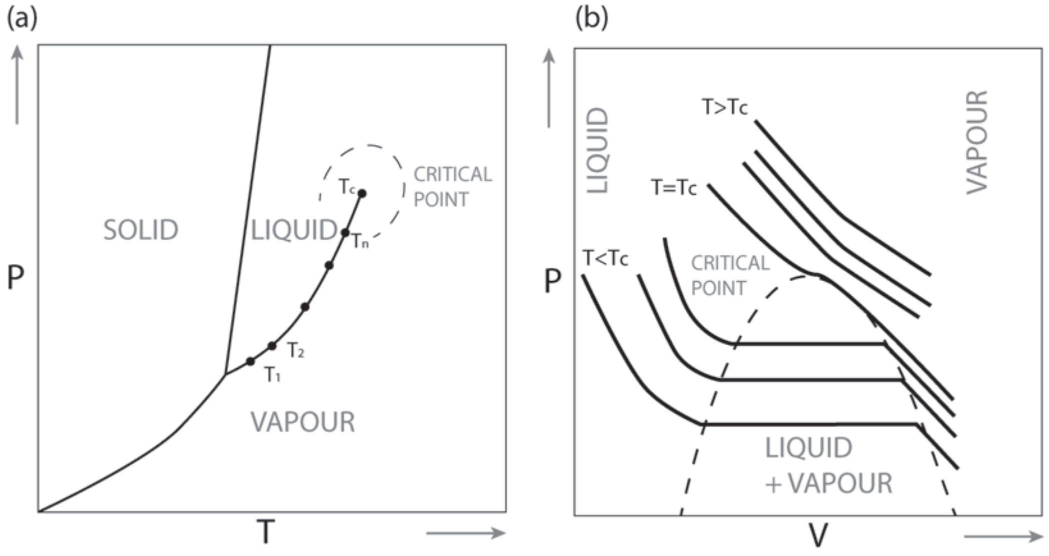

FIGURE 2.2: Projections of the phase diagram for a pVT system. (a) and (b) are respectively the pT and pV projections near the critical point.

The fact that the vapour pressure curve terminates in a critical point means that one can convert a liquid to a gas continuously, without crossing the phase transition line. In this sense, there is no fundamental difference between the liquid and gaseous phase. As it is shown by the isothermal curves in Fig.2.2 (b), at temperature below T_c, the difference in the volumes (density) of the liquid and gaseous phases is large. This difference becomes zero while approaching the critical temperature. The existence of a quantity which is non zero below the critical temperature and zero above it, is a common feature associated with the critical points of a wide variety of physical systems. This quantity represents the order parameter of the system [29].

The order parameter helps to define a phase transition, in fact, for any system, a change of phase occurs when one or more of its order parameters changes discontinuously from one value to another or from zero to a non-zero value (or vice versa). At any phase transition, either if the system is crossing the critical point or a coexistence curve, the Gibbs energies of the two phases are equal. However this condition may not hold for all the thermodynamic variables which govern the equation of state of the two phases. A discontinuity in the order parameter which governs the transition, as it happens for example to the density of water when it crystallizes, produces a discontinuity in the first order derivative of the free energy potential. As a consequences, a phase transition may belong to the first order phase transition class (discontinuous and irreversible process) or to the second order phase transition class (continuous and reversible process).

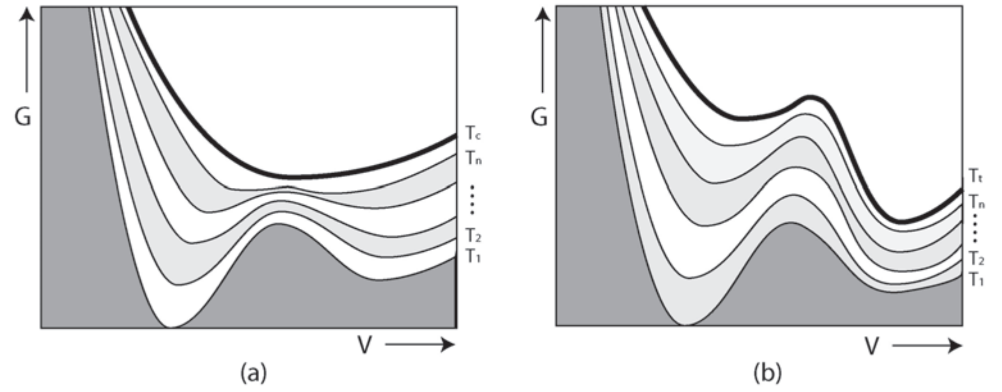

FIGURE 2.3: Schematic representation of the Gibbs free energy as a function of the internal variable V for a PVT system in the vicinity of a second order phase transition (a) and of a first order phase transition (b).

2.2.1 Continuous phase transitions

A plot of the Gibbs free energy as a function of a state variable (p, T, V) in the vicinity of a phase transition can be represented schematically with two equilibrium position separated by a maximum, the two minima representing the two phases which are (meta)stable for a set of pVT values. This representation serves to consider the two phases as different systems, governed by a different equations of state. The existence of a phase transition is explicate by the point in which the relative Gibbs free energy are equal. As it can be observed in Fig.2.3 (a), the volumes of the two phases are different along the isothermal curve labelled with T_1. As the temperature is increased, the curve of the Gibbs energy modifies and the two minima smoothly merge into a single equilibrium minimum. The energy of the two phases thus, by the effect of the temperature, is continuously transformed into a sequence of equilibrium positions, until the critical temperature T_c is reached and the two phases have the same values of

T and V: they are undistinguished and thus governed by a single minimum in the Gibbs free energy. In these cases, at the transition, the specific heats and compressibilities of Eq.(2.16-2.19) are discontinuous.

IMPORTANT PROPERTIES AT A SECOND ORDER PHASE TRANSITION

Since the internal energy U is a function of state, a phase transition can be studied by looking at the difference in the internal energies of the initial and final phase. If a system absorbs an infinitesimal amount of heat dQ during a reversible process, the entropy change of a system is equal to:

$$dQ = TdS. \tag{2.21}$$

It follows that for a reversible transition, i.e. a continuous process, by combining Eqs.(2.4) and (2.21), the difference from the initial and final internal energy is given by:

$$dU = dQ - dW. \tag{2.22}$$

This equation describes the variation of the internal energy of a system, which is due to the exchanged heat of the reversible processes diminished by the work done by the system. For a pVT system the work is due to $-pdV$. The work done during a second order transition is fully reversible.

Considering a system in contact with a heat reservoir during a reversible process, if there is heat Q absorbed by the reservoir at temperature T, the change in entropy of the reservoir is given by:

$$dS_{\text{reservoir}} = -\frac{dQ_{\text{rev}}}{T}. \tag{2.23}$$

The total entropy change of system plus surroundings is

$$dS_{\text{total}} = dS_{\text{system}} + dS_{\text{reservoir}} = 0, \tag{2.24}$$

and this is also true if there is a quantity of heat rejected by the system.

For a second order phase transition, specific heats can be calculated by using Eqs.(2.16) and (2.17). Substituting S with eq.(2.21), the pressure specific heat become:

$$c_P = \left(\frac{\partial Q}{\partial T}\right)_P; \tag{2.25}$$

Such equation can be used to determine the specific heat of phases by measuring the exchanged heat of the transition with calorimetry methods (see Ch.5).

2.2.2 First order phase transitions

In Fig.2.3 (b) is depicted the evolution of the Gibbs potential when the coexistence curve is approached. When the system reaches the transition temperature, T_t, the two equilibrium minima, representing the two phases, remain separated by a maximum which represents a point of instability. Differently from a second order transition, the effect of the rising temperature is to establish which of the two minima is more stable (lower). In these cases, at the transition temperature, the system may prefer to evolve to the more stable configuration, even if a sharp discontinuity in the values of V, with respect to the pVT system, persists. The conditions which help the system to transform in the more stable phase usually involve process at the micro scale level.

IMPORTANT PROPERTIES AT A FIRST ORDER PHASE TRANSITION

The change in internal energy during a first order transition is not necessarily continuous. In these cases, the transition is characterized by a latent heat, which is defined as:

$$L = T\Delta S, \tag{2.26}$$

where T is the temperature of the transition and ΔS is the difference in the entropy of the two phases. Alternatively, the latent heat can be written as the difference in the enthalpies of the two phases:

$$L = \Delta E. \tag{2.27}$$

Since the method by which the transition is induced is irrelevant, the latent heat is independent thereof. As an example, at a pressure of one atmosphere, the liquid-gas transition (boiling) of water occurs at 373.15 K and the latent heat of vaporization is then 2264.76 kJ/kg.

Another consequence of a first order phase transition is the presence of hysteresis. If the system has been transformed once, in order to restore the initial conditions the reverse process will follow a different thermodynamic path, explaining the difference in melting point and freezing point of some substances. Such direction dependence is known as hysteresis. Lastly, at the transition point, specific heats and compressibilities diverge to infinity, since they are calculated from the derivative of a discontinuous function.

A graphical summary of the behaviour of the main thermodynamic quantities at a first or second order phase transition or in the absence of transformation is furnished in Fig.2.4.

2.3 Magnetic systems

The simplest way to describe a magnetic system is by using the degree of order of its constituent spins, therefore magnetic materials can be modelled as systems of spins which can orient themselves in an applied magnetic field. Most solid materials are paramagnetic or diamagnetic. These materials either do not have electron spins or these spins are not ordered unless an external field induces some non-random orientation. Such materials are not considered to have an ordered magnetic structure. This is different for ferro-, ferri- and antiferromagnetic materials, which differ in the relative ordering of their spins within the lattice. In some ferromagnetic cases the structure may be relatively simple in that all spins point in the same direction. Towards higher temperatures

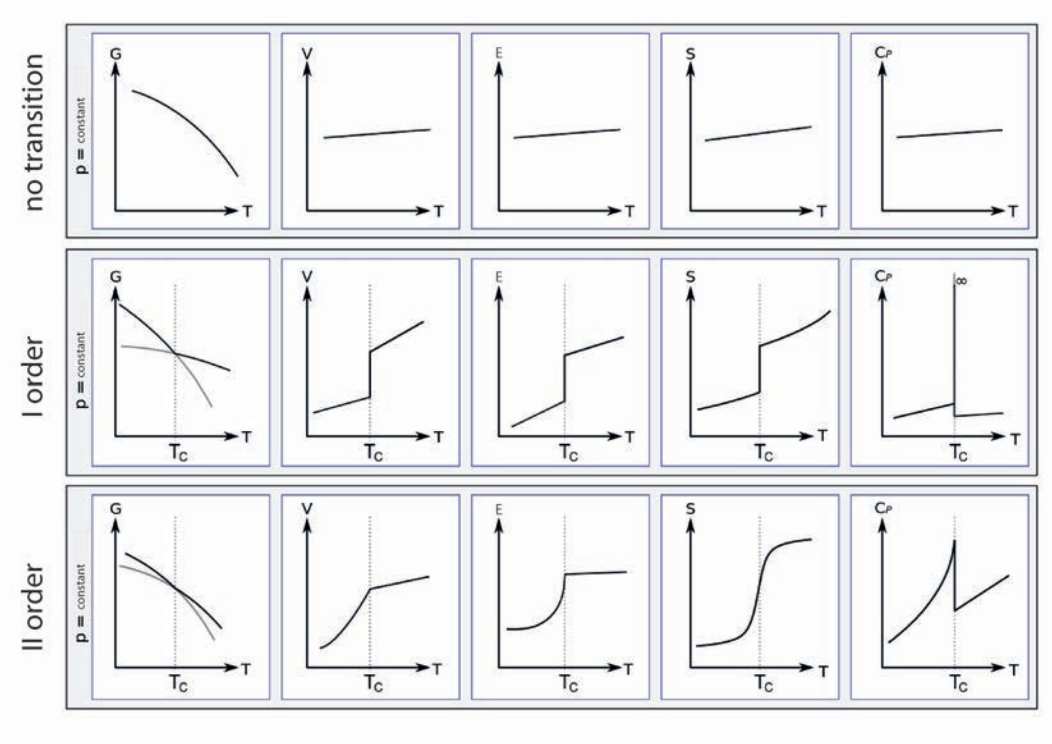

FIGURE 2.4: Summary of the behaviour of the main thermodynamic quantities in a pVT system in the absence of transformation (a), at a first (b) or at a second order phase transition (c).

there will be more and more disordered spins defying the order of the magnetic structure and, at a certain temperature, the order will break down and the spins will point in random directions. In some materials the pattern in which the spins order is much more complicated. In antiferromagnetic materials, contiguous spins point in opposite directions so that the overall magnetic moment is zero. However, this is not necessarily achieved by a simple up and down pattern and complicated structures may arise. Within the lattice, there may be layers in which all spins point in one direction (as in a ferromagnet) but in the next layer they point in the opposite direction giving an overall antiferromagnetic arrangement. The possible number of arrangements is very large and can include spirals, clusters, tetrahedra etc. In the following the discussion will be centred to the case of ferromagnetic order, which vanishes at the Curie temperature, releasing the system in a paramagnetic phase. In a paramagnetic phase the spin disorder is maximum and can be lowered just by applying a magnetic filed. However, is only close to T_c that the spin order can be drastically enhanced by applying an external magnetic field. In these cases, the Curie temperature represents a point at which the magnetic system experience a large change in magnetic order and thus in the magnetic entropy itself.

2.3.1 Analogy between pVT and magnetic systems

The magnetzation M (i.e. the volume or mass density of magnetic moment) is used as the order parameter and serves, in analogy to the density for a classical substance, to defines the phase diagram of a magnetic system. As for the case of a pVT system, it is possible to furnish a thermodynamic description of the macroscopic behaviour of a spin system on the basis of classical thermodynamic of equilibrium. The most used representation of the laws governing a magnetic system at equilibrium, starts from the analogy which can be made between a pVT and a magnetic system. If a pVT system can be represented by its internal variable volume and pressure, by replacing V with M and $-p$ with $\mu_0 H$, the magnetic field, it is possible to write the function of state for a magnetic system. The volume and pressure effects in the present discussion on magnetic system are neglected for simplicity. In the case of a magnetic solid the appropriate intensive variables are thus H and T. The work done by the system, if the applied filed is held constant, is then done by a magnet during a process in which its magnetization is changed:

$$dW = -\mu_0 H dM. \tag{2.28}$$

The function of states for the internal energy, U, the enthalpy, E, the Gibbs free energy, G, and the Helmholtz free energy, A, can be written as density functions:

$$dU = TdS + \mu_0 H dM, \tag{2.29}$$

$$dE = TdS - \mu_0 M dH, \tag{2.30}$$

$$dG = -SdT - \mu_0 M dH, \tag{2.31}$$

$$dA = -SdT + \mu_0 H dM, \tag{2.32}$$

The resulting thermodynamic square for a magnetic system is given in Fig.2.5.

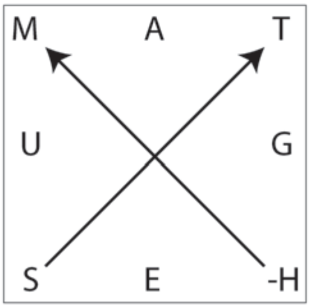

FIGURE 2.5: Thermodynamic square for a magnetic systems [14].

The internal parameters S, M, T and H can be determined by the following equations of state:

$$T = \left(\frac{\partial U}{\partial S}\right)_M ; \mu_0 H = \left(\frac{\partial U}{\partial M}\right)_S \tag{2.33}$$

$$T = \left(\frac{\partial E}{\partial S}\right)_H ; -M = \frac{1}{\mu_0}\left(\frac{\partial E}{\partial H}\right)_S \tag{2.34}$$

$$-S = \left(\frac{\partial G}{\partial T}\right)_H ; -M = \frac{1}{\mu_0}\left(\frac{\partial G}{\partial H}\right)_T \tag{2.35}$$

$$-S = \left(\frac{\partial A}{\partial T}\right)_M ; \mu_0 H = \left(\frac{\partial A}{\partial M}\right)_T \tag{2.36}$$

2.3.2 Maxwell relations

The four Maxwell relations for a magnetic system are:

$$\frac{1}{\mu_0}\left(\frac{\partial T}{\partial M}\right)_S = \left(\frac{\partial H}{\partial S}\right)_M , \tag{2.37}$$

$$\frac{1}{\mu_0}\left(\frac{\partial T}{\partial H}\right)_S = -\left(\frac{\partial M}{\partial S}\right)_H , \tag{2.38}$$

$$\frac{1}{\mu_0}\left(\frac{\partial S}{\partial H}\right)_T = \left(\frac{\partial M}{\partial T}\right)_H , \tag{2.39}$$

$$\frac{1}{\mu_0}\left(\frac{\partial S}{\partial M}\right)_T = -\left(\frac{\partial H}{\partial T}\right)_M , \tag{2.40}$$

whether, the response functions of Eqs.(2.16-2.19) are substituted with the magnetic specific heats at constant magnetization values or applied magnetic field:

$$c_M = T\left(\frac{\partial S}{\partial T}\right)_M , \tag{2.41}$$

$$c_H = T\left(\frac{\partial S}{\partial T}\right)_H . \tag{2.42}$$

The compressibilities are replaced by the isothermal and the adiabatic susceptibilities, which takes into account for the change in magnetic order in response to an applied magnetic field.

$$\chi_T = \left(\frac{\partial M}{\partial H}\right)_T \tag{2.43}$$

$$\chi_S = \left(\frac{\partial M}{\partial H}\right)_s \tag{2.44}$$

2.3.3 Magnetic phase transitions

As mentioned before, a change in the magnetic order is accompanied by a consequent variation of the spin entropy. This effect can be obtained by varying the external constrains H and T and forcing the system toward a different magnetic equilibrium state. A magnetic phase diagram can thus be visualized by the projection of the equilibrium surface on MT and HT planes. In Fig.2.6 (a) the ferromagnetic and paramagnetic states are considered near the critical point, i.e. the Curie temperature. Above T_c the system is paramagnetic and the external field can just slightly order the spins. Below T_c, the system is ferromagnetic and H improves the order of the spontaneous magnetization. In Fig.2.6 (b), the order parameter M, is represented as a function of T. Again, there exists the critical temperature (Curie point) at which the PM phase is established. The magnetic order, in this representation, continuously decreases while increasing T. This scheme is suitable for a second order phase transition and can be successfully described by mean field theory models.

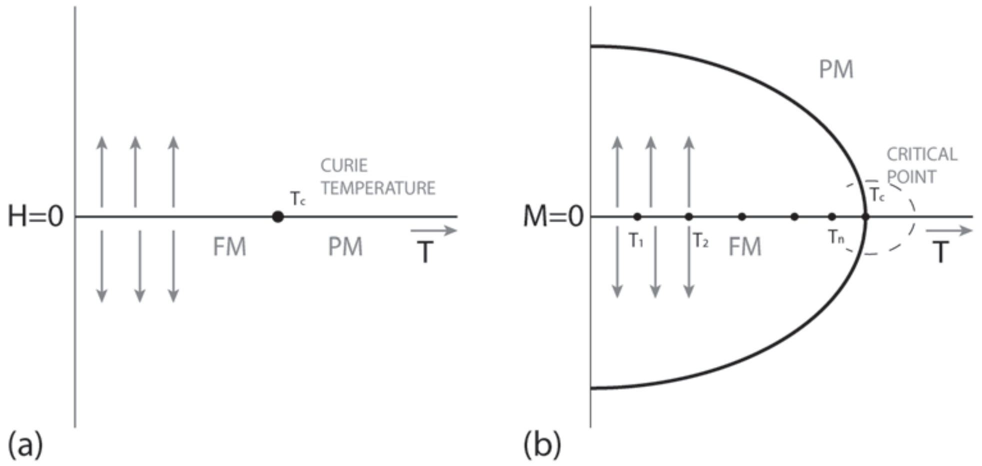

FIGURE 2.6: (a) Scheme of the projection of the HT plane of a ferromagnetic system near the second order phase transition (Curie temperature, T_c). (b) Analogue MT projection plane of the phase diagram.

The specific heats at the transition, are derived from the second order derivative of the free energy by making use of Eqs.(2.41) and (2.42) which show that c_p of a ferromagnet is greater than that of a non ferromagnet and goes through a maximum at the Curie temperature. When heat is added to any metal, part of it increases the amplitude of thermal vibration of the atoms (lattice specific heat), while the remaining increases the kinetic energy of the valence electrons (electronic specific heat). If the metal is ferromagnetic, additional heat is required to disorder the spins (magnetic specific heat). The number of spins disordered per degree increases with the temperature in accordance with the appropriate Brillouin function, and becomes very large just below the Curie temperature, where the magnetization is decreasing precipitously. According to the mean field approximation, the heat capacity change at $T = T_c$ can be presented as:

$$\Delta c_M = Nk_B \frac{5J(J+1)}{J^2 + (J+1)^2}. \tag{2.45}$$

where J is the quantum number of the total angular momentum. It follows that c_M rapidly increases with J increasing, approaching the upper limit of 5 $Nk_B/2$ (for example, the c_M maximum value amounts to 128 $\mathrm{Jkg^{-1}K^{-1}}$ for Gd). On the basis of the mean field approximation, the specific heats should experience a step wise discontinuity at T_c, but, experimentally, ferromagnets usually show a λ-type anomaly in their specific heat at T_c. This fact may be explained by the persistence of a short-range spin order at temperature slight above T_c, but the mean field theory insufficiently reproduces the measurements (Fig.2.7).

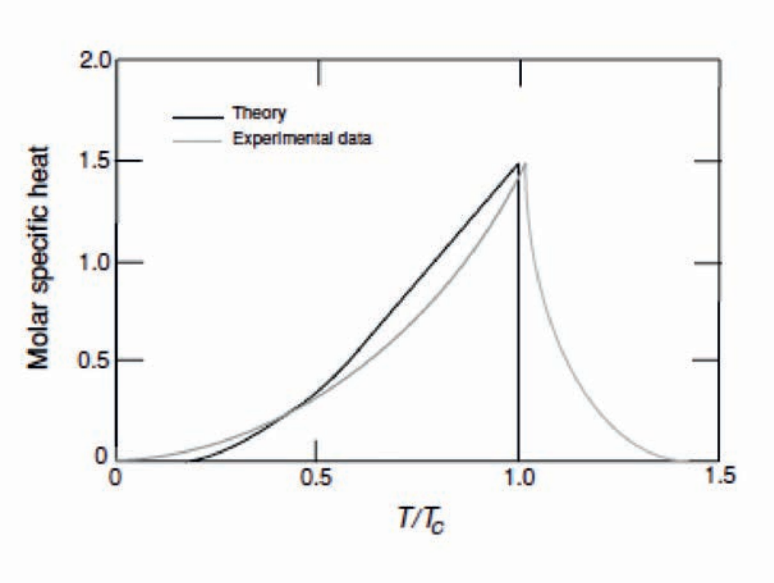

FIGURE 2.7: Comparison of the measured magnetic specific heat of a ferromagnet near T_c (dotted line) with the prediction of mean field theory (solid line) [30].

2.3.4 Irreversible magnetic phase transitions

The condition on the continuity of the magnetization, as a function of T, is not satisfied if the transition is of first order. The situation is sketched in Fig.2.8. By increasing the temperature, the value of M is drastically reduced to zero at the transition tempertaure T_t. This temperature establishes when the minimum of the paramagnetic phase in the Gibbs potential is more stable with respect the ferromagnetic minimum. The correspondent set of HT coordinates are those at which the system transforms. It has to be noted that, following the general description of a first order phase transition, these points on the phase diagrams are accompanied by a coexistence of the two phases and the transitions will have a characteristic latent heat, L, of transformation, which can be calculated with Eqs.(2.26) and (2.27).

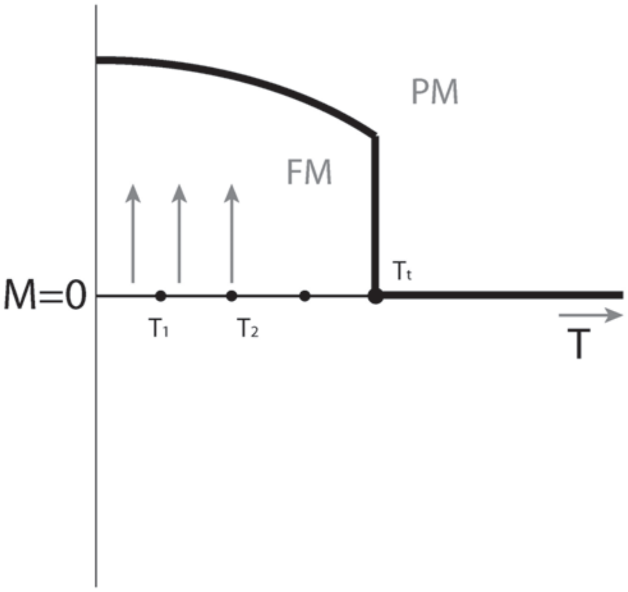

FIGURE 2.8: Schematic MT phase diagram of a first order magnetic phase transition. The magnetization, M, of the ferromagnetic state abruptly drops to zero at T_t.

Actually, in first order transformation, the Maxwell relations can not be applied as they are. The coexisting phases (ferromagnetic - FM, and paramagnetic - PM) may be thought as two equilibrium systems in contact with each other, with the same temperature T_t, thus by equating the Gibbs potentials of the two phases (Gibbs Duhem equation):

$$dG_{FM} = dG_{PM}, \tag{2.46}$$

The equality must hold along the entire coexistance curve (T_t, H_t) and hence:

$$dG_{FM} = -S_{FM}dT - \mu_0 M_{FM}dH = dG_{PM} = -S_{PM}dT - \mu_0 M_{PM}dH, \tag{2.47}$$

thus that:

$$\mu_0 \frac{dH_t}{dT_t} = -\frac{\Delta S}{\Delta M}. \tag{2.48}$$

By using Eq.(2.26) for the the entropy change it results:

$$\mu_0 \frac{dH_t}{dT_t} = \frac{L}{T(M_{FM} - M_{PM})} \tag{2.49}$$

which is known as the Clausius Clapeyron equation. The equation sets up a relationship among: H_t, the magnetic field at which the transition take place, T_t, the transition temperature, ΔM, the magnetization change, and ΔS, the entropy change, at a first order phase transition.

In a magnetic system, in addition to the hysteresis produced by the irreversibility of a first order phase transition, may be important to consider the magnetic hysteresis too. In fact, a ferromagnet is by its nature subjected to magnetic hysteresis due to the domain nucleation and growth processes [31]. The thermo-magnetic hysteresis may thus results from both the processes: the magnetization hysteresis and the irreversible first order phase transition.

2.4 Magnetocaloric effect

Ferromagnetic substances exhibit two unusual thermal effects. These effects are of interest for solid-state physics because they can gives informations on the electronic nature of a solid, and may have some practical applications in refrigeration systems. These effects are large at phase transitions when a material experiences a drastic change in magnetic order. The first effect is the magnetic specific heat which adds on the electronic and lattice specific heats of a solid and it was commented earlier. The second thermal effect is the magnetocaloric effect (MCE). When heat is absorbed by a ferromagnet, part of the heat causes a decrease in the degree of spin order. Conversely, if the spin order is increased, by the application of a large field, heat will be released. If the field is applied suddenly, the process will be essentially adiabatic (quasi-adiabatic) and the temperature of the specimen will rise. The magnetocaloric effect is not to be confused with a much smaller heating effect which occurs during a change of magnetization from zero to the state of technical saturation, i.e., during the conversion of the specimen from the multidomain to the single-domain state. In this case, the magnetization is accompanied by dissipation effects which arise from nucleation and growth of the ferromagnetic domains. The magnetocaloric effect, differently, is caused by the change in spin order accompanying forced magnetization, in which a high field causes an increase in magnetization of the domain itself. This increase in magnetization above the saturation value, for a given applied field, is greatest at the Curie temperature and decreases as the temperature decreases below T_c.

2.4.1 Entropy and the magnetocaloric effect

Since a magnetic material can be roughly represented as consisting of spin, lattice and conduction electrons, these three subsystems has to be considered to contribute to the total entropy of the material.

$$dS = dS_M + dS_l + dS_e. \tag{2.50}$$

With this simple approach, in the case where it is possible to neglect the electronic term dS_e, the entropy of a system is the sum of two contributions arising from magnetic ordering dS_M and from the lattice dS_l of the system. With this observation, it is evident that by controlling the change in magnetization inside a body a temperature variation can be achieved. The simplest way to change magnetization is to apply an external magnetic field, in these cases, if we consider the total entropy S of a magnetic system as a function of temperature, pressure and applied field, H, its total differential can be written as:

$$dS = \left(\frac{\partial S}{\partial T}\right)_{H,p} dT + \left(\frac{\partial S}{\partial H}\right)_{T,p} dH + \left(\frac{\partial S}{\partial p}\right)_{H,T} dp. \tag{2.51}$$

For an adiabatic and isobaric process (where dS = 0, and dp = 0), by using the Maxwell relation of Eq.(2.39) and Eq.(2.42), the expression for the temperature change due to a variation of the magnetic field can be obtained:

$$dT_{ad} = -\mu_0 \frac{T}{c_{H,p}} \left(\frac{\partial M}{\partial T}\right)_{H,P} dH. \tag{2.52}$$

Alternatively, another way to consider the MCE effect, is to write the total entropy of the system as function of the temperature, the pressure and the magnetization of the material. In this way, its total differential can be written as:

$$dS = \left(\frac{\partial S}{\partial T}\right)_{M,p} dT + \left(\frac{\partial S}{\partial M}\right)_{T,p} dM + \left(\frac{\partial S}{\partial p}\right)_{M,T} dp. \tag{2.53}$$

On the other hand, if an adiabatic and isobaric change of magnetization is considered, the expression for the temperature change can be deduced by using the Maxwell relation of Eq.(2.40):

$$dT = -\mu_0 \frac{T}{c_{M,p}} \left(\frac{\partial H}{\partial T}\right)_{M,p} dM. \tag{2.54}$$

Integrating equations Eqs.(2.52) and (2.54) the finite temperature change for an adiabatic process, ΔT_{ad},is obtained:

$$\Delta T_{ad}(T, \Delta H) = -\mu_0 \int_{H_1}^{H_2} \left(\frac{T}{c(T,H)}\right)_H \left(\frac{\partial M(T,H)}{\partial T}\right)_H dH. \tag{2.55}$$

$$\Delta T_{ad}(T, \Delta M) = -\mu_0 \int_{M_1}^{M_2} \left(\frac{T}{c(T,M)}\right)_M \left(\frac{\partial H(T,M)}{\partial T}\right)_M dM. \tag{2.56}$$

Considering a system which is held at constant pressure and at constant temperature the only surviving term is the derivative with respect M of Eq.2.51, which corresponds to the finite entropy change under an isothermal and isobaric magnetization process. Integrating the Maxwell relation of Eq.(2.39) :

$$\Delta S_{iso}(T, \Delta H) = \mu_0 \int_{H_1}^{H_2} \left(\frac{\partial M(T,H)}{\partial T}\right)_H dH. \tag{2.57}$$

A graphical description of this quantities is proposed in Fig.2.9. ΔT_{ad} (horizontal line) and ΔS_{iso} (vertical line) define the MCE. It follows that, in order to measure the magneto caloric properties of a specific system, the magnetic field is applied under adiabatic conditions when any heat exchange with the

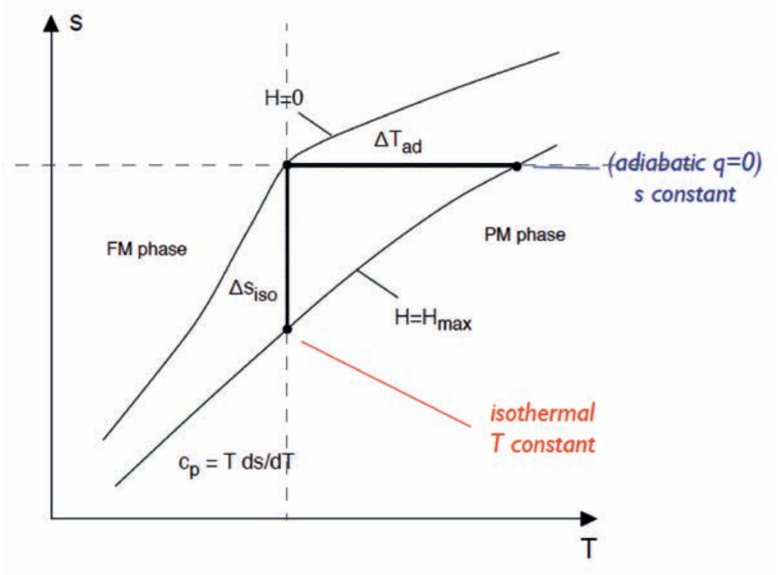

FIGURE 2.9: Graphical description of MCE, considering the entropy of a system as a function of the applied magnetic field and the temperature $S(H,T)$, the MCE is defined by ΔT_{ad} (horizontal line) and ΔS_{iso} (vertical line).

surroundings is absent. In this way the direct measurements the adiabatic temperature change associated to the magnetic field variation can be obtained just by measuring the initial and final sample temperatures.

Unlike direct measurements, indirect experiments allow the calculation of ΔS_{iso}. Considering Eq.(2.53), the finite change of total magnetic entropy under the change of both T and H is the sum of two contributions:

$$\Delta S = \int_{T_1}^{T_2} \frac{c_H}{T} dT + \mu_0 \int_{H_1}^{H_2} \left(\frac{\partial M(T,H)}{\partial T} \right)_H dH = \Delta S_H(\Delta T, H) + \Delta S_{iso}(T, \Delta H). \tag{2.58}$$

From a set of measured isothermal magnetization curves by the integration of the Maxwell relations it is possible to obtain ΔS_{iso}, and this is very useful as a rapid search for potential magnetic refrigerant materials. On the other hand, if is the total entropy change which is obtained by experiments, as in the case of calorimetry data, both the two terms of eq.(2.58) have to be considered, while by isofield measurements of the total entropy change the variation in specific heat of the system can be obtained.

2.4.2 MCE in reversible and first order phase transitions

The above definitions of ΔT_{ad} and ΔS_{iso} are suitable also in those cases where the magnetic order is altered due to a change of magnetic phase of the system. However, the relationships between the magnetocaloric effect and the constant magnetic field heat capacity discussed in the previous section were derived assuming that the total entropy of the magnetic material is a continuous function of temperature. This is the case when phase transitions are of second order or

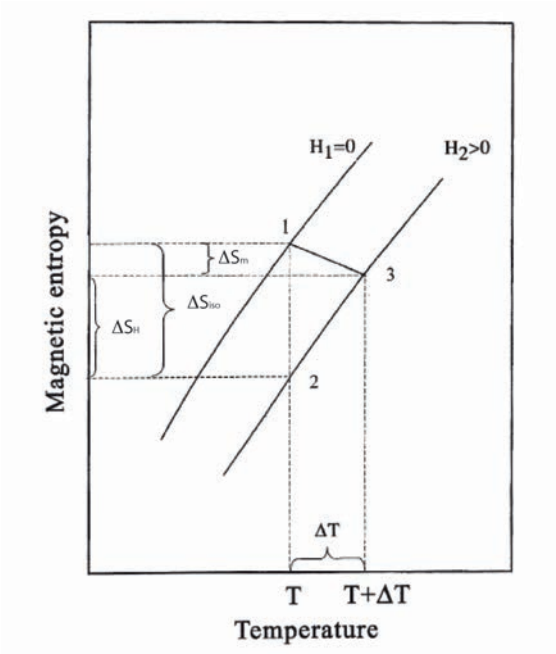

FIGURE 2.10: Temperature dependences of the magnetic entropy S_m at two different fields H_1 and H_2 ($H_2 > H_1$) in a ferromagnetic material [32].

when there is no phase transition at all. In fact, in previous sections, the entropy change was derived at the passage from different magnetic phases and it was calculated on the basis of thermodynamics potential which has to be equal at the phase boundaries. This condition holds also if the two phases are subjected to external magnetic field. It follows that the MCE, at a phase transition, is maximized because the external magnetic field effect sums up to the change in M due to the phase transition.

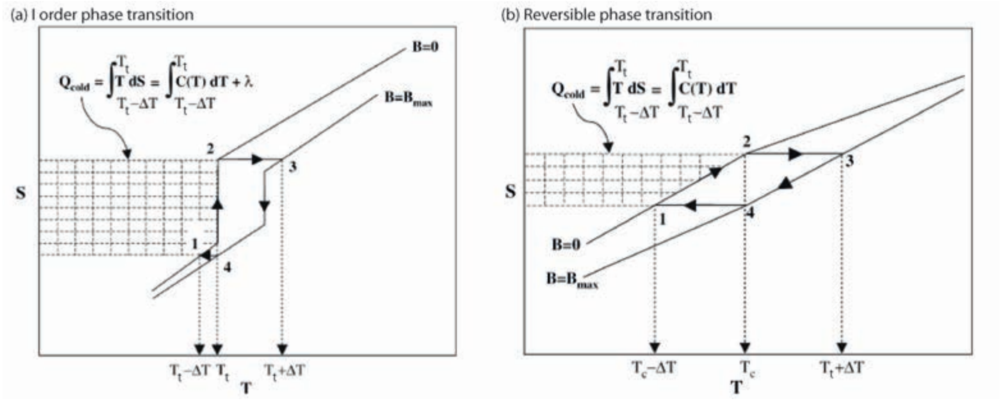

FIGURE 2.11: Comparison of MCE for first order (a) and in second order (reversible) (b) transitions.

In the case of first order transitions the behaviour of the total entropy as a function of temperature must account for discontinuity. Both the specific heat and the magnetization terms of Eq.(2.58) experience discontinuities, thus they must account for irreversible contributions too. The reason is specified in Fig.2.11, for the exchanged heat measured along an isofield curve, where T_t represents the inset of the transition for the heating (or cooling) process.

In this chapter the MCE is presented as a result of the classical thermodynamics. The fundamental equations which will be used in the experimental Ch.5 are explained, in particular the total entropy of a magnetic system, and the magnetic specific heat are treated at the end of the chapter, and the difference between a second and a first order transition are highlighted. The main characteristics of a first order magnetic phase transition which will be encountered in the rest of the thesis are: the coexistence of phases at the transition temperature, the thermal hysteresis and the latent heat content as expression of irreversibility.

PhD Thesis - Chapter 2.

3

MCE in La(Fe,Si)$_{13}$ based compounds

> "When an attempt is made to lower the temperature of liquid helium II below about 1 K by pumping as rapidly as possible trough a tube as wide as possible, the phenomenon of film creep provides a series of events equivalent to a heat leak. The net effect is a transfer of heat to the liquid helium, whose temperature, therefore, cannot be reduced appreciably below 1 K with ordinary apparatus. It was suggested independently by Debye and by Giauque in 1926 that magnetic properties of certain paramagnetic salts could be used to obtain temperature below 1 K. The method suggested was the magnetocaloric effect [33]."

Magnetic cooling could allow the development of an environmental friendly technology based on solid state elements: magnetic materials are used as working bodies instead of gas and magnetization/demagnetization is used instead of compression/expansion in conventional refrigerators. All magnetic materials show MCE to a greater or lower extent, but those which show a higher MCE can reach temperature changes up to 7 K with a 2 Tesla magnetic field [34]. These large magneto caloric effects are possible when, under the effect of an external magnetic field, a material undergoes a phase transition of first order which involves changes both in the intrinsic magnetic order and in the structure. In order to achieve an efficient technology, in addition to the high MCE values, these materials have to fulfil several requirements, so to motivate the intense research among a variety of compositions elements and alloys. A particular example is the class of compounds based on La(Fe,Si)$_{13}$ alloy, whose characteristics and features are commented in this chapter with respect to practical considerations for magneto cooling applications.

3.1 Active Magnetic Refrigerator

The basic idea for magnetic refrigeration consists in a thermodynamic cycle driven by magnetic field changes. One of the technologies developed around this concept, is the active magnetic refrigeration (AMR), in which the magnetocaloric regenerates a fluid which acts as a heat exchange medium. Permanent magnets are used to produce the necessary external magnetic field. The AMR matrix, along with its housing, a motor, a fluid pump, valves, and permanent magnet, replaces the hermetic compressor/motor and valve found in conventional vapor compression systems [35]. One of the advantage of such idea is that in the active magnetic regenerator (AMR) refrigerators, the MCE material works both as the refrigerant and the regenerator, the last is a necessary thermal device which assists in heath transfer between parts of the refrigeration cycle. A sketch of a single component AMR thermodynamic cycle is reproduced in

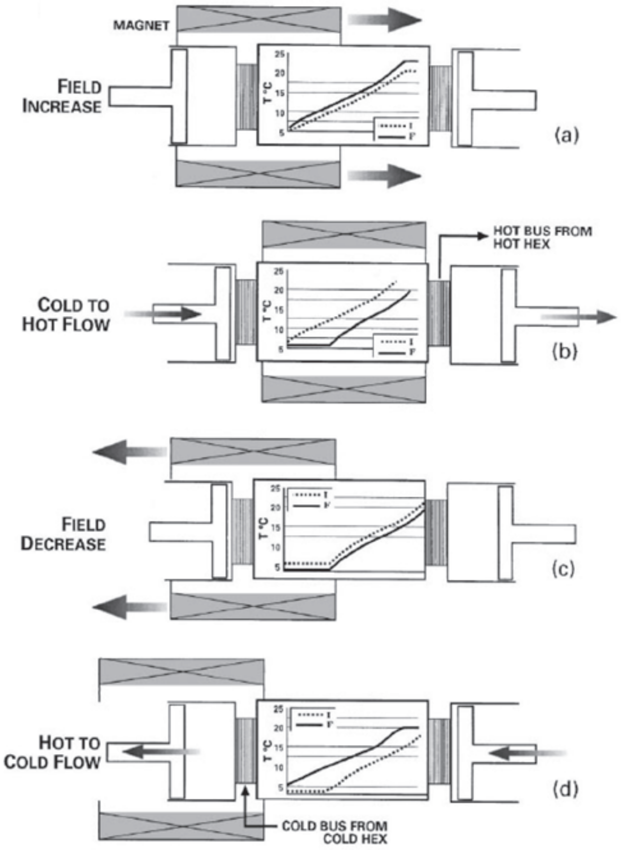

FIGURE 3.1: Active magnetic regenerator cycle: an idealized system in which a porous matrix of magnetocaloric material, the AMR, is cycled into the field created by an ideal ring dipole magnet [36].

Fig.3.1 and consists of four individual steps [36]: (a) increasing the temperature of the active material above the temperature of the hot bath, (b) releasing heat to the hot bath, (c) decreasing the temperature of the active material to a temperature below the cold bath, (d) extracting heat from the cold bath. In the diagram, a MCE material is in contact with a cold sink (left side) and hot sink (right side), bridging the gap between them. The AMR material can be build in the form of perforated-plates AMR, parallel-plate AMR, wires-like AMR or packed-bed AMR (d)). The parallel-plate and packed-bed AMRs are the most widely applied to date, since they allow an easier fluid to flow between the AMR parts. Only a small fraction of the fluid is moved in the thermal baths, thus the AMR is able to develop a temperature gradient, which is sketched in the small graphs of Fig.3.1. Each AMR material should work at the temperature (T_c) at which the MCE is maximum; moving away from such temperature, due to the cycle, the MCE decreases. In the case of refrigeration processes with high temperature differences (large span) the efficiency is lowered due to the decrease of MCE, because of the deviation from the Curie temperature. One solution to this problem is to implement a cascade system, where each cross section has a different material with a Curie temperature in the proximity of its application, so that its working domain and operating temperature range is optimum. In this type of device, the AMR would be made of a layered bed of material, with each layer operating in the vicinity of its Curie temperature, thus providing maximal cooling power, as it is represented in Fig.3.2.

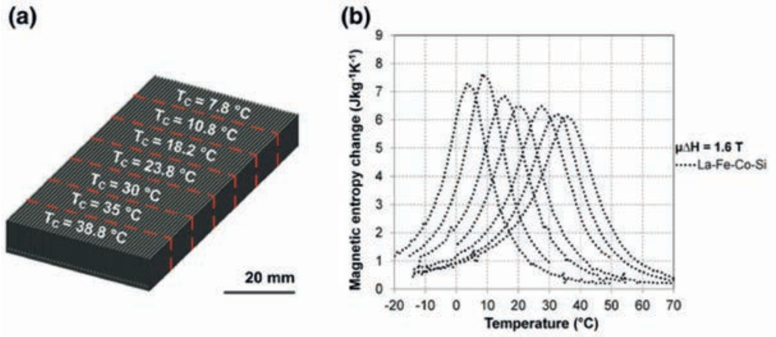

FIGURE 3.2: (a) Example of a AMR with seven layers. (b) The magnetocaloric effect (magnetic entropy change) of La–Fe–Co–Si with different Curie temperatures (reproduced from data obtained from Vacuumschmelze GmbH)[5].

As it was pointed out by Yu et al. [37] and Gschneidner et al.[38], the AMR materials must fulfil a series of properties and characteristics, in addition to the large MCE values, in order to be efficiently used as cooling and regenerator materials:

- Curie temperature close to the working temperature (i.e. room temperature);
- large temperature difference (ΔT_{ad}) in the vicinity of the working temperature;
- no thermal or magnetic hysteresis to enable high operating frequency and,consequently, large cooling power;

- low specific heat and high thermal conductivity, thereby allowing large changes in temperature and facilitating the processes of heat transfer and increasing efficiency;
- high electrical resistance in order to avoid eddy currents in the processes of rapid change in magnetic field;
- no toxicity;
- resistant to corrosion;
- good mechanical properties;
- low manufacturing costs necessary for commercial viability, and
- low environmental impact.

3.1.1 Room temperature candidates materials

The feasibility of magnetic refrigeration at room temperature was introduced by Brow in 1976 through a magnetic refrigerator prototype working with Gd material and a magnetic field created by superconducting magnets up to 7 Tesla [39]. In the element Gd lanthanide metal, the ferromagnetic to paramagnetic

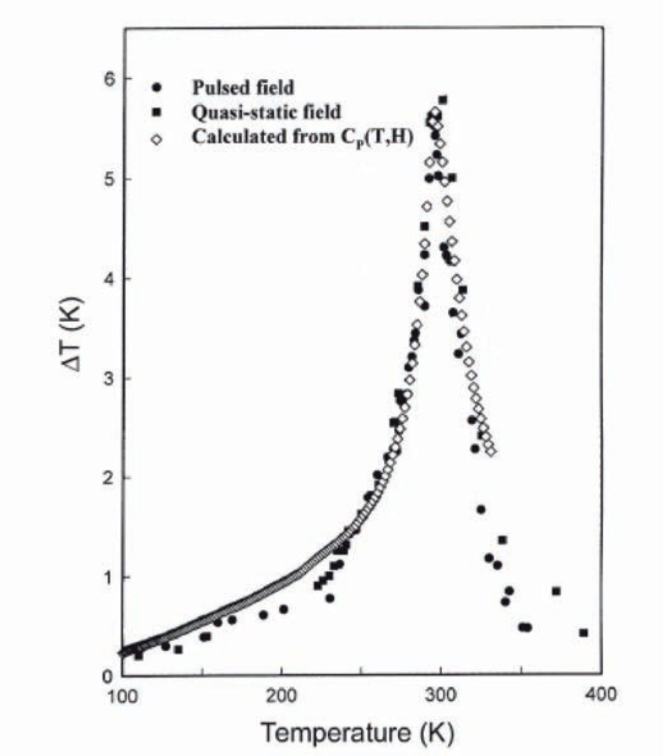

FIGURE 3.3: $\Delta T(T)$ dependences of high purity polycrystalline Gd measured directly by different techniques H = 20 kOe (2 T). (Copyright 1998 by the American Physical Society)[32].

phase transition takes place at 294 K. The use of Gd was studied by many authors and the $\frac{\Delta T_{ad}}{\Delta H}$ to T_c values have been attested to be approximately 2.8 K/T at low magnetic fields and drop to approximately 2 K/T in higher magnetic fields [7]. In 1997, Pecharsky and Gschneidner discovered materials with a remarkable magnetocaloric rensponse at room temperature [12] and stimulated the research of new magnetocaloric materials. $Gd_5(Si_{1-x}Ge_x)_4$ has a magnetostructural transition leading to a giant magnetocaloric effect (GMCE) at room temperature. The interest on the R_5T_4 materials, where R is a rare-earth element and T = Si, Ge or Sn can be ascribed to a number of unusual features observed in these compounds, such as a colossal magnetostriction and giant magnetoresistance. These behaviours are due to a coupled magneto structural first order transition in which slabs of a well defined arrangement of R and T atoms shift $\sim$ 0.5 10^{-10} m with respect to each other along the a-axis when the material transforms under the influence of temperature, magnetic field or pressure. This shift gives rise to an $\sim 1\%$ volume change at the transition. The phenomenon, which gives rise to the GMCE, is thus the transformation of the lattice cell in different structures either applying a magnetic field or cooling the system. The interesting features of these transformations are that T-T bonds between the slabs are absent in the Sm_5Ge_4-type structure, or that they are absent between alternate slabs in the $Gd_5(Si_2Ge_2)$-type structure, but that the T-T atoms are present between all the slabs in the Gd_5Si_4-type structure [40]. Another interesting feature is that the first order transition temperature in the $Gd_5(Si_{1-x}Ge_x)_4$ is strongly dependent on the Si:Ge ratio, especially for x ≥ 0.5 (see Fig.3.4 [41]).

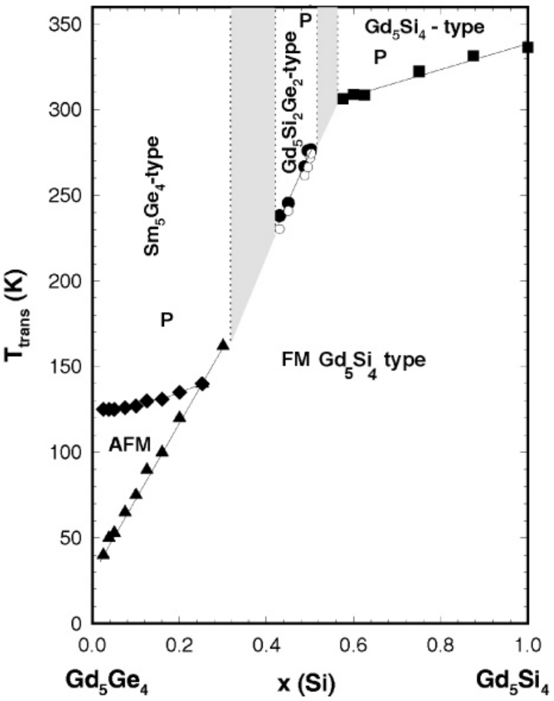

FIGURE 3.4: Low temperature part of the pseudo-binary phase-diagram Gd5Ge4–Gd5Si4 reprint from [12]. In the shaded regions phases co-exist [41] [42].

For materials with magneto structural transition, although the high magnetocaloric response is centred at the transition temperature, the magnitude of the magnetocaloric response in each of the four steps of the cycle depends on the thermal and magnetic history of the material which is generated by the four steps. In fact, the first order nature of these phase transitions principally involve the existence of thermal and magnetic hysteresis, while the magnetostructural coupling and the changes in volume may produce thermal stress between the existing phases. Both the magnetic hysteresis (during an alternating magnetic field) and the thermal hysteresis (during heating and cooling), result in an energy loss and therefore, imply an increase in the input work of the thermodynamic cycle. This can drastically reduce the MCE during the cycling operation as well as the efficiency of the magnetocaloric device. It follows that, dynamical investigation and experiments are required in order to avoid that the intrinsic kinetics of first order phase transitions influences and limits the refrigerator performance. Each of the class of candidates for MCE application may thus deserve a proper attention to correctly characterize its features and drawbacks.

3.2 La(Fe,Si)$_{13}$ based materials

Two graphs summarizing the most suitable compounds for room temperature applications based on the ΔS_m, ΔT_{ad} values and their Curie points are reported in Figs.3.5(a) and (b). As it emerges from the graphs, a class of magnetic materials which are promising due to their enhanced magnetocaloric effect (MCE), is the one based on La(Fe,Si)$_{13}$. Since the first order nature of the transition had become a prerequisite, due to the larger achievable MCE values, those classes of materials characterized by very low values of thermal and magnetic hysteresis, in spite of the irreversibility, are particularly attractive. Such feature is present in La(FeSi)$_{13}$ alloys [43], which belong to the Fe-rich rare-earth-iron compounds such as R$_2$Fe$_{17}$, R(Fe,M)$_{12}$ and R(Fe,M)$_{13}$, where R = rare earth element, M is Si, Al, etc. the main group elements. These compounds possess a large

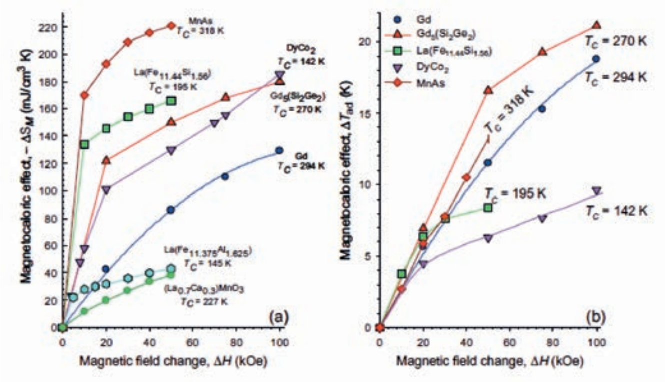

FIGURE 3.5: The isothermal entropy change as a function of the magnetic field change (a) and the adiabatic temperature rise as a function of the magnetic field change (b) for different materials available in literature [38].

MCE because of the large enough spontaneous magnetization and the sharp drop in magnetization with increasing temperature. The former arises from the large amounts of Fe atoms and the latter is associated with ferromagnetic-paramagnetic transitions at the Curie temperature, due to the direct magnetic exchange interaction between Fe atoms [44]. These prerequisites have made La(FeSi)$_{13}$ based compounds strongly investigated among the class of magnetocaloric materials in the last 30 years. However, one of the first experimental investigation was made in 1983 by Palstra et al. [45], who studied the La(Fe,Si)$_{13}$ compounds by measuring the temperature dependences of the zero-field susceptibility and the electrical resistivity. The concluding remarks of this work showed that the compound has strong critical behaviour in the temperature dependence of the magnetization susceptibility and resistivity. The ferromagnetic state had a susceptibility critical exponent corresponding to that found in isotropic, 3-dimensional Heisenberg ferromagnet occurs, while the anomaly in the resistivity was interpreted as a sign of a lattice structural change. In 1999 a paper of Fujita [16] renewed the interest in such compounds, and later, in 2001, Hu and collaborators [23] measured the entropy change at the reversible transition (second order) in LaFe$_{11.4}$Si$_{1.6}$ finding a value of 19.4 J/kgK, much larger than for other materials showing a reversible transition. Since then, a large number of experiments ([44] [17] [18] [46]) have been devoted to the MCE properties of the compounds at the transition and, in particular, a strong attention has been directed to the role of substitution elements and interstitial atoms.

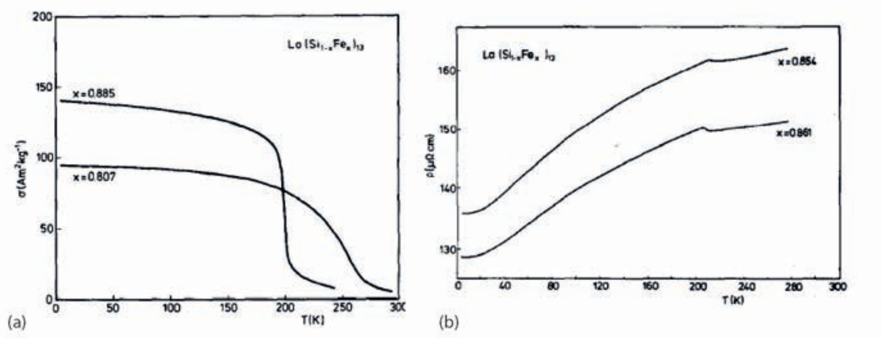

FIGURE 3.6: (a) Temperature dependence of the magnetization in LaFe$_{11.5}$Si$_{1.5}$ (x = 0.885) and LaFe$_{10.5}$Si$_{2.5}$ (x = 0.807) measured in a field of 3 kOe.(b) Temperature dependence of the electrical resistivity ρ in LaFe$_{11.2}$Si$_{1.8}$ (x = 0.861) and LaFe$_{11.1}$Si$_{1.9}$(x = 0.854). [45]

3.2.1 Substitution and interstitial atoms

LaFe$_{13}$ does not exist because of its positive formation enthalpy. To obtain a LaFe$_{13}$-based alloy, a third element has to be introduced. The first stable LaFe$_{13-x}$M$_x$ compound was obtained by Kripyakevich et al.[47] in 1968 after partially replacing Fe with Si or Al. The compound crystallizes in the cubic NaZn13-type structure with a space group of $Fm\bar{3}c$. The incorporation of Si/Al causes no change in crystal structure but lattice shrinkages because of the small atomic size of Si/Al compared with that of Fe. The measured lattice constant of LaFe$_{13-x}$Si$_x$ was found to decrease with Si content increasing from ~1.1475 nm for x=1.2 to ~1.1450 nm for x=2.5. Although the change is not very large, it has dramatic effects on magnetic properties. In this study, performed by Shen et al. [48], the LaFe$_{13-x}$Si$_x$ is paramagnetic near the ambient temperature, and transforms into a ferromagnet upon cooling at a temperature between 200 and 250 K, depending on Si content. The obtained Curie temperature increases linearly from ~175 K for x=1.17 to ~254 K for x=2.5, a rate much more rapid than that expected for a simple dilution effect, indicating the change of electronic structure due to the incorporation of Si.

In the composition range LaFe$_{13-x}$Si$_x$ ($1.0 \leq$ x ≤ 1.6), the stable 1:13 phase undergoes a first order transition accompanied by a large volume change in the vicinity of its Curie temperature T_c [23]. When $1.6 <$ x ≤ 2.0 a second order transition occurs and the corresponding magnetic entropy change becomes smaller. Further increasing the Si content, a tetragonal structure is formed [22]. As in the case of Gd based compounds, the Curie temperature can be tuned in a range of temperature close to the ambient one by opportune substitutions, without loosing the giant values of MCE. As an example, the transition temperature of the first order compounds, which is around 200 K, can be tuned up to room temperature by partial substitution of Fe with Co, which modifies the exchange interaction between ferromagnetic atoms.

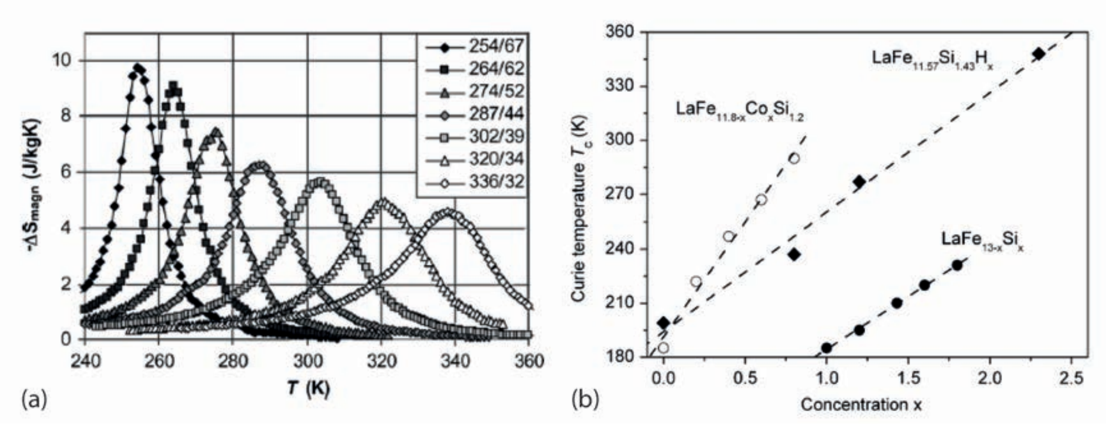

FIGURE 3.7: (a)Magnetic entropy changes of various sintered alloys LaFe$_{0.915-x}$Si$_x$Co$_{0.085}$)$_{13}$ with x = 0.05, 0.058, 0.065, 0.075, 0.087, 0.099 and 0.112 (peaks from the left to the right) [49]. (b) The Curie temperature T_c dependence on element concentration x [50].

Increasing the Co content, however, transforms the transition into a second order type corresponding to a lower MCE (Fig.3.7(a)). An interesting solution is the introduction of interstitial hydrogen, which conserves the first order character and the high MCE. However, the full hydrogenation, which is needed to avoid degradation ageing and to have a long time stability of the material [51], shifts the transition to about 350 K (Fig.3.7(b)), making the transition temperature to high for room temperature applications.

With respect to the Co effect, the substitution of Fe with Mn atoms, which prefer an AFM coupling [52], lowers the transition temperature T_t and permits a fine tuning of T_t [53]. The concomitant effects of the interstitial hydrogen and of the Mn substitution can thus be used to obtain the desired high MCE close to room temperature. The system with Mn is also particularly interesting because a transition on the border between first and second order can be obtained and it may provide the optimal magnetocaloric properties.

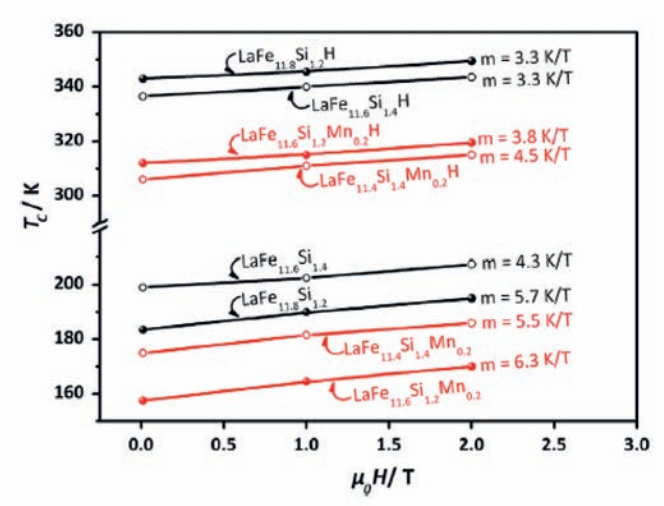

FIGURE 3.8: Field dependence of transition temperature $\mathrm{d}T_c/\mathrm{d}H$ for four representative samples with Mn, Si and H [53].

It has to be noted that, although the promising feature offered by substitution elements, depending on the route of preparation of the samples, additional undesirables features may affect the MCE properties of the compounds. For this reason, a systematic study of the microstructure and the magnetocaloric effect in LaFe$_{11.8}$Si$_{1.2}$ and LaFe$_{11.4}$Si$_{1.4}$ alloys over a large range of annealing temperatures and times was carried out by Liu et al. [22]. As pointed out before, a minor additions of Si or Al are required to stabilize the cubic NaZn13-type phase. For $1.0 \leq x \leq 2.0$, however, it is difficult to prepare single phase La–Fe–Si bulk materials by conventional casting and during the solidification, α-Fe dendrites firstly grow from the liquid and then peritectically react with the surrounding liquid forming a La-rich phase in the interdendritic region. In this case, due to the incompleteness of the peritectic reaction, a large number of α-Fe dendrites are usually preserved at room temperature. Homogenization treatment at high temperatures (up to 1373 K) is thus required to obtain a maximized single phase 1:13-type material together with the high value of ΔS_{iso}. However, for higher values of annealing temperatures, the number of α-Fe phase starts to grow and interestingly reduces the MCE of the compound (Figs.3.9 (a) and (b)). The effect of α-Fe inhomogeneities have thus to be considered carefully during the characterization of the MCE properties of compounds. Another interesting example of the effect of substitution elements can be found in the work of Krautz [53]. For LaFe$_{11.8-x}$Si$_{1.2}$Mn$_x$ samples it has been shown that the amount of α-Fe phase increases with increasing Mn content. Therefore, it was concluded that

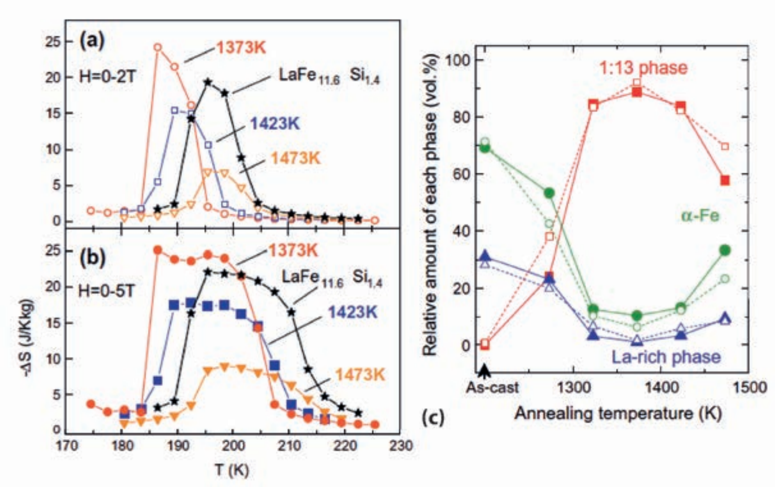

FIGURE 3.9: (a) and (b) Temperature dependence of ΔS for annealed LaFe$_{11.8}$Si$_{1.2}$ bulk alloys under a magnetic field change of (a) 0-2 T and (b) 0-5 T. The black lines are for LaFe$_{11.4}$Si$_{1.4}$ annealed at 1323 K. (c) Volume fraction of constituent phases as a function of annealing temperature (closed symbols determined by SEM, open symbols determined by Rietveld refinement) of LaFe$_{11.8}$Si$_{1.2}$. [22].

the Mn atoms may inhibit the homogenization process to form the 1:13 phase. The results are reported in Fig.(3.10), where the 1:13 phase is reduced especially in the sample with low Si content.

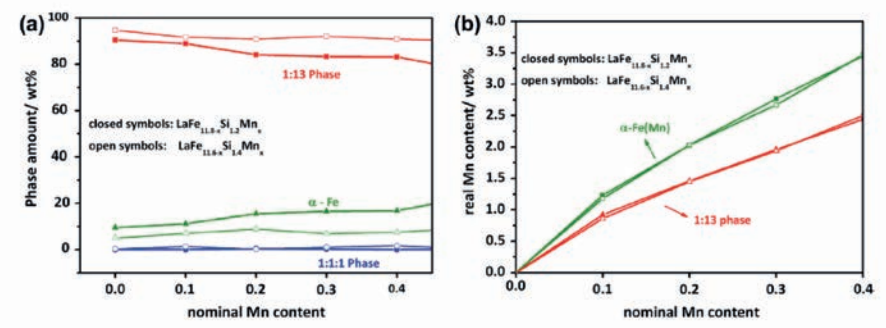

FIGURE 3.10: (a) Phase constitution of non-hydrogenated LaFe$_{11.8-x}$Si$_{1.2}$Mn$_x$ (closed symbols) and LaFe$_{11.6-x}$Si$_{1.4}$Mn$_x$ (open symbols) obtained by Rietveld refinement of XRD patterns and (b) solubility of Mn in 1:13 matrix phase and α-Fe as secondary phase (results obtained by EDS) [53].

3.2.2 Contributions to the hysteresis

Among the reasons of interest offered by La(FeSi)$_{13}$ based compounds, there is also the possibility to change the nature of its phase transition from first to second order, close to room temperature. In many works, devoted to small variation of composition or changes in temperature or magnetic field, experimental evidences do appear of a drastic change of phenomenologies associated with the transition.

An example is furnished in Fig.3.11, where the separated measure of irreversible and reversible heat at the transition was conducted by Morrison et al.[54] by exploiting microcalorimetry methods. With respect to other types of first order phase transition, the one of the $La(FeSi)_{13}$ based compounds was ascribed to a case in which, a coupled heat capacity and latent heat behaviour appears.

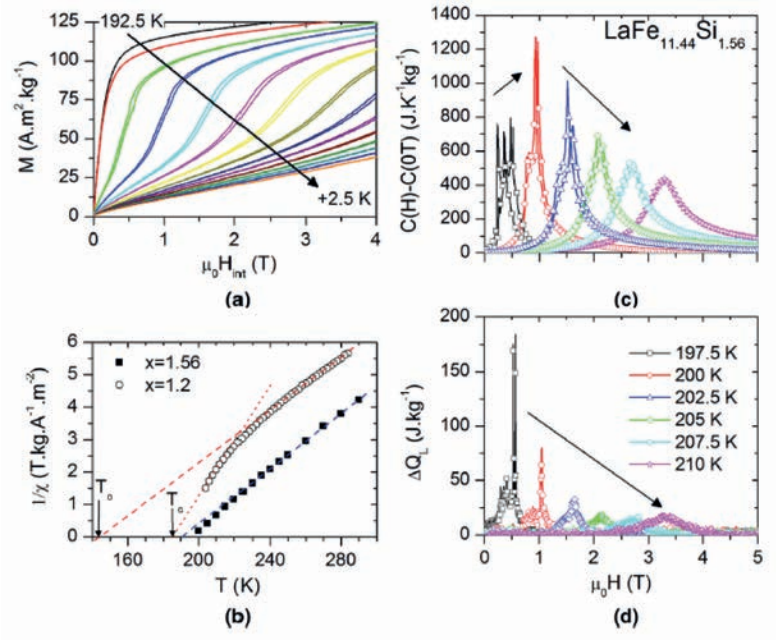

FIGURE 3.11: (a) $M(H)$ loops for $LaFe_{11.44}Si_{1.56}$ at increments of 2.5 K (the S-shaped curve moves to higher fields as the temperature is increased). (b) The corresponding Curie–Weiss plots for $LaFe_{11.44}Si_{1.56}$ and $LaFe_{11.8}Si_{1.2}$. (c) The change in heat capacity and (d) latent heat measurements for $LaFe_{11.44}Si_{1.56}$ [54].

Fig.3.11 highlights three main features as a function of the external magnetic field:

- A continuous change of the magnetic moment (Fig.3.11(a)) and of the transition temperature;
- The variation of the inverse susceptibility from the linear behaviour expected by the Curie–Weiss law (Fig.3.11(b)), indicating two different Curie temperatures: T_0 (in the absence of a volume change) and T_c (the observed Curie temperature);
- A large change in the heat capacity ($\Delta C > 100$ pct) accompanied by latent heat, both of which change dramatically with the increasing transition temperature (Figs.3.11 (c) and (d)).

The benefits arising from this behaviour are mainly ascribed to the ease with which the transitions can be tuned with respect to field, temperature, or composition in order to approach the critical point (i.e., where the phase transition moves from first order to continuous). This feature suggests that material systems which exhibit an easily tunable critical point are desirable, not only because they enable better control of the desired properties (ΔS_{iso},ΔT_{ad} and T_c), but also because of the lower hysteresis ($\mu_0 \Delta H_{hyst}$) associated with them.

Generally, the experimentally observed hysteresis in first order systems correlates with intrinsic and extrinsic factors. Intrinsic ones usually include strain effect, frictions from domain rearrangements, impurity and nucleation factors, band structure, and etc. Extrinsic ones mainly refer to the heat transfer during measurements, the field/temperature rate, the sample surface to volume ratio, etc. Strong magneto-volume effect is a common feature for the first order magnetocaloric materials and strain effect and frictions from domain rearrangements are unavoidable. Moore et al. studied the Gd_5Ge_4 [55] system and found that, when a sample is broken into fragments, the operating field for the transition became lower due to the reduction of internal strain. However, they found that when the sample was further reduced into fine powder (particle size $\sim 100\ \mu m^3$), the magnetic transition and the MCE nearly disappear. They also observed this hysteresis effect in first-order La($Fe_{1-x-y}Co_xSi_y$)$_{13}$ [56] systems, highlighting that the magnetic hysteresis appears strongly field sweep rate dependent. Such effect was interpreted as due to heat transfer conditions, which differ depending on the sample dimension. This fact was also observed in [43] by changing the contact medium between the samples and the sensor of measure in calorimetry experiments. A detailed discussion on the sample size dependent hysteresis, particularly for the particles smaller than 100 μm, is still limited, however, some insights are present in the work of Hu [57]. The size dependent hysteresis losses and the associated MCE were reported for $La_{0.7}Ce_{0.3}Fe_{11.6}Si_{1.4}C_{0.2}$ first order particles smaller than 120 μm. As the sample was ground from bulk into small particles (20 - 50 μm) the hysteresis reduced of about 61 $\%$ with respect the bulk. Such reduction was ascribed to the notably increased surface area of the sample and to the partially removed internal strain and grain boundaries. For particle size above 20 μm, the hysteresis loss get smaller while the effective entropy change remained nearly unchanged, however, as the particles were further ground into extra-fine powder samples (below 10 μm - average 4 μm) they lost stability and the MCE was remarkably reduced.

Similarly, Fig.3.12 (b) reports the comparison for the adiabatic temperature change in samples produced in the form of porous materials by compaction of the pulverized bulk alloy, melt-spun ribbons and nanocrystalline mechanically milled powders [58]. The performance of La(Fe,Si)$_{13}$ based systems with porous architecture is of a magnetic hysteresis partially improved due to partial removal of grain boundaries that restrain volume expansion, however when the porous architecture was prepared with nanoparticles (40 nm) the MCE was drastically reduced. In order to maintain the excellent MC performance, microcrystalline alloys combined with a porous architecture, should be favoured.

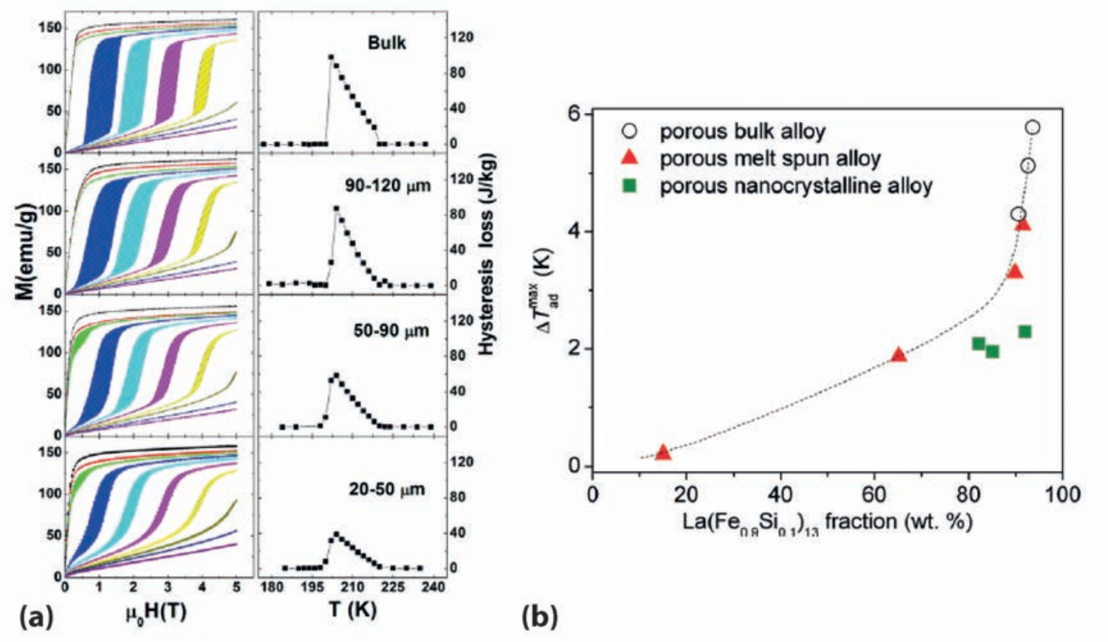

FIGURE 3.12: (a) Magnetization isotherms on field increase and decrease and the deduced hysteresis loss for different particles size compared to the bulk [57]. (b) Maximum adiabatic temperature change in LaFe$_{11.6}$Si$_{1.4}$ with various microstructure in dependence on the La(Fe,Si)$_{13}$ phase fraction. [58].

Further and more recent studies on this topic were also conducted by other groups. Recent results on volume and magnetization response due to the fragmentation of bulk samples were presented in [59] and [20]. In both works, respectively by in-temperature tomographic volume reconstruction and a magnetization relaxation technique, it was shown that, depending on the fragments size and on their arrangements with respect to each others, very different thermo magnetic hysteresis curves can be obtained. The examined magnetic transition of clearly separated particles (Fig.3.13), has been found to be much broader compared to the interlocked particle ensemble. The motive of this behaviour was attributed to the magneto static interactions, which do not require direct contact between the particles and may thus facilitate the nucleation in neighbouring particles, leading to an avalanche-like sharp transition.

Micro structure, particle arrangement, dimensions, compositions elements and secondary phases are all shown to contribute to the MCE properties of the La(Fe,Si)$_{13}$ based compounds. Depending on these factors, the first order nature of the transition can be suppressed, leading to a reduction of the magnetic entropy change. On the other hand, without considering all these factors, the thermo-magnetic hysteresis width may be overestimated, leading to a wrong conclusion about the cycling frequency and magneto cooling power of the alloys.

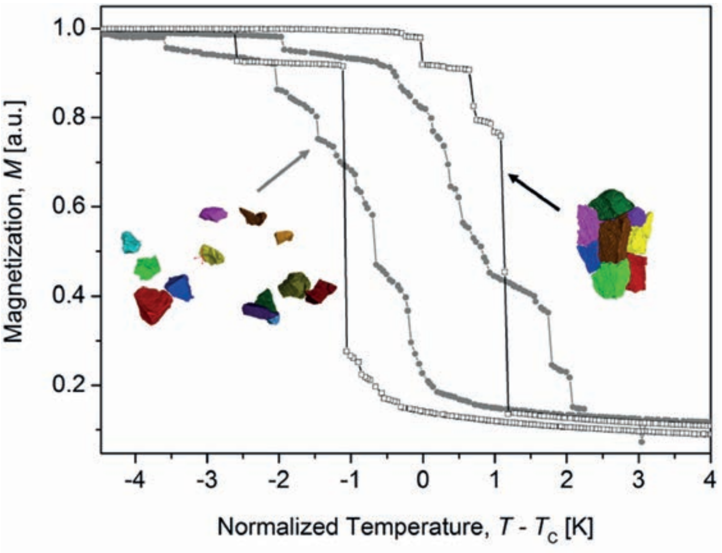

FIGURE 3.13: The magnetic transition of an interlocked particle ensemble (open squares) with volume 0.12 mm^3 is very sharp even though most particles are separated by cracks of widths in the range 2-6 μm. For a well separated particle ensemble of volume 0.18 mm^3 (solid circles), the transition broadens significantly. The sample images show the measured particle ensembles imaged with computed tomography [59].

3.3 Origin of the giant magnetocaloric effect

For LaFe$_{13-x}$Si$_x$ compounds with Si content x < 1.6, an external field can induce a transition from a paramagnetic to a ferromagnetic state at temperatures near but above T_c, which is the so-called itinerant-electron metamagnetic (IEM) transition [16]. The FM state becomes more stable than the PM state under an applied field due to the field-induced change in the band structure of 3d electrons. The IEM transition is usually indicated by the appearance of "S"-shaped M^2-H/M isotherms (Arrott plot). For the LaFe$_{13}$-based compounds, the lower the Si content is, the stronger the first-order nature of the magnetic transition will be. The origin of the large ΔS_{iso} in the compound LaFe$_{11.4}$Si$_{1.6}$ was attributed by many papers to the rapid change of magnetization at the T_c caused by a dramatic lattice expansion of about 1% when transforming into the FM phase. The temperature dependence of the lattice parameter was obtained firstly by Hu et al. from XRD patterns (see Fig.3.14) and confirmed that the crystal structure remain cubic NaZn13-type upon altering the magnetic state from paramagnetism to ferromagnetism.

3.3.1 Itinerant electron metamagnetic transition

In 1999 a paper of Fujita [16], showed a first-order transition above the Curie temperature for ferromagnetic La(Fe$_x$Si$_{1-x}$)13 (x=0.86 and 0.88) compounds by

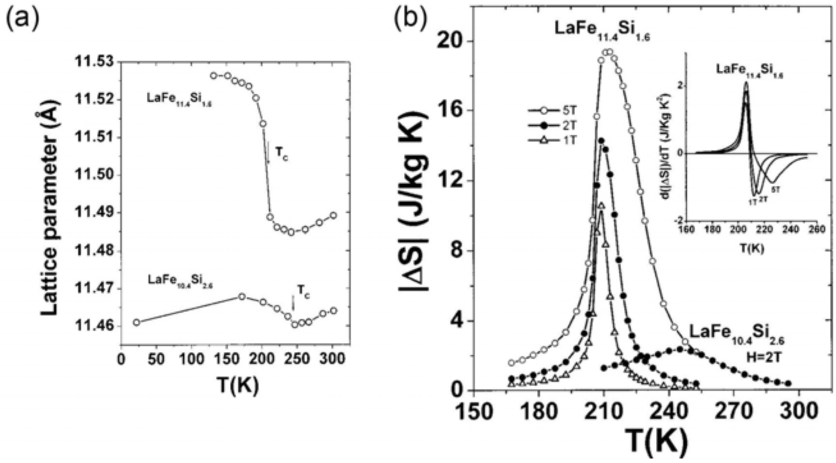

FIGURE 3.14: (a)Temperature dependent lattice parameter of LaFe$_{11.4}$Si$_{1.6}$ in comparison with that of LaFe$_{10.4}$Si$_{2.6}$. (b) Magnetic entropy change of LaFe$_{11.4}$Si$_{1.6}$ for the magnetic field changes of 0 to 1.0 to 2, and 0 to 5 T respectively. For comparison, the ΔS_m of LaFe$_{10.4}$Si$_{2.6}$ under 2 T is also presented. The inset shows the differential curves of ΔS_m for LaFe$_{11.4}$Si$_{1.6}$ [23].

applying a magnetic field. The Curie temperatures of the two alloys, were determined by the Arrott plots (207 K for x=0.86 and 195 K for x=0.88 Fig.3.15 (a)) and the measurements performed above the Curie points of both compounds were characterized by the hysteresis in the magnetization curve (b) and (c). The results were interpreted as the inset of an itinerant electron metamagnetic transition (IEM) above the Curie temperature. Moreover, this IEM transition was attributed to the 3d electrons of Fe, also because an enhanced effect was observed in the compound with an higher amount of Fe (Fig.3.15 (c)). The theoretical discussion on the itinerant electron metamagnetic transition is closely concerned with the double minima of the paramagnetic (M=0) state and the ferromagnetic (M>0) state in the magnetic-free energy as a function of magnetization F(M). When the minimum in the ferromagnetic state is lower than that in the paramagnetic state at 0 K, the system is ferromagnetic in the ground state. However, at high temperature, the ferromagnetic energy minimum can become shallower than the paramagnetic one, resulting in the paramagnetic state of the compound. By applying the magnetic field, the ferromagnetic energy minimum again becomes lower than the paramagnetic one and the first-order metamagnetic transition from the paramagnetic to the ferromagnetic state can be induced. Following the work of Fujita [16] and considering the case of the compound with x=0.88, the free energy as a function of the uniform magnetization M has two minima at M=0 and M > 0, which respectively correspond to the paramagnetic and the ferromagnetic states. Under these conditions, the free energy structure gives not only the thermal induced first-order phase transition between the ferromagnetic and the paramagnetic states, but also the magnetic-field induced metamagnetic transition from the PM states to the FM state above the Curie temperature. The hysteresis in the magnetization curves above T_c

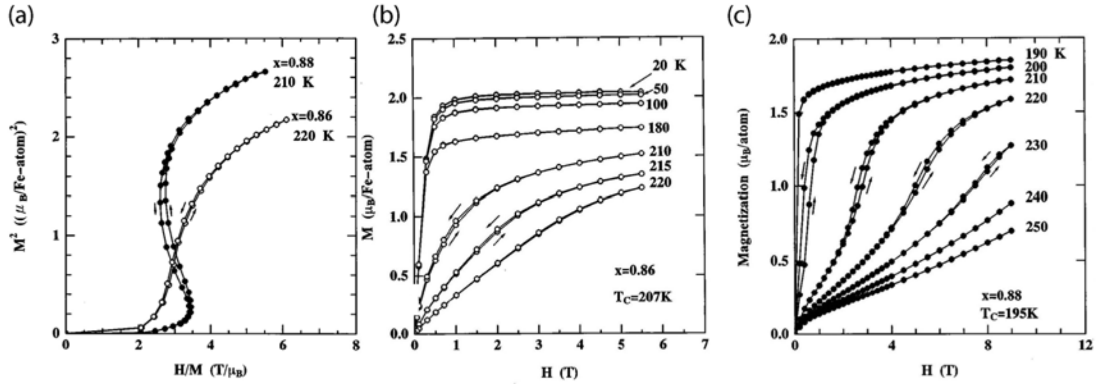

FIGURE 3.15: (a)The Arrott plots at 220 K for x=0.86 and at 210 K for x=0.88. Magnetization curves of the La(Fe$_x$Si$_{1-x}$)13 compound at various temperatures: (b) x = 0.86, lower amount of Fe atoms and (c) x = 0.88, higher amount of Fe atoms. Hysteresis is present above the Curie point. The magnetization M is smoothly saturated and its magnitude gradually decreases with increasing temperature below T_c.

were brought as one of the evidence for the onset of the IEM transition also because the strong similarity with the curves found in Lu(Co$_x$Ga$_{1-x}$)$_2$ compounds due to Co substitutions, which is a compound with a ferromagnetic ground state that exhibits an itinerant electron metamagnetic transition above T_c [60].

In the works of Fujita, Fujieda and Fukamichi, the IEM transition at finite temperatures was discussed in terms of both the Ginzburg–Landau-type free energy expansion and the re-normalization effect of spin fluctuations on the expansion coefficient. The double minimum structure of free energy E(T,M) was phenomenologically described by the Ginzburg-Landau-type expansion in terms of the series of the magnetization as it follows:

$$E(T, M) = F_2(T)M(T)^2 + F_4(T)M(T)^4 + F_6(T)M(T)^6. \tag{3.1}$$

with $F_2(0)>0$, $F_4(0)<0$, and $F_6(0)>0$. For the onset of the IEM transition, the fourth-order coefficient of the Landau expansion should be negative, giving a negative slope of the Arrott plot. This negative slope was measured for the x=0.88 composition together with an inflection point for the x=0.86 composition, also explainable by the negative fourth-order Landau expansion coefficient (3.15(a)). A further element used to prove the IEM transition, was the fact that this type of transitions may be influenced not only by the electronic structure but also by the elastic energy change, because such a large increase in the magnetic moment should be accompanied by a large volume expansion. The La(Fe,Si)$_{13}$ based compounds undergo the first-order magnetic phase transition without any change in the crystal structure. In successive studies, performed by the same group [24] [61], the magnetovolume effects in the ferromagnetic state was connected with the IEM transition. The hydrostatic pressure was used to prove the enhancement of the thermal change in the curve of free energy, and

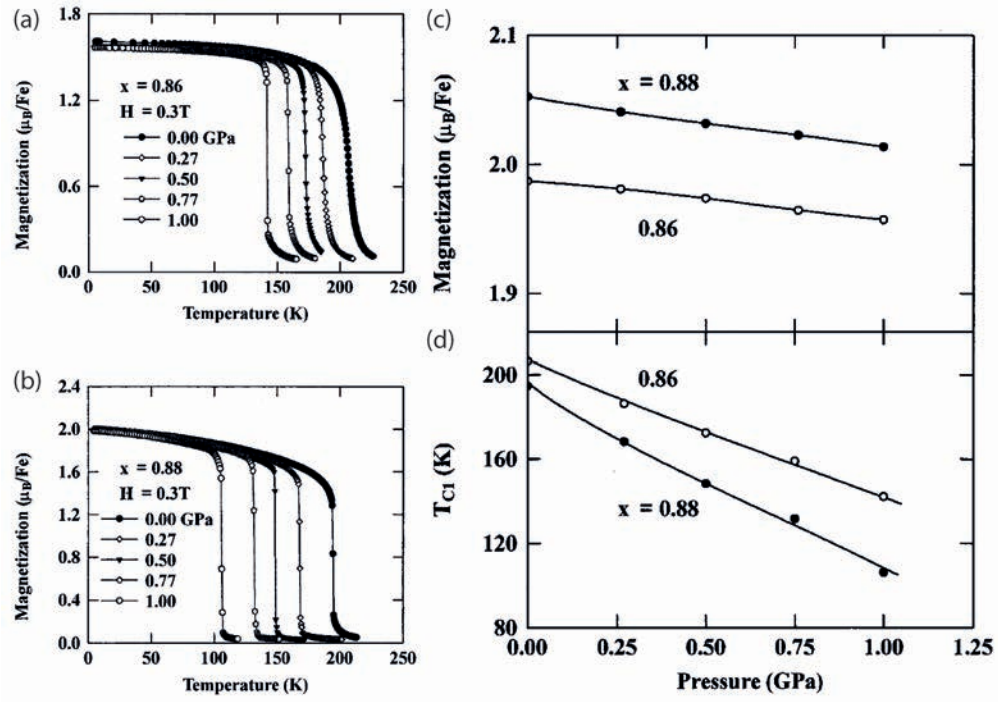

FIGURE 3.16: Temperature dependence of the magnetization measured in applied hydrostatic pressures for (a) x=0.86 and (b) x=0.88. Pressure dependence of the (c) magnetization and the (d) Curie temperature for x=0.86 and x=0.88 [24].

a significant decrease in the Curie temperature was observed by applying hydrostatic pressure, the results are shown in Fig.3.16.

Due to these theoretical and experimental works, the theory of IEM had become popular to explain the field induced transition in La(Fe,Si)$_{13}$ based compounds.

3.3.2 Lattice contribution

The evidence of a volume contraction when transforming in to the high temperature paramagnetic phase of such compounds, favoured the interest in modelling the magneto-volume interaction taking place at the transition. The existence of both ferromagnetism due to the exchange interaction between Fe atoms of the lattice and of the increasing distance of such magnetic atoms at low temperature is in accordance with a theory developed by Bean and Rodbell in 1962 [15]. In their original work on MnAs they construct a theoretical model based on the fact that, the exchange interaction depends on the distance between ferromagnetic atoms and that, an overall variation in the interatomic distance correspond to a volume change of the compound. The double effect, on the volume and on the exchange interaction strength, was described by introducing a Curie temperature dependent on the lattice reduced volume $\Omega = (v - v_0)/v_0$, where v and v_0 are the deformed and equilibrium specific lattice volume, respectively. The Curie temperature results in $T_c = T_0(1 + \beta\Omega)$, with β being a dimensionless coefficient describing the magneto-elastic coupling and T_0 the Curie temperature at β = 0. This theory was applied more recently by Jia et al. [62] on La(Fe,Si)$_{13}$ based compounds. The authors, in accordance with the Bean and Rodbell theory, argued that a lattice shrink should always correspond to a decrease of the lattice entropy, thus that the lattice contribution affects the entropy change at the transition temperature. The theoretical work of Bean and Rodbell has also been used in a work of Piazzi [63] to describe La(Fe,Mn,Si)$_{13}$ compounds with different amounts of constituent elements. The series of compounds offered the possibility to change both the values of the magnetization and of the Curie temperature as a function of the Mn substitution elements, thus to compare experimental data with the model either in first or second order phase transitions [53]. In the model proposed by Piazzi, the expression for the free energy of the magnetic system is composed by the sum of two terms, one which considers the non-magnetic degrees of freedom f_s and one due to the magnetic contributions f_M. The last is described by the molecular field coefficient $W(\Omega)$, dependent on the reduced volume Ω introduced by Bean and Rodbell. The structural part, f_S, of the free energy is mainly due to atomic vibrations (phonons) and give also an entropic contribution which can be isolated in the calculus for the total entropy, s. In fact, the derivative with respect the free energy results in three terms $s_M(m) + s_S(p,T) + s_W(m)$, being respectively the magnetic, the structural and the magneto-elastic entropy. The parameters governig this model are mainly two: η and ζ, whose expression are given below and depend on the Boltzmann constant k_B, the number of magnetic moments per unit mass n, the isothermal compressibility k_T and the thermal expansion coefficient α_p of the solid.

$$\zeta = \alpha_p \beta T_0, \tag{3.2}$$

$$\eta = \frac{3}{2}\frac{\beta^2 k_T n k_B}{a_J v_0} T_0, \tag{3.3}$$

The α_J parameter is a coefficient dependent on the total angular momentum quantum number J, and is given by $\alpha_J = (J+1)/3J$.

The transition from a low temperature ferromagnetic phase to the high temperature paramagnetic phase, which is observed in the La(Fe,Si)$_{13}$based compounds, is obtained for values of ζ < 1. In these cases, the entropy change Δs_M is positive, while the magneto-elastic contribution, Δs_W can either be positive (for $\zeta < 0$) enhancing the overall entropy change, or negative (for 0 < ζ < 1), counteracting the magnetic entropy change.

Numerical calculation showed that the value of η mainly affects the shape of the curve -Δs, while the value of ζ changes the ratio between the height and width of the -Δs peak. With the fixed value of nk_B = 170 Jkg^{-1}K^{-1} and $\zeta = 0.25$, different compositions were compared. The resultant experimental graphs as a function of Mn content and the correspondent theoretical plots as a function of η values are shown in Figs.3.17 (a) and (b). A good qualitative agreement between experimental and modelled entropy change -$\Delta S(H,T)$ appears. The magneto-elastic coupling is shown to be responsible for a decrease of -$\Delta s(H,T)$

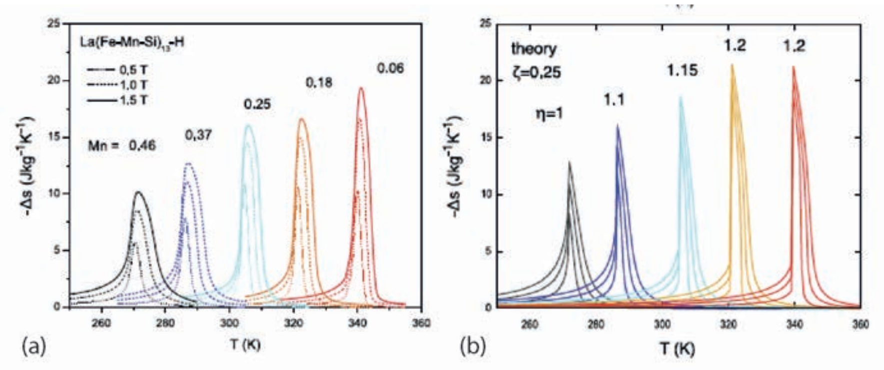

FIGURE 3.17: Magnetic field induced entropy change in hydrogenated La(Fe–Mn–Si)13 samples with different Mn content. (a) experimental curves obtained by Peltier calorimetry [27].(b) Model results derived for J= 1/2 and the same ΔH values set in the experiments [63].

at the transition, due to a small lattice contribution to the entropy, which counteracts the magnetic entropy. At the FM–PM transition, the magnetic and lattice entropies behave differently: the first one is increasing, while the second one is decreasing, with the balance in favour to the former. Interestingly, other experiments on the phonon spectrum of LaFe$_{13-x}$Si$_x$ compounds below and above the transition temperature have reached a different conclusion [25]. In these experiments, the lattice entropy that appears to be slightly larger in the PM state, is shown to act cooperatively with the magnetic contribution. These different facts pose several interesting questions on the nature of the transition and of the FM state of La(Fe,Mn,Si)$_{13}$.

A more interesting result obtained by Piazzi, is that the magneto-elastic coupling drives the phase transition of the system, changing it from second to first order by varying the mean field theory exchange interaction coefficient, a representative graph is reported in Fig.3.18. In this case, the model was at least able to provide the information about the extension of the metastability region of the system under investigation. The latter corresponding to the region in which the equation for the free energy has two coexisting FM and PM solutions.

The La(Fe,Si)$_{13}$ based compounds have a transition from a low temperature paramagnetic phase to a high temperature paramagnetic phase. Many of the experimental works directed to the phase transition of La(Fe,Si)$_{13}$ and its substituted compounds regard the calorimetric properties as a function of the external magnetic field or the tentative to reduce hysteresis through the change in composition elements or shape and route of preparation. These researches leaded to a wide characterization of the magneto structural properties of several compositions; the main achieved results can be summarized as follows:

- the phase transition couples both a change in magnetic order and a structural expansion of the cubic cell [23].

- the transitions can be of the first or the second order and can be induced by a magnetic field [16].

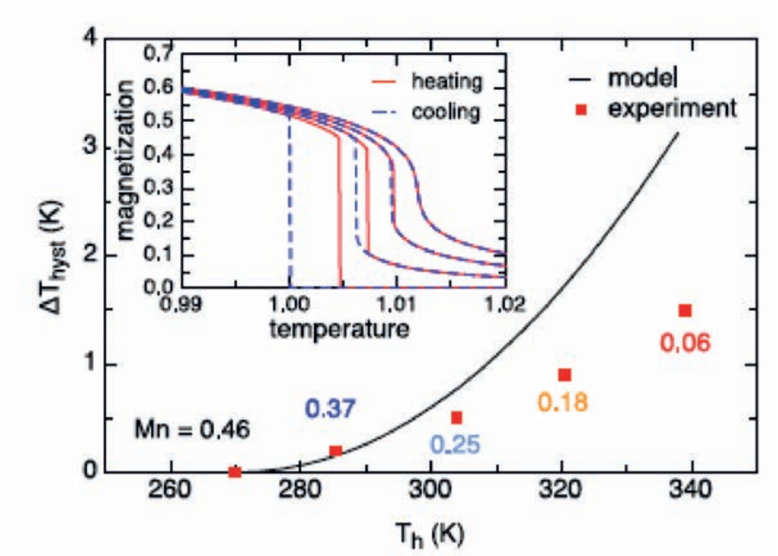

FIGURE 3.18: Experimental(red squares)and theoretical(black line)temperature hysteresis values ΔT_{hyst} as a function of heating transition temperature T_h. Experimental data taken from [27] for La(Fe,Mn,Si)$_{13}$–H$_{1.65}$ with different Mn content. Theoretical curve obtained for $1 \le \eta \le 1.25$. Inset: magnetization versus temperature behavior η =1.2 and at different magnetic fields h for heating (red solid lines) and cooling (blue dashed lines) processes. Remaining parameters are ζ=0.25,J=S=1/2 [63].

- the temperature of the magneto structural phase transition can be tuned by changing composition and with interstitial atoms (around ambient temperature).

With respect to the role of the magnetic field a little is still known about the way on which it interacts with the structure, modifying the energy landscape of the transition, thus that La(FeSi)$_{13}$ based compounds still deserve scientific attention; on the one hand, due to the interesting issue of the IEM nature of the phase transition and, on the other hand, due to the possibility to investigate the magneto-structural coupling in systems which preserve structural symmetry. Ch.5 will be mainly directed to this topic, concerning a series of alloys based on hydrogenation and Mn substitutions.

4

Magneto optical study of La(Fe,Si)$_{13}$ based compounds

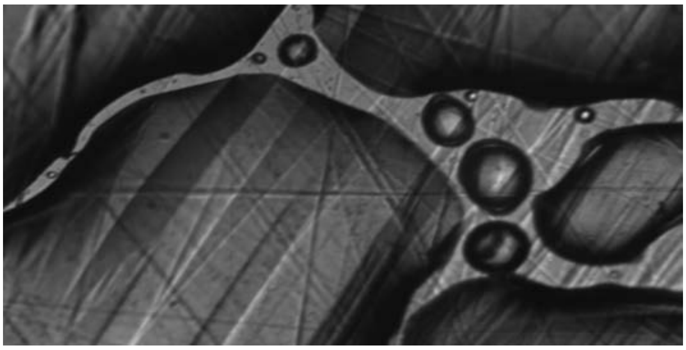

Optical image of the formation of structural variants in the magneto structural phase transition of a sample of Ni_2FeGa. The optical contrast produced by the structure is distorted by the presence of water drops on the surface of the sample.

This chapter presents a study on the magnetocaloric compound La(Fe$_{0.9}$Co$_{0.015}$Si$_{0.085}$)$_{13}$. The spatial evolution of the ferromagnetic to paramagnetic phase transition has been observed, by means of a Magneto Optical imaging technique with Indicator Film (MOIF). Since the phase transitions in La(FeSi)$_{13}$ are magneto-structural, the structural phase separation produces a spatial separation of magnetic behaviours, making magnetic imaging a powerful tool for this type of study. The MOIF technique is explained in the first section of this chapter after a short classification of some of the most known magnetic imaging techniques. Among the suitable methods for the imaging of magnetic materials, the motivation for the use of the MOIF are explained. Details of the experimental setup in use at the Politecnico of Torino are reviewed in section 4.1.1, with a particular attention to the use of Garnet imaging films with a strong Faraday rotation effect. The last sections of the chapter are dedicated to the experimental results, which will be shown to be mainly of two types: a qualitative observation of the phase fronts propagation and a quantitative evaluation of the magnetic phases concurring on the transformation process.

4.1 Magnetic imaging techniques

Magnetic imaging methods serve to visualize and measure the change in magnetic order and in spin structure inside a volume or at a surface. All these techniques were developed after 1931, when Francis Bitter [64] published the first pictures of magnetic micropatterns obtained with the help of an improved powder method. The evolution of the Bitter technique greatly improved the study of magnetization in matter and, nowadays, strongly applies to the study of magnetic domain structure [65] and of the domain walls motion. The type of magnetic orders in solids, the shape of the samples under investigation and the external conditions (magnetic fields, temperature, electrical currents,...) produce very different magnetic signals at different length scales. For this reason, the choice of the imaging technique depends on the type of magnetic phenomena under investigation and on the type of analysis to be performed. It must be highlighted that, depending on the type of interaction between the probe and the sample, the currently used imaging methods can be divided into two main groups.

STRAY FIELD IMAGING TECHNIQUE

- **Bitter decoration**. In the classical method, the surface of a magnetic material is covered by a thin layer of nano particles (size 5–20 nm) suspended in a liquid media (water, kerosene, oil). The optical contrast arises from the nanoparticle concentration at the places of largest field gradients. Optical anisotropy may be induced in the magnetic liquid (ferrofluid) by the local field under study; the former produces additional optical contrast owing to the birefringence observed in polarized light allowing, in principle, a directional map of the stray field pattern to be constructed. Because of this, Bitter layers may be considered as liquid MO films whose resolution is approximately the one of the optical microscope. If some agents are added to the nanoparticle suspension, so that it forms a continuous film on drying, such resolution can be improved by using the thin solid films obtained from the ferrofluid [66].

- **Magnetic Force Microscopy, MFM**. This technique is based on the Atomic Force Microscopy (AFM) method. It implies the use of a silicon micro cantilever: a single ferromagnetic particle can either be mounted on such cantilever or the cantilever itself can be coated with a ferromagnetic film and rasterized across the surface of the sample. The force derivative registered by the deflection of the cantilever or the change of its mechanical resonance frequency gives an image of the stray field gradient at the surface. The resolution achievable with MFM is about 20 nm. A problem arises when imaging soft magnetic materials, because the stray field produced by the tip may perturb the domain structure of the sample.

- **Magnetic field scanners based on sensors** (SQUID, magnetoresistive sensors, Hall probes,...). As an example, the Scanning Hall Probe Microscopy (SHPM) is based on the use of microprobes having a direct response to the projection of the magnetic flux density vector on the axis of sensitivity. Sensors sensitive to the magnetic field component perpendicular to the plane of observation are usually employed, but three-axials sensors are also available.

- **Indirect magneto optic imaging**. This technique is based on a polarization microscope and on the use of high quality transparent films, magnetically active, positioned on the top of a magnetized object. The stray field distribution at the surface of the object induces a polar magnetization component in the active layer (film) which acts as a detector. The interaction between the magnetization and the polarized light in the indicator film is due to the Faraday effect. Such technique, named Magneto Optical imaging with Indicator Film (MOIF), will be discussed in details in section 4.1.1 [66] [26].

MAGNETIZATION DISTRIBUTION IMAGING TECHNIQUES

- **Scanning Electron Microscope**. An important group of domain-observation techniques is based on TEM (Transmission Electron Microscopy). The electrons experience the Lorentz force $e\vec{v} \times \vec{B}$ as they pass through a magnetized sample and they suffer a net deflection from domains magnetized with an in plane magnetization component. Two methods for obtaining magnetic contrast in Lorentz microscopy are the Fresnel scheme and the Foucault scheme. The former images the domain walls in a defocussed geometry as bright or dark lines. The latter images the domains themselves, with contrast that depends on the orientation of the aperture slit relative to the magnetization.
- **Direct magneto optic imaging**. These techniques are based on the interaction between light and magnetization discovered by Maxwell. They make use of the Kerr, the Faraday or the Voight effect and they all exploit the deviation of the light polarization plane performed by the off-diagonal components of the dielectric tensor, ε, depending on the magnetization direction. As an example, the Kerr microscopy is based on the rotation of the light polarization plane upon reflection from a magnetic surface, while the Faraday effect uses an analogous principle upon the transmission of light. With these techniques the magnetization can be observed directly without ambiguity.

This rough classification is useful in order to understand the technique applied in this chapter, since it deals with the use of imaging indicator films to map the stray fields above magnetized objects (superconductors, hard magnetic materials or active integrated circuits).

4.1.1 Magneto Optical imaging with Indicator Film

The MOIF technique provides for the use of an active layer, namely the Indicator Film, which is positioned on the top surface of a magnetized object whose

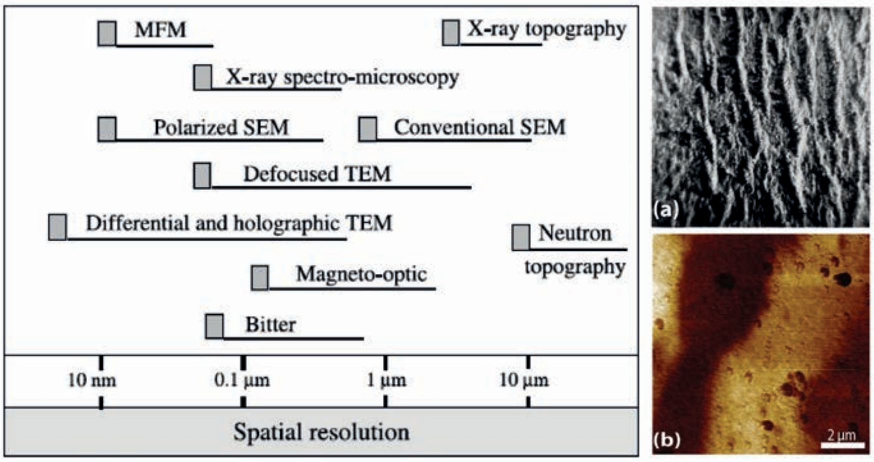

FIGURE 4.2: Left side: comparison of the spatial resolution obtained by different domain observation techniques [65]. Right side: examples of images obtained by stray field methods. (a) The first image showed by Bitter in 1931 of a pattern obtained on an iron-silicon alloy in large fields *[...a suspension is allowed to settle on a magnetized surface, the pattern of the deposit reveals those points at which irregularities in the magnetic flux occur...]* [64]. (b) Stray field pattern of a Mn_2RhSn alloy obtained by MFM measurements at T = 255 K (Ch.6). The bubble domains characterize an out of plane magnetic anisotropy (INRiM).

stray field induces a polar magnetization component in the active layer itself. In order to observe the stray field pattern, the MOIF uses the optical Faraday effect arising from the interaction of the light with the magnetization inside the indicator film.

The Faraday effect

The Faraday Effect was discovered by Michael Faraday in 1846 [67]. It describes the interaction between the polarization plane of an electromagnetic wave and the local magnetization of a transparent material. As mentioned before, the Faraday effect, as far the other MO effects (Kerr, Voight,...), results from the off-diagonal components of the dielectric tensor ϵ of materials. Such off-diagonal components depend on the magnetization of the material which produces an anisotropic permittivity. The speed of light in a material, v_p, is affected by the tensor ϵ according to the expression $v_p = \frac{1}{\sqrt{\epsilon\mu}}$, where μ is the magnetic permeability; such dependency causes fluctuations in the phase of the polarized incident light. In the case of the Faraday effect, the result for an incident linearly polarized light is that the refracted polarization plane is rotated by an angle α_F, which is given by the following equation:

$$\alpha_F = \nu \cdot d \cdot M_{\parallel}. \tag{4.1}$$

Where d is the length of the light path into the magneto optical (MO) media. A positive Verdet constant, ν, corresponds to a left-rotation (anticlockwise) when the direction of propagation is parallel to the magnetization vector and to a right-rotation (clockwise) when the propagation direction of light is antiparallel to the magnetization vector. Thus, if a ray of light passes through a material and is reflected back through it, the rotation doubles (this principle s used in MOIF experiments). It has to be noted that an external magnetic field has no direct influence on the electromagnetic wave since the Faraday effect is due to the interaction between light and the induced magnetization of the solid medium parallel to propagation direction of the incident light $M_{\parallel}$.

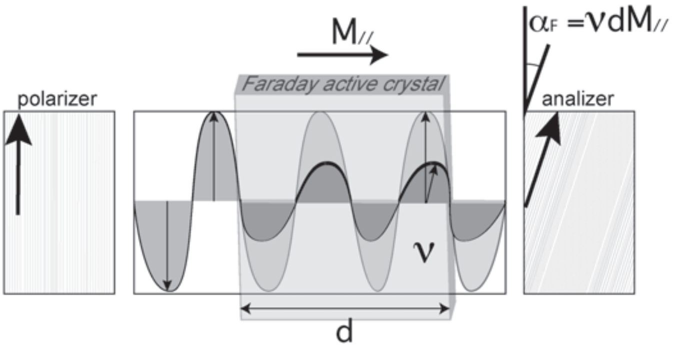

FIGURE 4.3: Principle of Faraday effect (1846) [67]: the polarization plane of the light refracted by the magneto-optically active media is rotated by an angle α_F proportional to the length of the light path into the media and to the local magnetization component along the light direction trough the Verdet constant, ν of the Faraday active material.

The original demonstration, for the Faraday effect, has been given for paramagnetic glass, but such effect is also observed when light traverses a diamagnet or a transparent, spontaneously magnetized, ferromagnet or ferrimagnet [30]. The polarization analysis of the refracted light results in the direct imaging of the local magnetic state of a material, in the form of light intensity variations, thus that, the refracted light, can be recorded by opportune rotation of a light polarization analyser.

4.2 Experimental setup

The main parts of the experimental setup in use at Politcenico of Torino are depicted in Fig.4.4 [26] [68]. The light beam, generated by a Hg lamp (1), is collimated by the use of a bi-convex lens (2) before passing through a polariser (3). At this point the light is linearly polarized. After the exciting filter (not drawn), the light hits a beam splitter (4) and is focused by the objective lens (5) onto the indicator surface (6). Since the aim is to perform measurements as a function of the temperature, the magneto optical active media (indicator film) is positioned inside a cryostat (7) furnished with a transparent window. An external magnet (8), cooled with water, generates a uniform magnetic field in the direction perpendicular to the indicator plane. Because of the aforementioned Faraday effect (Eq.(4.1)), the polarization plane of the light refracted by the imaging film is rotated. Such light passes then through the lens (5), the beam splitter (4) and the rotating analyser (9), before being focused by the camera lens (10) and captured in the CCD matrix of the videocamera (11). A PC (12) acquires the digital signal of the camera and elaborates it. Each part of the MO setup is crucial for the experiment, however, in the following, only the most important factors to obtain high quality images will be highlighted.

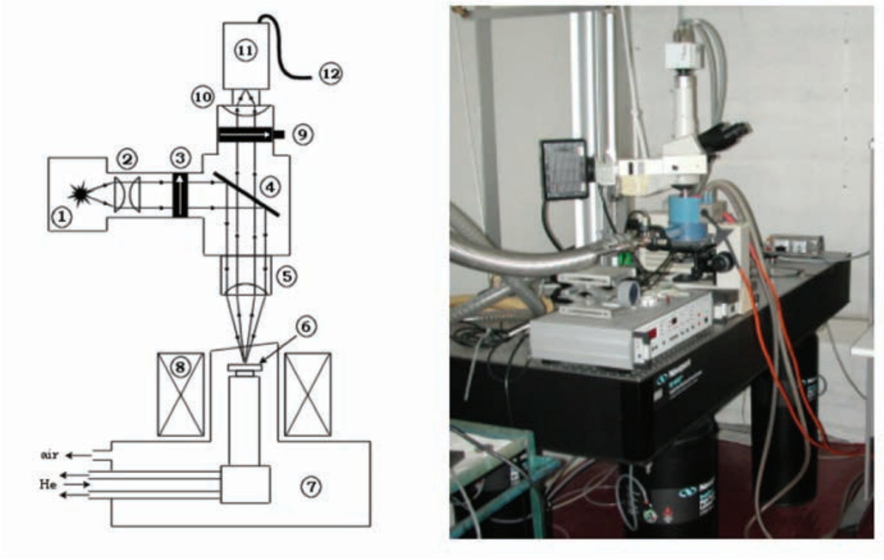

FIGURE 4.4: Scheme and photo of the experimental setup in use at Politecnico of Torino. The linearly polarized light beam is refracted by the imaging film before being focused by the camera lens and captured in the CCD matrix of the videocamera. [26]

4.2.1 The indicator film

As expressed in Eq.(4.1), the most important parameter for the MOIF technique is the Verdet constant of the employed imaging film ν, which is proportional to the angle of rotation of the light polarization plane and determines the strength of the Faraday effect.

For most materials, the Verdet constant is extremely small and wavelength dependent. Due to their large ν, during the last two decades, ferrite garnet single-crystalline films have become the defacto material for direct visualization of magnetic field microdistributions. Ferrite garnets $R_3^{+3}[Fe_3^{+2}](Fe_3^{+3})O_{12}$ have a cubic structure with rare earth and iron ions occupying different positions (R dodecahedral, [Fe] octahedral (antiferromagnetic or paramagnetic) and (Fe) tetrahedral (ferromagnetic) between oxygen ions. The uniqueness of

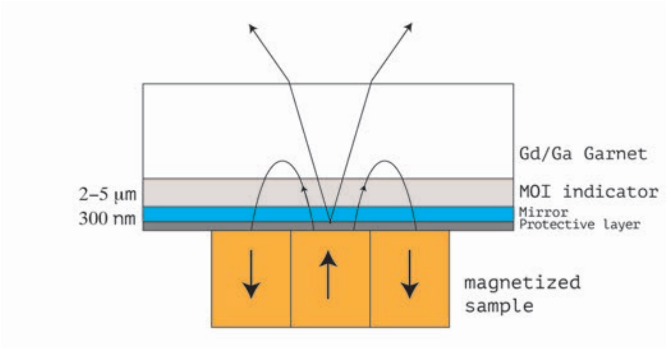

FIGURE 4.5: The stray field produced by a magnetized object below the indicator film induces the rotation of the magnetization vector in the indicator, producing a rotation of the polarization plane of the incident light. The layer configuration of the MO indicator is depicted in the scheme. The Ag mirror doubles the Faraday rotation of the refracted light.

this type of ferrites lies in their ability to produce an endless variety of physical properties by isomorphic substitutions of atoms in the three-sublattice garnet structure; moreover, the properties of ferrite-garnet epitaxial films may be substantially altered by choosing different substrates and growth conditions [66]. The thickness of the film can be varied from few hundred nanometers to several microns (best quality films can be generally grown between 0.5 and 6 μm). The imaging films in use in our setup are produced on the basis of the orthorhombic ferrite $Y_3Fe_5O_{12}$ (Yttrium Iron Garnet). The challenge for MOIF consists into a series of substitutions of iron (with Ga) and yttrium (with Bi) in order to obtain only ferromagnetic iron sites. The Bismuth-substituted ferrite garnets (BIG) are high-quality MO materials having specific Faraday rotation of an order of magnitude larger than bismuth-free crystals. In particular, the $Bi_3(Fe, Ga)_5O_{12}$ compound is characterized by a Giant Faraday Rotation (GFR) in all the visible spectrum. Reported values of the GFR-Verdet constant range in the order of 10^4 ° kOe^{-1} cm^{-1} [69]. Moreover, the Curie temperature of iron garnets is above 750 K and its ferromagnetic state is very stable down to low temperatures (T<1 K), allowing their usage at room temperature as well as in vacuum and at low temperatures. The indicator films are coated with a mirror layer on one side, so that the light passes through the film twice, enhancing then the sensitivity (doubling the effect) as showed by the scheme in Fig.4.6 (c), moreover the deposition of the mirror layer makes possible to visualize the magnetic field above any planar surface. The mirror, in the imaging film structure, is covered by a protective layer.

4.3 Quantitative Magneto-Optics

4.3.1 Model for the indicator films

The response of BIG has been described by a complete electrodynamical model of indicators with in-plane magnetization by Lars Egil Helseth [70]. The model takes into account in the Hamiltonian of the system for the uniaxial anisotropy energy (K$_u$), the Zeeman coupling with the external field and the demagnetisation energy. An approximation of the extended Halmiltonian results in:

$$E_{int} = E_a(1 - cos\phi) + BM_s[1 - cos(\beta - \phi)], \tag{4.2}$$

where μ_0E$_a$ = μ_0M$_s^2$-2K$_u$, while β is the angle between the magnetic induction vector and the xy plane, where the spontaneous magnetization lies in absence of external fields (see scheme on the left of Fig.4.6). With respect to the scheme, on the basis of this equation it is possible to obtain the relation for the angle ϕ which accounts for the perturbation of the magnetic moments inside the BIG, yielding to its equilibrium solution:

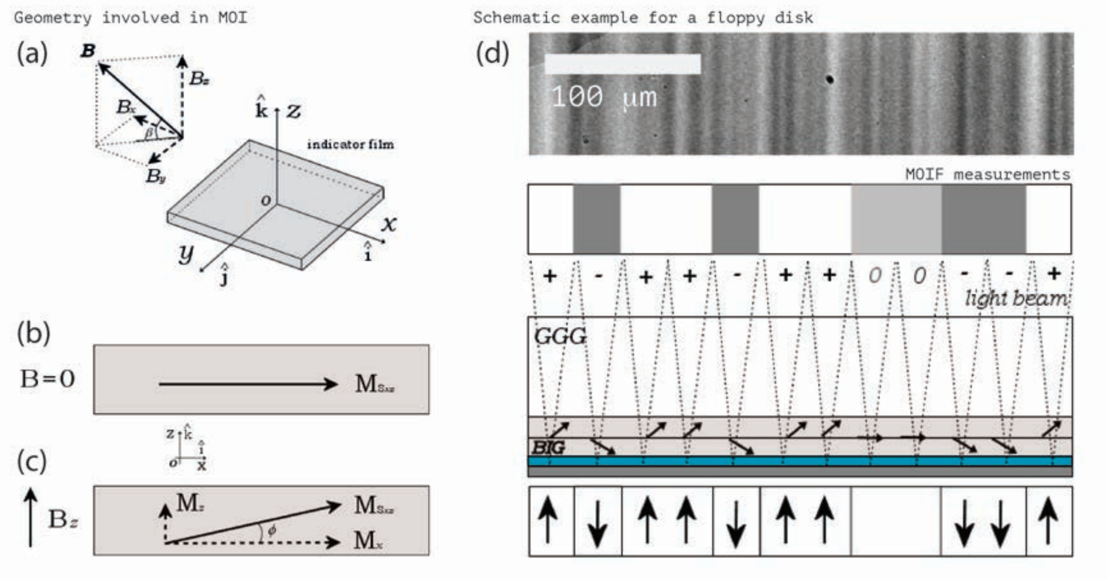

FIGURE 4.6: (a) xyz coordinates involved in the MO indicator. (b)(c) The saturation magnetization of the indicator lies, at first, in the plane of the indicator (B_z = μH_z = 0), then it rotates, by an angle ϕ, in the z direction if external fields are provided. (d) Scheme of the light path and a relative image obtained with MOIF for a floppy disk track.

$$\phi = \frac{B_z}{B_{xy} + B_A}. \tag{4.3}$$

where B_A = $\frac{E_a}{M_s}$, B_z = $\vec{B} \cdot \hat{k}$ = $Bsin\beta$ and B_{xy} = $\sqrt{(\vec{B} \cdot \hat{\imath})^2 + (\vec{B} \cdot \hat{\jmath})^2}$ = $Bcos\beta$ [26].

The polarization plane of the incident light is rotated by the Faraday effect and the amount of such a rotation, indicated by the angle α_F, is proportional to the magnetisation component along the light direction. In the current MOI experiment it is assumed the simple relation:

$$\alpha_F = CM_s sin\phi \tag{4.4}$$

where C is the optical-coupling parameter which depends on the thickness and chemical composition of the indicator film [26]. The whole set of the indicator parameters must be evaluated separately for any experimental condition, since the parameters characterising the garnet are stable just in small temperature ranges.

4.3.2 Analysis of the Faraday rotation angle

The analyser, positioned after the reflected beam, is used to detect the Faraday rotation angle of the Garnet, α_F. The analyser is fixed at an angle θ off the polariser direction (commonly 2/3°off the crossed condition). The light intensity I, received by the video camera, can be evaluated by using a simple form of the Malus law, where all the Fresnel integral due to the light path trough the optical constituents of the setup, other then the BIG, are neglected for the calculus. The simple form for the light intensity can be expressed as:

$$I = I_0 + I_{max}cos^2(\alpha_F + \theta). \tag{4.5}$$

I_{max} is the light intensity of the incident beam and I_0 is the intensity of the not-linearly polarised light. Combining the equation (4.5) with (4.4) and (4.3), the relation between the measured light intensity and the magnetic induction results in:

$$I = I_0 + I_{max}cos^2\left[\frac{CM_sB_z}{\sqrt{(B_a + B_{xy})^2 + B_z^2}} + \theta + \nu B_z d\right]. \tag{4.6}$$

This equation is the final model for relating the measured light intensity to the local magnetic field acting on the indicator [26] and will be used in 4.4.2 to calculate the z component of the stray field produced by the MCE sample.

4.4 MOIF in La(Fe$_{0.9}$Co$_{0.015}$Si$_{0.085}$)$_{13}$

The use of the present MOIF technique, for the study of the phase transition in magnetic materials and, in particular of MCE compounds, is motivated by the possibility to use the setup at different temperatures and to capture real time images of large areas of the investigated samples. This fact permits to instantaneously observe the global response of a relatively large surface (several millimetres), thus to correlate the MOIF signals with other magnetic properties which can be measured by standard magnetization techniques (magnetization

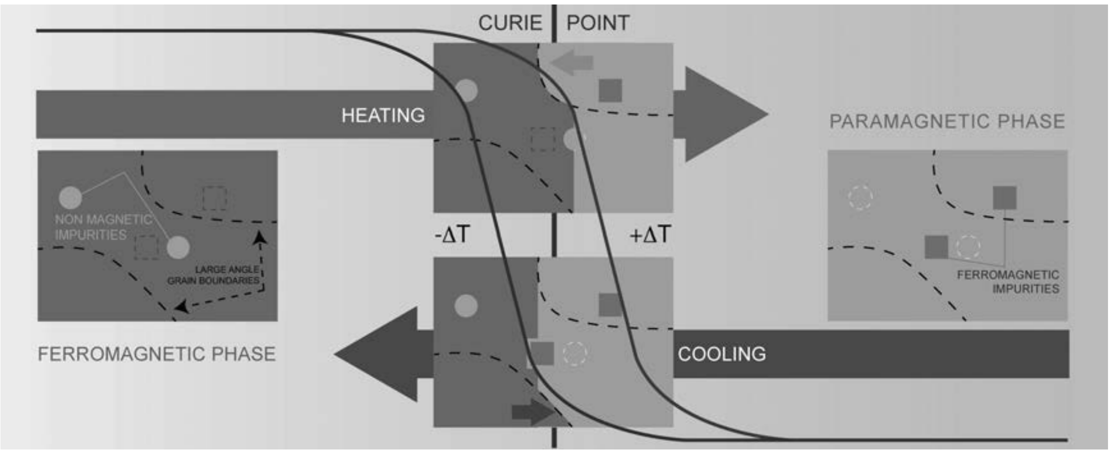

susceptibility, magnetic entropy,...). In the last decades, few optical visualisations of the phase transition in MCE compounds have been published. Among those, Kawamoto used a Lorentz microscopy technique in Fresnel mode on La(Fe$_{0.895}$Si$_{0.105}$)$_{13}$ and La(Fe$_{0.90}$Si$_{0.10}$)$_{13}$ compounds [71][72][73]. In these works, the authors visualized the domain walls of the ferromagnetic phase just below their Curie temperatures and they captured, close to T_c, the coexistence of the PM/FM phases. The experiments helped to correlate the pinning of domain walls with grains boundaries. Another important result was the reproducibility of the domain wall positions. Despite of the amount of temperature cycles performed, the authors didn't find any lattice defects arising from the magneto structural transformation, however, in spite of the great spatial resolution used to visualised the magnetic domains, just a small fraction of the samples surface was investigated. In 2014, MFM images of the surface of a piece of La(Fe$_{0.9}$Co$_{0.015}$Si$_{0.085}$)$_{13}$ were published by Lollobrigida et al. [74].Varying the external magnetic field, a ferromagnetic signal was detected above the Curie temperature: such ferromagnetic response was attributed to a secondary $\alpha - Fe$ phase embedded in the matrix and imaged with MFM and it was correlated with X-ray Magnetic Circular Dichroic (XMCD) spectra acquired above and below of the compound Curie temperature ($\sim$ 200 K). The Scanning Hall Probe Technique (SHPM) has also been applied to phase transitions in other several magneto caloric candidates. A study, performed by Morrison et al., on the MCE compound CoMnSi$_0$.92Ge$_0$.08 [75], disclosed the differences in the magnetic response recorded at single sites or considering a larger portion of the sample surface (1 mm^2) collected by means of the SHPM technique. On the local scale, below the Curie temperature, both ΔH and the applied field, were observed to be much smaller then those for the total area, Fig.4.7. The existence of such a difference was attributed to the spatial separation of the transition and they also observed, that local sites could posses different Curie temperatures because of inhomogeneity. Since the transitions in La(Fe,Si)$_{13}$ based compounds are magneto structural, literature attention has been also devoted to the observation of the spatial evolution of the front by means of volume measurements. Waske and collaborators published the reconstruction of the volume expansion/contraction [59] measured with a tomography technique in a

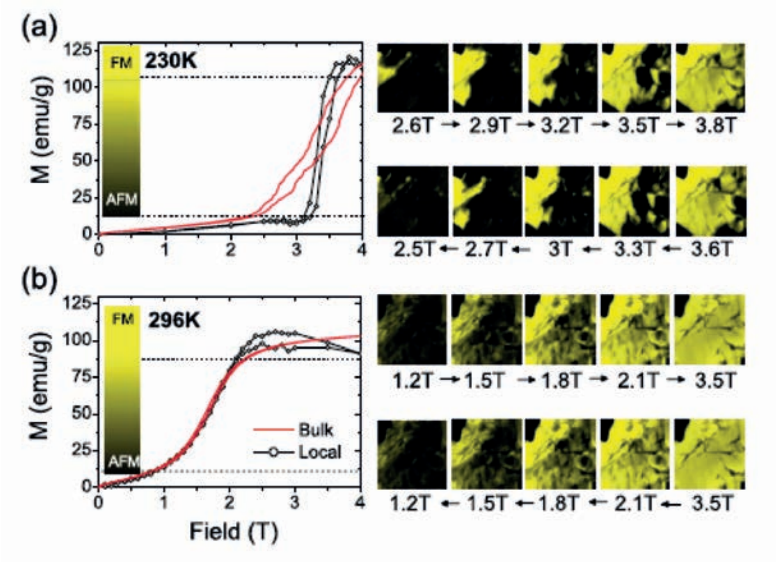

FIGURE 4.7: Hall probe imaging of CoMnSi$_0$.92Ge$_0$.08 across the field driven magnetic transition: (a) first order transition at 230 K, (b) second order transition at 296 K. Left: The M vs H loops constructed from a single pixel (dotted black line) of a series of images are shown at these temperatures alongside bulk measurements (continuous red lines). Right: Equivalent up-field and down-field images are shown to highlight reversibility of this sample. Each image is 1 mm across. Dark areas in the magnetically saturated images indicate the presence of cracks in the sample surface or the sample edge top left corner, which were used as location markers [75].

LaFe$_{11.8}$Si$_{1.2}$ sample. They found differences in the nucleation sites of the new FM phase, which were shown to strongly depend on the surface morphology of their sample (valley, peaks or planar regions pf the surface). With respect to previous works, the in-temperature indirect MOIF technique was here firstly applied on a MCE compound. The technique allowed to simultaneously detected the change in the stray fields of the main magneto caloric phase and also of the secondary phases present in the compound La(Fe$_{0.9}$Co$_{0.015}$Si$_{0.085}$)$_{13}$, while imaging the entire surface of the sample.

Sample details

A sample of polycrystalline Co substituted La(Fe$_x$Co$_y$Si$_{1-x-y}$)$_{13}$ with x=0.9 and low Co content of y = 0.015 and T$_c$ = 200 K was prepared by powder metallurgy at Vacuumschmelze GmbH and CoKG [49]. The elemental analysis was performed by energy dispersive X-ray spectroscopy in a Scanning Electron Microscope (SEM) on a polished surface of the sample. Fig.4.8 shows a representative area of the sample and the distribution of the constituent elements based on their X-ray characteristic energies. Two secondary phases can be distinguished from the La(Fe,Co,Si)$_{13}$ matrix: $\alpha - Fe$ grains and a LaO rich phase with bright contrast in backscattered electrons images which might be also conducted to the

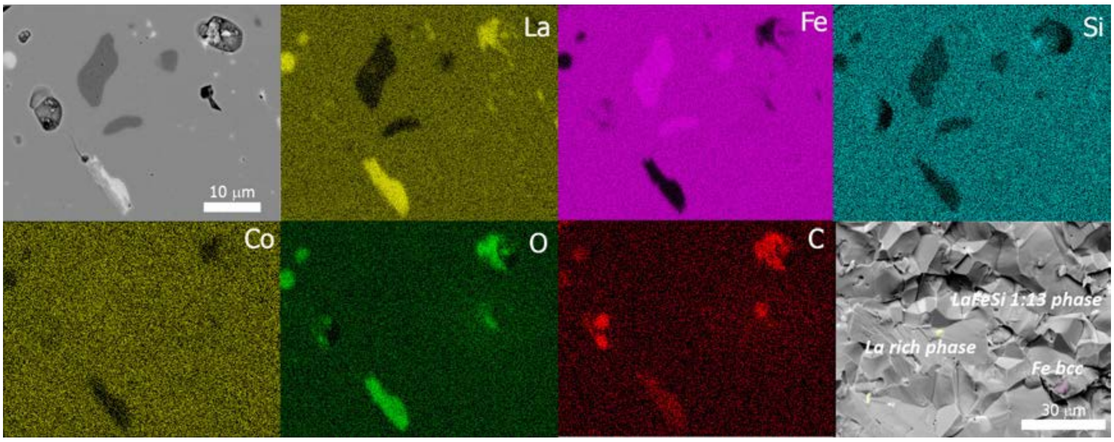

FIGURE 4.8: SEM backscattered electrons image of sample surface and elemental X-ray maps of the area; the characteristic X-ray energies of selected elements (La, Fe, Si, Co, O, C) are represented in false colors. The bottom right image shows fracture surface of the sample where grains of the MCE phase are in grey and other phases are highlighted with the same colors of the X-ray maps [76].

(1:1:1) phase of the peritectic reaction: $\alpha - Fe$ + LaFeSi $\longrightarrow$ La(Fe,Si)13 [77]. The carbon enriched spots are likely associated with diamond debris and organic matter accumulation in the pores of the sample, resulting from the sample polishing process. The $\alpha - Fe$ grains and the pores have typical sizes which span from 5 μm to 30 μm. In the last frame of Fig.4.8, a fractured surface is presented, showing the typical grain size of the (1:13) MCE phase.

Two fragments of the same sample were used for the experiments with masses below 10 mg. The MOIF experiments were performed utilizing an imaging film with Bismuth Iron Garnet (BIG) as MO indicator. Both samples were mounted on the cold finger of the cryostat and covered with the indicator film. The temperature in the cryostat was monitored with a cernox thermometer mounted on the top of the cold finger and it was varied by using liquid He flux and a heater (scheme in Fig. 4.9).

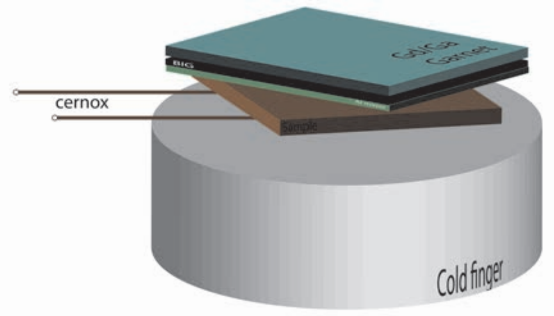

FIGURE 4.9: Scheme of the mounted sample inside the cryostat for the optical visualization by indicator film.

4.4.1 Spatial evolution of the magnetic front

A qualitative observation of the spatial separation of the phases during the first order PM/FM (and vice versa) phase transition was performed on a first sample, whose optical image is reported in Fig.4.10.

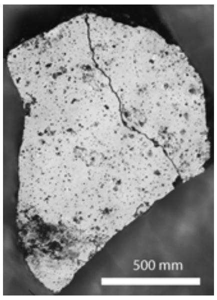

FIGURE 4.10: Optical image of the sample.

The thickness of the specimen was estimated of about 400 μm. Since the transition in La(Fe$_{0.9}$Co$_{0.015}$Si$_{0.085}$)$_{13}$ is expected at around 200 K, the images were acquired in the temperature range [195-215] K. In order to magnetize the sample and then to gain in magnetic contrast, we applied a small external magnetic field of 3 mT. The acquisition time stamp between subsequent images was 180 ms. The whole sample was visualized and monitored using a $10X$ magnification, corresponding to a spatial resolution of 3.4 μm per pixel. In all the subsequent MOIF images, a bright area corresponds to a magnetic field pointing toward the reader, while a dark area corresponds to a magnetic field toward the paper, with respect to the grey background level (0 applied magnetic field). The grey scale can be considered as being proportional to the local stray field at the sample surface (out-of-plane component, B$_z$), but for a correct evaluation of these values a calibration of the system is necessary, as it will be described in section 4.4.2. The frames showed in Fig.4.11 are selections of the heating and cooling sequence of images across the Curie point of 200 K. The temperature was varied at a heating rate of 69 mK/s and at a cooling rate of 123 mK/s. All the magnetic contrast derives from the magnetized La(Fe$_{0.90}$Co$_{0.015}$Si$_{0.10}$)$_{13}$ sample. Starting from the first frame of the top row, the sample passes from being slightly contrasted with respect to the surrounding space (at 202.3 K) to become bright and clear in the last frame recorded (at 189.71 K). In this last frame, the shape of the optical image of Fig.4.10 is clearly recognisable. The randomly sparse bright spots of the first images (also observable in the subsequent images) are mainly due to other phases at the surface, which can be magnetic, or to defects, which can press the mirror of imaging film. During the in-temperature acquisition, as soon as the Curie point was crossed, part of the sample went through the PM to FM transition and the corresponding sample area lighted up. In fact, the bright large areas of each image, correspond to an increased Faraday rotation angle of the magnetization vector into the BIG, due to a larger out of plane component of the local stray field of the sample. The frames show that the FM/PM front moves across the sample area following a precise pattern. By comparing sequences of frames in the top and bottom rows of Fig.**??**, it is possible to observe that the positions of the front are almost the same during heating and cooling. The three main features which dominate the dynamics of the front motion, in the plane of the sample surface, are: a slow growth of the new phase, the pinning of the front at some reproducible sites and some fast events in which big parts of the sample transform almost instantaneously. As an example, comparing the frames 9(a) and 10(a), it appears that a large area of the bottom part

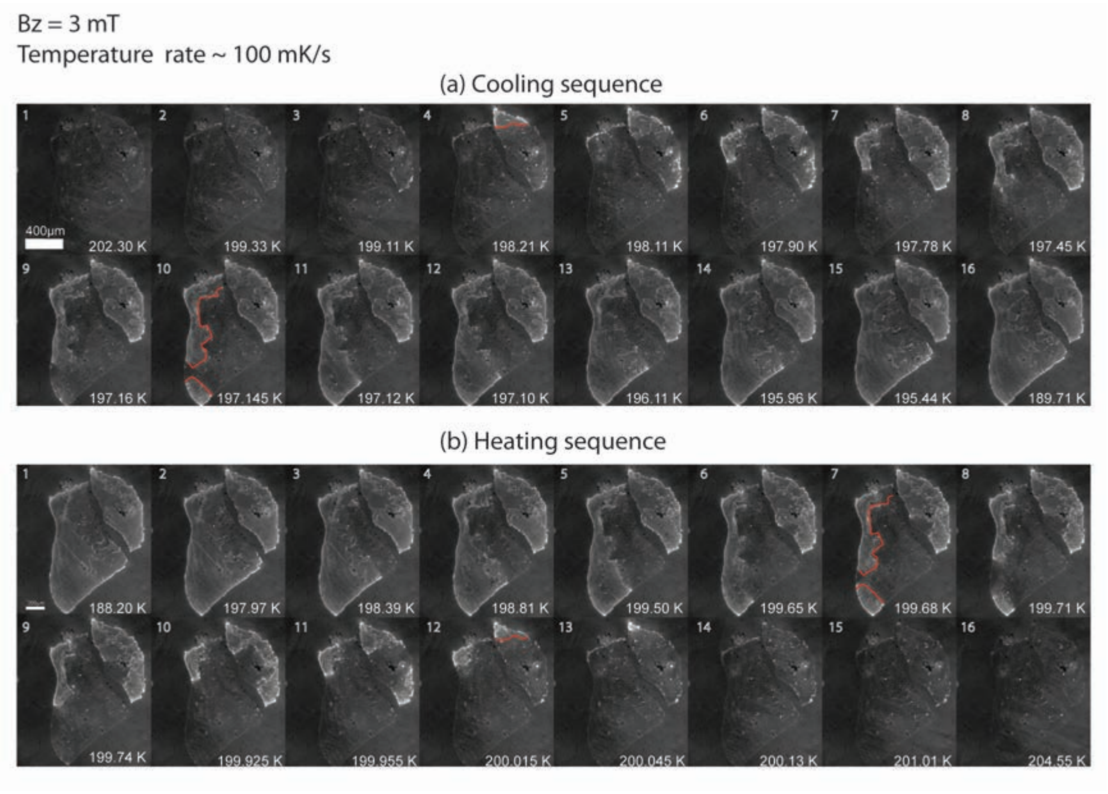

FIGURE 4.11: Selected MOI frames at temperature rates of 69 mK/s (cooling: top rows) and of 123 mK/s (heating: bottom rows). The first and the last images show the relatively pure PM or FM phase (or vice-versa), while the others show phase coexistence. Uniform out-of-plane induction field: 3 mT. The FM phase (brighter parts) displays much larger magnetic flux density than the PM phase (darker parts).

of the sample transforms faster then in the subsequent 11(a) and 12(a) frames. The fast events are not resolved in the time between two acquired frames and are the ones responsible for a jump wise fashion of the 2D front motion; they are position dependent independently on temperature rates and applied fields. As pointed out in the introduction, the spatial magnetic phase separation, here visualized by the help of MOIF, gives strong support to the first order nature of the observed FM/PM transition; on one hand because the concomitant observation of the two phases at the transition, on the other hand, due to the different transition temperatures of the heating and cooling sequences (see frames 10(a) and 7(b) for example). In order to quantify the two observed dynamics, the speed of the 1D front was estimated by assuming a linear advancement from one image to the next until a pinning centre was reached. The speed of the fast events appears to be faster then 4×10^{-3} m/s, while the front which propagates continuously has a speed of the order of 1×10^{-4} m/s. These results suggest an a-thermal character of the phase transition in which the transformation process is dominated by the pinning of phase boundaries at defects rather than by the nucleation and growth processes.

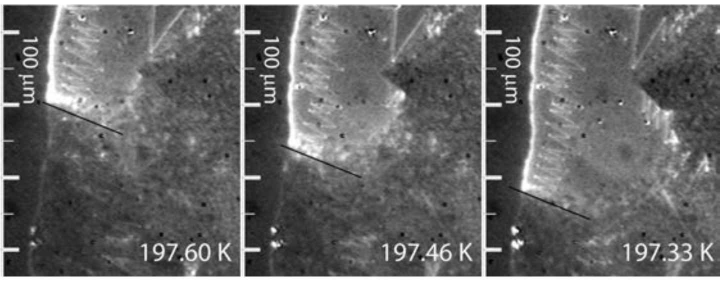

FIGURE 4.12: The average velocity of the smooth propagation of the front was calculate to be 4X10^{-4} m/s, while the fast propagation of the front is faster then the acquired time between frames (> 1X10^{-3} m/s).

4.4.2 Quantitative analysis of the stray field

The previous sequences of MOIF images were not calibrated, thus they just furnished a qualitative description of the magnetic response of the sample. In order to extract the values of the sample stray field, B_z, responsible for the Faraday rotation inside the BIG, a calibration procedure was performed. The calibration is needed for each temperature of measure, in order to avoid the possibility that any temperature driven change in the BIG physical parameters affects the measure of B_z. For this reason, at any temperature of interest, a sequence of images as a function of the external applied magnetic field, H_a, was recorded and then it was mathematically treated before obtaining the B_z field dependency.

Calibration procedure

The evaluation of B_z starts with the measured light intensity, I, converted in digital values by the CCD camera. Such values are related to the properties of the camera itself (pixel depth, gain, etc.) and to the number of photons collected by the CCD sensor, they are therefore the result of a relative (to the camera photon range) measurement of the light intensity over the MOI indicator surface. To make the calibration procedure possible, it is important to acquire, in the same image, the whole area of the sample together with a large area of the BIG far from the sample stray field. The recorded light intensity thus comes from two main zones of the image: a region where the indicator film reacts only to the external magnetic field, H$_a$, and a region where the indicator reacts to the sum of the applied magnetic field and the dipolar field produced by the sample, H$_d$. A scheme is reported in Fig.4.13. In both regions (grey and orange areas of Fig.4.13), the light intensity of the indicator film is given by the Eq.(4.6) of section 4.2.1, which was obtained combining the Faraday rotation effect of the BIG and the Malus law for the analyser.

The hysteresis loops in the area where the BIG reacts only to the external applied magnetic field (i.e dark grey areas) were the ones used to calibrate the BIG response to an external magnetic field. The applied fields were generated

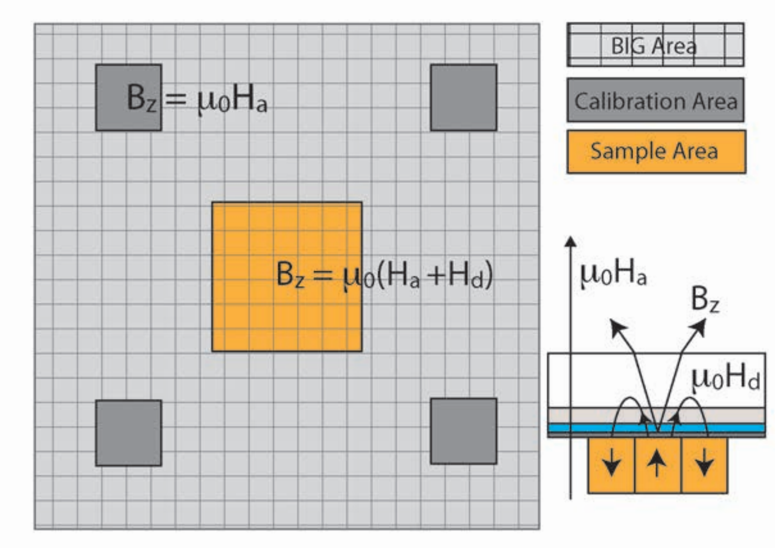

FIGURE 4.13: Scheme of the image area acquired for the calibration procedure. The orange area represent the part of the indicator film which reacts to the stray field of the sample. The mean values of the light intensity in four different areas (typically the corners of the images, dark grey squared areas) are used to fits with the calibration curve.

in the range of [-750,750] Oe ([-75,75] mT). The obtained series of images, at constant T, were subjected to the following operations:

- IMAGES ALIGNMENT. Since the experimental conditions (temperature and magnetic field) are varying, they can produce a slight movement of the optical components. To be able to correctly observe the response at pixel sites, the sample has to occupy the same pixel position along the entire sequence.

- NORMALIZATION OF THE INTENSITY VALUES. All the images of each sequence were normalized by their maximum and minimum values of the acquired I (respectively the image at which the applied field is maximum and the one in which H_a = 0 T.). This operation permits to reduce the calibration curve of Eq.4.7 for the BIG to the following expression:

$$\frac{I_{BIG}(H) - I_{BIG_0}}{I_{BIG_{max}}} = cos^2(\theta - \nu x - \frac{C M_s x}{\sqrt{B_a^2 - x^2}}). \tag{4.7}$$

In the last equation, suitable for the fit, x represents the external applied magnetic field, while the in plane component B_{xy} of Eq.(4.6) has been neglected for the calculus. A detailed discussion about the in plane field B_{xy} can be found in [26]. An example of the calibration curve of the BIG magnetic field response is shown in Fig.4.14 for a sequence of images recorded at 195 K; typical values obtained from the calibration procedures at different T are listed in Tab.4.1. The calibration curve permits to relate each I value, recorded by the CCD

T (K)	CM$_s$	I$_{BIG_{max}}$	I$_{BIG_0}$	B$_a$ (Oe)	ν	θ
185 K	0.195	14	-0.3826	2000 Oe	-1E-5	1.404 rad
195 K	0.1939	14	-0.38072	2000 Oe	-1E-5	1.404 rad
215 K	0.2365	12	-0.3169	1900 Oe	-1E-5	1.406 rad

TABLE 4.1: Calibration values obtained at different temperatures for the BIG response using Eq.4.7. Each set of parameters is used to quantitatively evaluate the sample stray field.

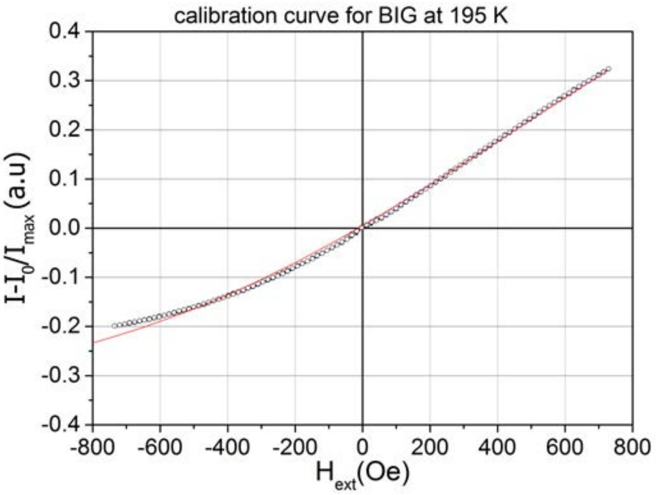

FIGURE 4.14: Example of calibration curve for the BIG response performed at 195 K.

camera, to the value of magnetic field acting on the BIG. After this operation, the light intensity values of the sequence of images at each pixel site can be calibrated following the indicator response and the correspondent values of B$_z$ can be obtained by inverting Eq 4.7.

4.4.3 Magnetic phases at the surface

The sample used for the quantitative analysis is reported in the left frame of Fig.4.15. The optical image (a) is compared to the not calibrated images taken at temperatures above (c) and below (b) the Curie point of $\sim$ 200 K . The out of plane stray field component of the sample, B$_z$, cannot be directly related to the value of the magnetization of the sample. The first reason is that the external applied field is not sufficiently high to align all the spins of the sample in the z-direction [78]. In fact, the value of the saturation magnetic field [74] of the La(Fe$_{0.9}$Co$_{0.015}$Si$_{0.085}$)$_{13}$ is higher than the applied $\mu_0 H_a$ = 75 mT. The second problem arises from demagnetizing factors due to magnetic anisotropy and shape. The last could be eliminated only if the shape of the sample under investigation is controlled, but, as it is possible to see in the optical image of Fig.4.15 (a), the sample under investigation had an irregular shape and its thickness was about 200 μm, making the geometrical demagnetizing factor hardly estimable.

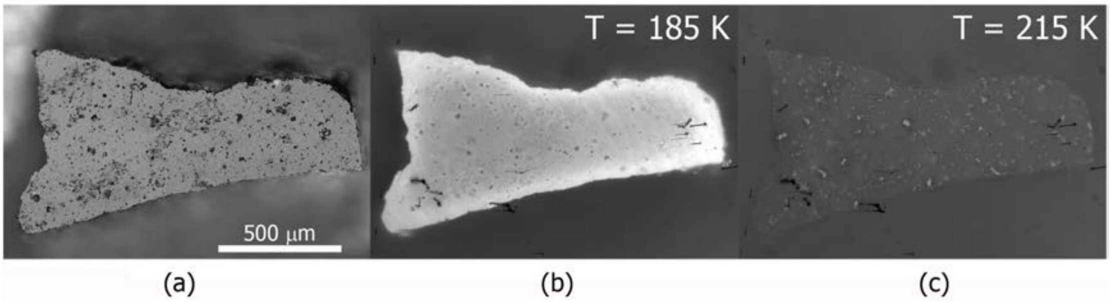

FIGURE 4.15: (a) Optical image of the entire sample. MOIF images of the magnetic contrast in the paramagnetic (b) and ferromagnetic phase (c).The dark spots in the FM phase of the sample (T = 185 K) mainly correspond to the holes of the optical image, while the bright spots in the PM phase (215 K) do not have a counterpart in the optical and FM images. In the MOIF images, the external magnetic field (75 mT) is pointing out of the images plane.

The magnetic anisotropy depends on the magnetic properties of the sample, and it was ignored due to the soft ferromagnetic properties of the La(Fe,Si)$_{13}$ series. Consequently, considering that all magnetization components count in the magneto static equation of the stray field, to comment the magnetic properties obtained by MOIF, the following generic formula will be used:

$$B_z = \mu_0(H_a + H_d(M(x,y,z)), \tag{4.8}$$

the last term representing the dipolar field of the sample which also depends on the z-component of the magnetization.

Fig.4.16 reports an highly contrasted image of the sample in the PM phase, after applying the calibration, for zero external magnetic field. The line profile, which crosses the surface of the sample, shows an almost zero value of the background, equal to the values inside the sample. A small remanence appears at the border of the sample due to the small magnetic response of the PM phase, close to the Curie temperature.

Examples of the two MOIF images at the two temperatures of interest after applying the calibration procedure are shown on the top row of Fig. 4.17. Differently from the not calibrated image of Fig.4.15(c), in the paramagnetic phase the MOIF contrast between the sample matrix and the background is almost null. This fact is clearly visible in the zoomed regions at the bottom of Fig.4.17. On the contrary, when the temperature is tuned below the T_c, the magnetization of the FM phase lights up the sample shape (left image of Fig.4.17). The two images of the FM/PM phases in Fig.4.17 are represented with the same colour scale, highlighting the differences in their magnetic signals. The main features that appear comparing the calibrated images are summarized below:

- The overall B_z value of the sample at 185 K is greater then the value at 215 K;

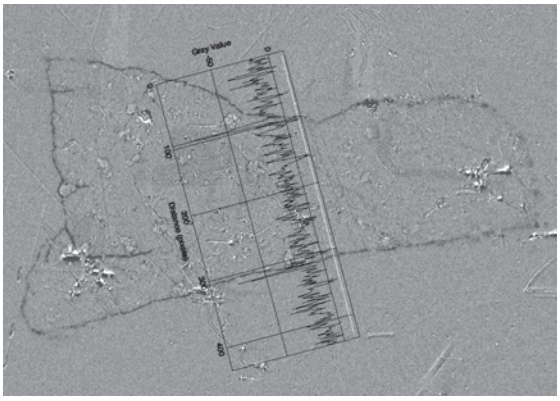

FIGURE 4.16: Values of the stray field produced by the sample and by the background in zero external applied magnetic field. The sample is in the paramagnetic phase (215 K): the sample and the background posses the same level of magnetic contrast. The pixel lateral size is 1.67 μm.

- Small randomly sparse regions, characterized by a higher stray field with respect to the matrix, are present in the PM phase of the sample at 215 K. Such regions will be named ferromagnetic grains in the rest of the discussion;
- Small randomly sparse regions, characterized by a lower stray field with respect to the matrix, are present in the FM phase of the sample at 185 K. Such regions will be named magnetic holes in the rest of the discussion;
- the ferromagnetic grains occupy different positions with respect to the magnetic holes across the surface, as it is highlighted by the zoomed regions of Fig.4.17.

The first observation is quantitatively represented in the graph at the bottom right of Fig.4.17, where the small fields hysteresis loops of the sample in the two phases are compared. The values of B_z are plotted on the y-axis. These values were calculated from Eq.4.8 and integrated over the whole surface of the sample at each external applied magnetic field. At temperatures below 200 K, the z component of the stray field is magnified by a factor of ~ 2 with respect to the PM phase. Since the positive magnetic permeability of a ferromagnet increases the density of the magnetic field flux lines inside the specimen, it produces an higher value of the stray field. Being able to phenomenologically distinguish between different responses of B_z, depending on the magnetic properties of the sample, a model for these hysteresis loops was constructed with the following phenomenological equation:

$$\mu_0(H_{meas} - H_a) = aH_a - bH_a^3. \tag{4.9}$$

In such a way two parameters were extrapolated: the first one, a, proportional to the external field which is conductible to the internal magnetic response of

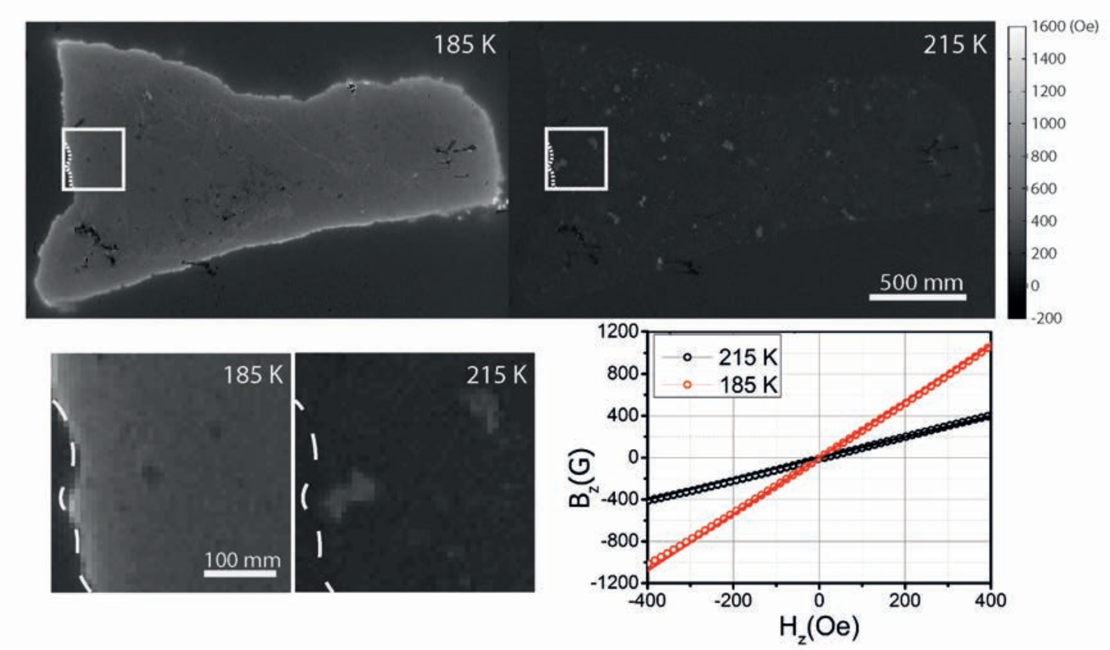

FIGURE 4.17: Top figures: calibrated images for 185 K and 215 K of the entire surface of the sample. The grey scale shows the intensity corresponding to the value of the stray field coming from the local sites of sample. Bottom right graph: Integral of the stray field calculated from the entire surface of the sample, with hysteresis loops for 185 K and 215 K.

the sample and the second one, b, which is a correction factor proportional to the cube of the external applied field.

The results of the fitting with Eq.(4.9) for the hysteresis loops at the two temperatures are shown in Fig.4.18. The values obtained for the parameter a are respectively 0.09 and 1.54 in the PM and the FM phase.

4.4.4 Analysis at single sites

As it was observed in the previous section, beyond the main PM/FM phases, the sample surface is characterized by other magnetic phases: the ferromagnetic grains visible in the PM phase and the magnetic holes visible in the FM phase. With the purpose to analyse these features, the hysteresis loops at each pixel position were collected performing single fits using Eq.4.9. Examples of the collected loops are reported in Fig.4.19 for some random sites on the surface.

Figs.4.20 (c) and (d) show the maps of the values of the parameter a for each pixel at temperatures above (T = 215 K) and below T_c (T = 185 K). These maps and their statistical distributions (Fig. 4.20 (a) and (b)) permit to distinguish different magnetic phases depending on the values of a. In particular, when T > T_c, the main MCE phase of the sample behaves as a paramagnet (a = 0.09), while the minor phase of the ferromagnetic grains possesses values of a = 0.78. Due to this magnetic difference, the ferromagnetic grains were attributed to the α - Fe secondary phase observed in the SEM images of Fig.4.8. It has to be noted

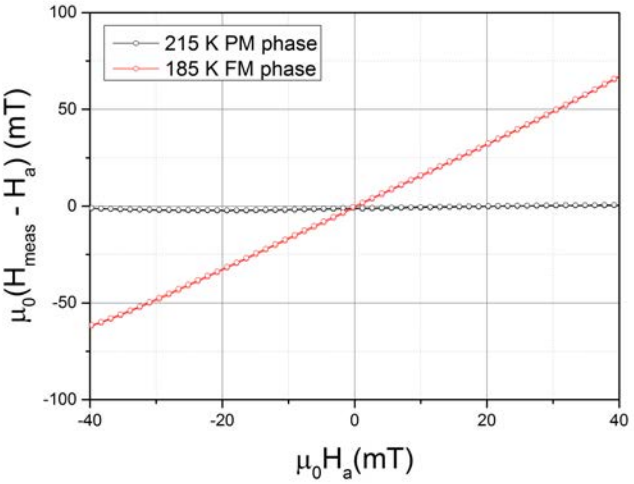

FIGURE 4.18: Hysteresis loops collected for the PM and FM phase according to Eq.4.9. The loops show different values of the linear coefficient a for the two temperatures above and below T_c.

that, in spite that the technique wasn't able to measure the value of the magnetic permeability of different phases, the distinction between a ferromagnetic or a paramagnetic behaviour was supported by the other experimental observation such as the SEM analysis and to the existence or absence of remanence signals after hysteresis loops. It was that considered reasonable to discriminate between a values close to zero for paramagnetic behaviour and values of a close to 1 for ferromagnetic behaviour. When T < T$_c$, the value of a of the ferromagnetic MCE phase overlaps with the value of a measured at the α - Fe sites, the respective mean values being 1.54 and 1.37. Moreover, at this temperature, local minima values of the parameter a = 0.95 randomly sparse at surface represent either magnetic holes or local sites where the transition does not occur above 185 K. Table 4.2 summarizes the values of the parameter a measured at T = 185 K and 215 K for the three different observed magnetic phases: the MCE main phase, the α- Fe grains and the magnetic holes.

	a	
phases	185 K	215 K
MCE phase	1.54	0.09
$\alpha - Fe$	1.37	0.78
magnetic holes	0.95	0.10

TABLE 4.2: Summary of the mean values of the linear coefficient a calculated for different phases and defects above (215 K) and below (185 K) the T_c.

These values have been calculated as the average of the statistical distributions of local pixels (grains) reported in Fig.4.20 (a) and (b). Both the $\alpha - Fe$

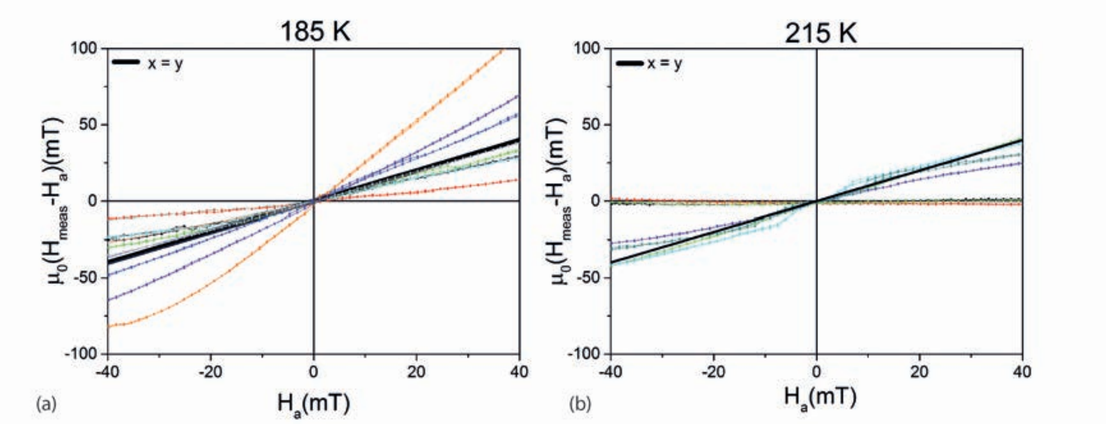

FIGURE 4.19: Example of hysteresis loops collected at pixel sites at the two temperatures 185 K (a) and 215 K (b). The hysteresis loops show a distribution of values of the coefficient a of Eq.4.9.

grains and the magnetic holes represent a fraction lower than 2% of the total sample surface. As already stated, at T = 185 K, the statistical distributions of the main MCE phase and $\alpha - Fe$ grains collapse to a similar value. This can be a confirmation of what was observed in [74], where the authors found a peculiar behaviour in the ferromagnetic X-ray magnetic dichroism signal of isolated ferromagnetic grains present at the surface, which disappears below the Curie temperature. Above T_c, the $\alpha - Fe$ grains are ferromagnetic and their stray field can be clearly observed. Below T_c, also the matrix becomes ferromagnetic and the flux of the $\alpha - Fe$ grains can not be observed by MOIF since it is closed into the matrix. From the statistical distributions in Figs.4.20 (a) and (b), it is also possible to note that the magnetic holes have a large distribution of a when T = 185 K, whether at higher temperature they behave as the rest of the PM phase. This effect is attributed to the local stray fields of the ferromagnetic main MCE phase, which deviate due to the shape and the magnetic irregularities produced by the magnetic holes at their surfaces.

4.4.5 Temperature induced phase transition

After the characterization of the magnetic phases present at the surface of the sample, their role in the dynamics of the magnetic phase transition was analysed. By changing the temperature around the Curie point, the time-temperature sequences of images with a resolution of 200 ms/frame were collected, permitting to map the discontinuous transition from the PM to the FM state (and vice versa) of the MCE main phase. The temperature scanning rates in use were 11 mK/s and 15 mK/s respectively for the heating and for the cooling of the sample. In these measurements, the external magnetic field was fixed at 30 mT, perpendicular to the sample surface. To calibrate the in-temperature image sequences, the response to external applied magnetic fields of the imaging film was measured at fixed T, both at the beginning and at the end of the temperature acquisitions. For these two temperature sequences, the fit parameters of Eq.(4.7) were found to be compatible with the values of Table 4.1, obtained at T

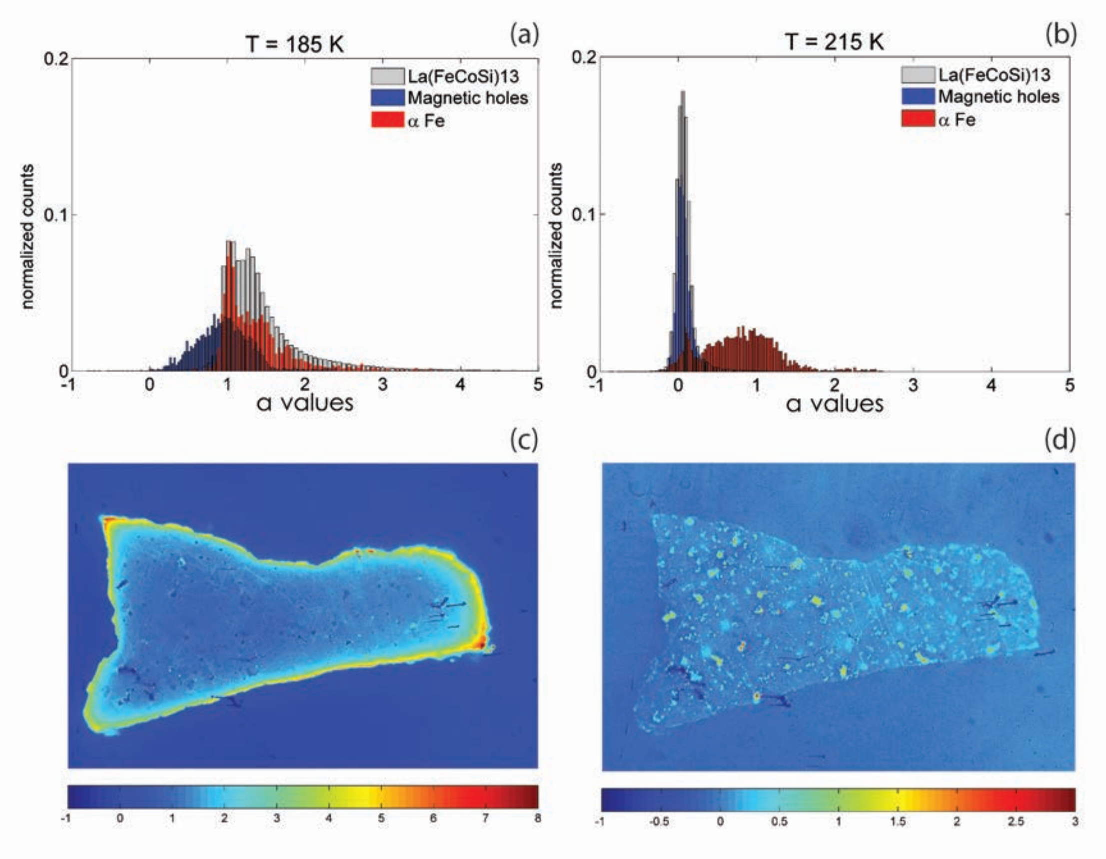

FIGURE 4.20: (a)(b) Statistics of the values of a at $\alpha - Fe$, magnetic holes sites and of the MCE phase below and above the Curie temperature. (c)(d) respective local maps of the magnetic linear response across the sample. The numbers of the counts have been normalized to allow a comparison with the minor percentage of other phases ($< 2\%$ of the total surface) [76].

= 195 K. In this way, it was possible to obtain the variation of the stray field generated by the whole sample during the in-temperature transition and to compare differences during the heating and the cooling processes. The magnetic flux across the open top surface of the sample (at the distance of the garnet) was obtained by calculating the integral of the scalar product of the measured stray field z-component with the orthogonal surface of the sample.

$$\Phi(\vec{B}) = \oint \vec{B} \cdot \vec{n} dS. \tag{4.10}$$

This equation provides a physical quantity which can be compared to the magnetic properties of the sample. Similarly to the result of section 4.4.1 either during heating or during cooling, the growing of the new phase is observed to proceed with some fast transformations of volumes separated by a slow motion of the front. These two dynamics correspond respectively to jumps and almost linear and continuous changes in the calculated total magnetic flux, as reported in the left graph of Fig.4.21. The frames corresponding to a particular path are

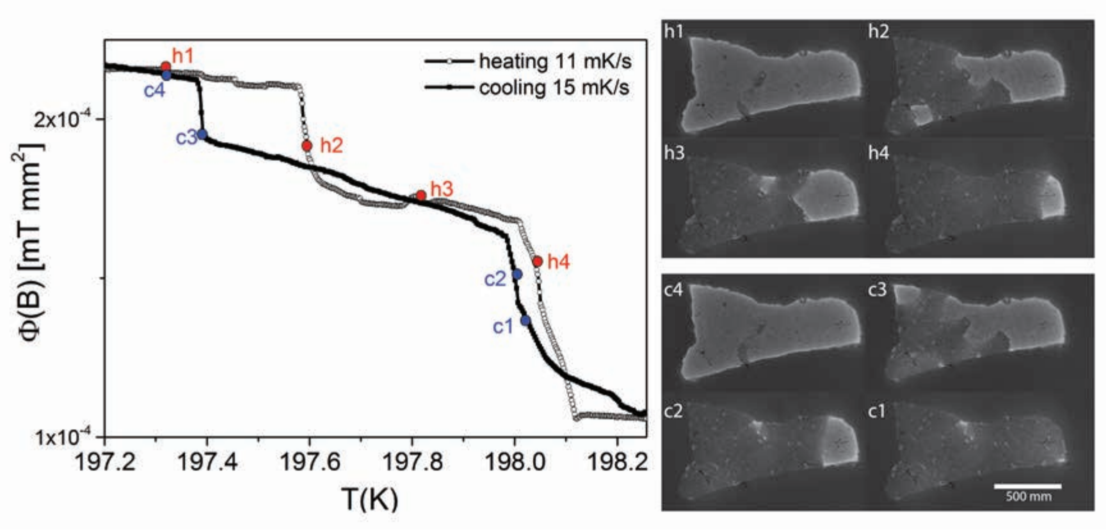

FIGURE 4.21: Left graph: magnetic flux integrated across the surface of the sample during heating (11 mK/s) and cooling (15 mK/s) transitions. The MOIF images on the right show the difference in the path followed by the surface ferromagnetic domains growth for the two temperature directions of the transition. In particular, h2 and c3 show that the energy barriers of bottom and top edges are very close to each other, thus the one which disappear first is determinates by a random disordered process. An external biasing field of 30 mT is pointing out of the surface [76].

reported on the right side of the figure and highlight two big steps which are related to two big parts of the sample transforming. Looking at the pictures, the right side of the sample transforms at a lower T, while the left part is characterized by a transition temperature almost 0.5 K higher. The thermal hysteresis represented in the graph has been obtained by correlating the measured data to the frame rate and by removing an arbitrary offset. This operation allowed to compare differences in the PM/FM and FM/PM fronts progress. The dissimilarities in the thermal hysteresis of the two sides of the sample could be due to slight differences in composition (i.e. Curie temperatures) as it was observed in [75], or to differences in the thermal contact between the sample surface and the cold finger. However, thanks to the possibility to correlate the images of the whole surface with the total change of the magnetic flux, it can be observed that the two sides of the sample are not completely separated in temperature and some grains on the left start to transform at the same time (temperature) of the big part on the right. This feature is highlighted in some representative frames on the right of Fig.4.21(h2 and c3) and it may refer to the first order intrinsic dynamics of the sample rather than to thermal contact effects. By performing (several) heating and cooling cycles (from un-calibrated sequences here not reported), it was also found that, both during heating and cooling, the nucleation of the new phase mainly starts from the edges of the sample and moves toward the centre. The big pinning events which stop the phase front are almost the same in heating and cooling and seem to be related to mechanical stresses or cracks produced by the sample lattice expansion: at the end of the experiment, the sample was in fact divided in many pieces. Due to the fact that the temperature at single local sites is not known, it is not possible to quantitatively estimate the effective local hysteresis and correlate it to the bulk one [43]. However, it is possible to qualitatively observe that, in spite of the slightly faster temperature sweep rate, the linear increase of the magnetic flux is slower during the cooling than during the heating process. On the other hand, in the heating process, a reentrance of the total magnetic flux is observed just after the strong de-pinning of the left grains. To explain the slower cooling transition, it was individuated, from MOIF frames, a particular behaviour of the FM front with respect to some $\alpha - Fe$ grains, around which the FM transformation seemed to be inhibited. An example is visible in 4.21 (frame h2), where an $\alpha - Fe$ grain lying in the middle of the sample is surrounded by the FM front. As pointed out in the previous section, when the transition is completed and the magnetic flux is constant, the $\alpha - Fe$ grains do disappear leaving, nevertheless, magnetic holes nearby. Revising the previous results, some of the magnetic holes, which were showed to posses a lower linear response with respect to the FM main phase (a values of Fig.4.20 at T = 185 K), can be regarded as regions of the main phase with slightly different compositions, with a lower Curie temperature and a lower total magnetic moment. In this experiment, the magneto static field of the slow magnetic phase front (FM) seems to interact with them and with the $\alpha - Fe$ grains; beside the random nucleation process, the FM front advance seems to experience some magnetic friction.

4.5 Defects, fast and slow dynamics

In this chapter, the MOIF technique was applied to the polycrystalline MCE compound La(Fe$_{0.9}$Co$_{0.015}$Si$_{0.085}$)$_{13}$ to visualise its magnetic phase transition. The magnetic properties of the main MCE phase and of minor phases have been characterized and compared, quantifying the local z-component of their stray fields by observing the phase transition with temperature. Two characteristic dynamics appeared: a faster one, which propagates with a velocity greater than 4x10^{-3} m/s, and a slower one (1x10^{-4} m/s). Different sources of hysteresis were evaluated as, for example, the presence of cracks across the volume. Such extrinsic factors introduce disorder in the compound, indicating that the size and the shape of the sample are crucial for dynamical observations (structural defects or micro-cracks can generate big jumps of the fast transition front motion). The low thermal hysteresis of this class of compounds [43] can be affected in different ways by the type of defects, either structural or magnetic, which alter the energy landscape of the PM/FM front. As an example, in section 4.4.5, the slow cooling process has been shown to be slowed down by the presence of magnetic impurities, which introduce random magnetic energy barriers and contribute to the hysteresis. The results obtained by the observation of the phase front spatial evolution along the PM/FM transitions, were compared to calorimetry measurements. The graph of Fig.4.22 reports two heat flux measurements, performed at a low rate of 0.01 K/min on a third sample of the

$LaFe_{11.7}Co_{0.195}Si_{1.105}$ compound, by using a differential scanning calorimeter in zero applied magnetic field.

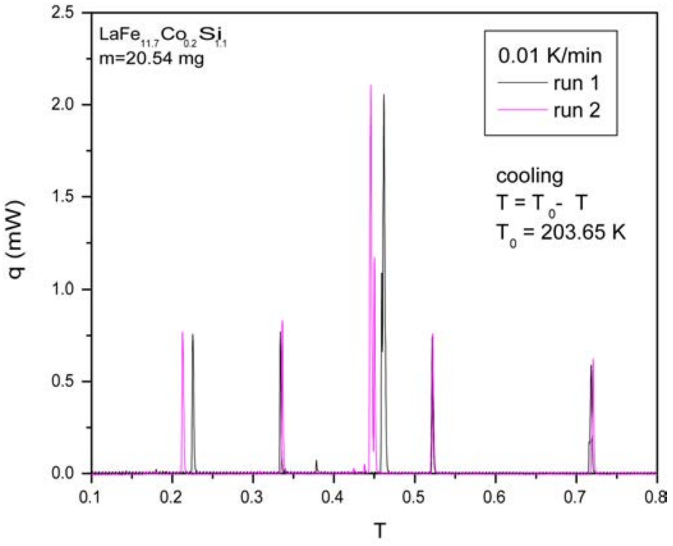

FIGURE 4.22: Two different scans of heat flux of a $LaFe_{11.7}Co_{0.195}Si_{1.105}$ fragment at temperature rates of 0.01 K/min (∼ 0.17 mK/s) around the transition temperature measured by commercial Perkin Elmer DSC in zero applied magnetic field [79].

The scans depicted in Fig.4.22 show many separated heat flux peaks repeating almost identically along temperature cycles. Although the discussion about calorimetry measurements is postponed to Ch.5, the connection between the front spatial evolution observed by the MOIF technique and the existence of a separation of volumes deducible by the DSC scans is here presented. Furthermore, the term avalanches referred to the heat flux peaks of calorimetry measurements are introduced and in [79] they were related to the fast reproducible propagation of the front in MOIF images. In fact, these observations were supported by the fact that, the avalanches appearing at constant temperature were fast and not resolved with such temperature rate, as it was found for the fast motion of the phase fronts. In chapter 5, the differential scanning calorimetry technique will be introduced and the measurements of heat flux avalanches will be discussed for a series of samples similar to the one investigated by MOIF.

5

Calorimetry study of the transition in LaFe$_x$Mn$_y$Si$_z$-H$_{1.65}$

The scope of this chapter is to provide an introduction to the differential scanning calorimetry methods (5.1) exploited in this thesis. Because of their unique properties like the large MCE values [17] [18] [19], the tunable Tc [80] [81] and, more importantly, the small thermal and magnetic hysteresis [43], a series of La(Fe$_x$Mn$_y$Si$_z$)$_{13}$-H$_{1.65}$ compounds, has been the main object of investigation. The measurements were performed with a differential scanning calorimeter with Peltier cells, build at INRiM [82] and described in 5.2. The MCE properties of the series are reported in section 5.3. In section 5.4, a low rate calorimetry method is applied to these samples in order to characterize the passage from a first to a second order transition with the purpose of understanding the origin of the hysteresis. The measurements of the exchanged heat flux, obtained with the calorimetry experiments, are collected while varying the composition, the external magnetic field and the mass under investigation.

At the end of the chapter it will be shown that the PM/FM (and vice-versa) phase transformation in the series is accompanied by hysteresis and by heat flux avalanches when the transition is of the first order. The evolution of the avalanche signals with the magnetic field and the composition gives a possible explanation to the fast dynamics observed in the MOIF experiments of Ch.4 [79] [76] .

5.1 Differential scanning calorimetry

Calorimeters are used in many research fields (chemistry, cell biology, material science, ...) to measure the thermodynamic properties of molecules and materials. Among all the existing types of calorimeters, the ones based on differential scanning calorimetry (DSC) are the most popular (and commonly used). The DSC is a thermal analysis that can be used to determine the temperature and the heat flow associated with the material transitions as a function of time and temperature. During a temperature change, DSC measures a heat quantity, which is released or absorbed by the sample on the basis of a temperature difference between the sample itself and a reference material.

DSC techniques can be divided into two categories: the heat flux DSCs and the power compensated DSCs. Both the methods require two equal cells, one

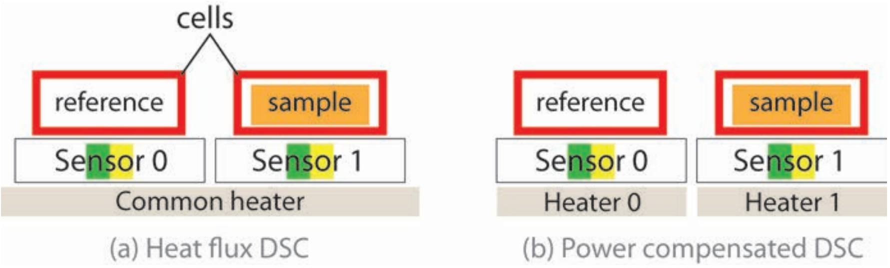

FIGURE 5.1: Scheme of the two methods for DSC analysis. (a) The Heat flux method uses the measure of the ΔT between the sample and the reference to calculate the heat flux furnished to the sample. (b) The power compensated method uses two different source of heat to maintain the sample and the reference at the same T.

used to hold the sample (sample cell) and one used as a reference (empty cell). The heat flux methods use a common heater for both the sample and the reference cell, while their temperatures are monitored by two separated sensors (Pt100, thermocouples, Peltier cells,...). After a correct calibration of the reference response, any difference of the two temperatures, ΔT, can be related to the heat flux exchanged by the sample and to its thermal properties. The other class of DSC methods are based on temperature measurements of the sample and the reference. In the presence of a ΔT, additional heat can be provided to compensate this difference by using two separated heaters for the sample and the reference cells. The extra heat furnished to the sample represents then the heat flux it exchanges with the surroundings. A scheme which highlights the principal differences in the two DSC configurations is depicted in Fig. 5.1. Both techniques require a well defined thermal system and the definition of its surroundings. The sample and the reference cells are usually embedded in an adiabatic holder in order to maximize the heat exchange between the heaters and the cells themselves and minimize the losses with the surrounding environment. Under such conditions, during the experiments, it is possible to determine some fundamentals thermodynamics properties of the samples: the internal energy, the specific heat and, if a phase change is observed, the total heat transferred during such transition.

The choice of calorimetry is then appropriate for the study of phase transitions; in particular, for what concerns the magnetocaloric effect, DSC experiments permit to fully characterize the quantities of interest for applications in MCE as it was explained in Ch. 3.

5.2 Peltier DSC setup

The experimental setup here described is based on the direct measurements of the sample heat flux. The system is a home made heat flux DSC [82] which makes use of two miniaturized Peltier cells as heat flux sensors. The two cells are positioned inside a brass cylinder which serves as a thermal reservoir. The external heat flux, used to change the temperature of the thermal bath, T_b, is provided by two power Peltier cells. This block is surrounded by a water circulating circuit to avoid over heating of the components due to the power Peltier cells. The temperature of the thermal bath is monitored by a resistance thermometer (Pt 100) positioned between the two Peltier flux sensors, which are connected differentially in order to subtract the common heat flux baseline. The sample can be easily positioned on the top of the cell of measure.

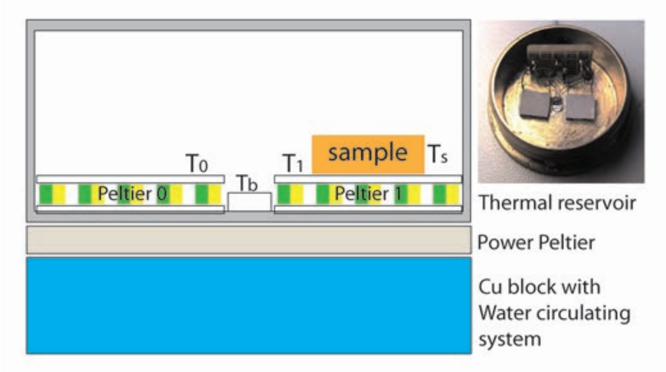

FIGURE 5.2: Scheme of the main components of the Peltier DSC at INRiM. In the photography is reported the brass cylinder (thermal reservoir) with the miniaturized Peltier cells connected differentially.

A vacuum chamber hosts the calorimetric cell. Such chamber can be evacuated or filled with inert gas like argon, in order to avoid the presence of spurious signals at about 273 K due to the humidity freezing and to improve the insulation from the external environment. The temperature can be regulated in a range of about ± 50 °C around the temperature of the copper passive block, which is kept constant by an external chiller. The operational range results to be from -50 °C to +100 °C. As it is depicted in the scheme of Fig.5.3, the vacuum chamber containing the calorimeter cell can be exposed to magnetic fields by means of an electromagnet producing an external magnetic field parallel to the top plate of the miniaturized Peltier cells which can be controlled in a range up to ± 2 T.

5.2.1 Heat flux equation

The heat absorbed/released by the sample can be obtained by solving a thermal equivalent circuit for the heat flux, $q = \frac{dQ}{dt}$ [W], which flows trough the components of the calorimeter [82]. Thanks to the analogy between the thermal domain (Fourier's law) and the electrical domain (Ohm's law), each thermal element of our setup can be represented by a thermal resistance and a thermal capacitance. For a bad heat conductor, the heat flux q will experience a large thermal resistance, otherwise the material will be described just by its thermal capacitance. Finally, the electrical potential difference is represented, in thermal circuits, by temperature difference, ΔT.

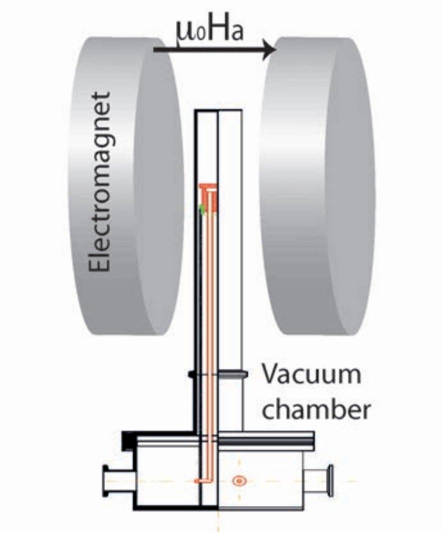

FIGURE 5.3: The calorimetric cell and the power Peltier cells (not shown) are attached to the top of the inner cylinder, which ends with a copper block (red) whose temperature is kept constant by a circulating fluid. At the bottom, the larger part of the chamber contains the electrical feed-through and gas/vacuum flanges. An electromagnet is used to generate static magnetic field in the plane of the calorimeter cells.

It follows that each part of the calorimeter, either the reference cell and the sample cell, can be described by their equivalent thermal circuits, as depicted in Fig.5.4. In such picture, T_b, T_0 and T_1 represent the temperatures of the thermal bath, of the reference cell top plate and of the one of the sample respectively, while T_s is the sample temperature, which depends on the proprieties of the sample itself and on its thermal contact with the Peltier cell. In the scheme (b) the sample is described by its thermal capacity, C_s, which is directly related to the intrinsic specific heat, while the realised contact is represented by a resistance R_c. The two miniaturized Peltier cells of the reference and of the sample

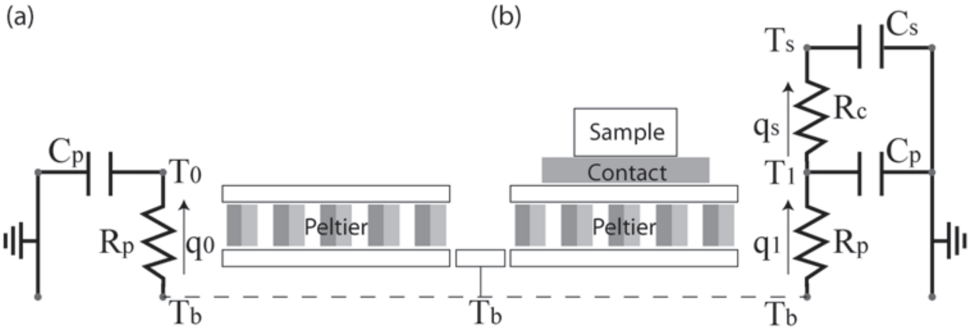

FIGURE 5.4: Equivalent thermal circuits for the Peltier cell of the reference (a) and of the Peltier cell of measure (b).

circuits are depicted in the same way with a capacitance C_p and a resistance

R_p, which connects the top plates with the thermal bath. Such resistance arises from the thermal conductivity of the thermoelectric pillars:

$$R_p = \frac{d_p}{2NA_pk_p} \tag{5.1}$$

where N is the number of couples, d_p the height of the pillars, A_p and k_p their cross section and thermal conductivity, respectively. Typical values of R_p are in the range of 10 KW^{-1} and 100 KW^{-1}.

When the temperature of the thermal bath is changed at a constant rate, $\frac{dT_b}{dt}$, the equations for the two temperatures at the top plates of the miniaturized Peltier cells are respectively for the reference and for the sample:

$$T_0 = T_b - \tau_p(\frac{dT_b}{dt}). \tag{5.2}$$

and

$$T_1 = T_b - \tau_p(\frac{dT_b}{dt}) - R_pq_s. \tag{5.3}$$

The Peltier cells, from the theory of thermoelectric effects [14], generate a voltage proportional to the temperature difference between their junctions $v_1 = \epsilon(T_1 - T_b)$ and $v_0 = \epsilon(T_0 - T_b)$ where ϵ is the Seebeck coefficient of the cells. Therefore, if the Peltier cells sensors are connected differentially, the resulting voltage become $v_p = v_1 - v_0$, is then proportional to the temperature difference of the two cells:

$$v_p = \epsilon(T_1 - T_0) \tag{5.4}$$

The final equation for the transferred heat flux of the sample becomes:

$$q_s = -\frac{1}{S_p}\left(v_p + \tau_p\frac{dv_p}{dt}\right) - q_A \tag{5.5}$$

where q_A represents a baseline background. The time constant τ_p depends on the Peltier cell thermal capacitance C_p, which mainly arises from the top plate of the cell (generally made of allumina or silicon). The sensitivity of the calorimeter, S_p, together with τ_p and q_A have to be calibrated before the measurements.

The temperature rate can be controlled within ± 0.005 K and the heat flux noise floor of the setup is around 0.2 μW. The sampling time of the measured signals could be set by the VEE software employed to control the instruments. The described setup was optimized for a sample contact surface equal to the one of the Peltier top plate (5X5 mm^2) and for sample masses larger than 50 mg [82]. In the next section, the employment of the current setup for the characterization of MCE properties of compounds will be analysed.

5.2.2 Detection of phase transitions by DSC

In order to describe a phase transition, the measurements of the heat flow toward/from the sample as a function of the temperature (time), q_s vs T (t), can be exploited. In the absence of any physical transformation of the sample, the heat flow provided by the sample characterizes is specific heat and entropy at the equilibrium. Otherwise, if the sample undergoes a physical transformation, the different temperatures reached by the measurement and the reference cell will give rise to a peak in the measurements of the heat flow. An exothermic processes (such as crystallization) results in a negative peak of the heat flux profile, while in an endothermic process the peak will point toward positive values of the heat flux. From our setup, starting from the measure of q_s of Eq.(5.5) of a sample of mass m_s, some characteristic thermodynamics quantities can be calculated. In particular, it is possible to obtain the specific heat and the total entropy change by using equations:

$$c_p = \frac{1}{m_s}\frac{q_s}{\frac{dT_s}{dT}}, \tag{5.6}$$

and

$$s - s_0 = \frac{1}{m_s}\int_0^t \frac{q_s}{T_s}dt, \tag{5.7}$$

s_0 represents a reference value. The value of c_{PM} is usually staken at the temperature $T_+ = T_c + 20K$, well above the transition temperature, where c_p can be considered magnetic field independent.

In heat flux calorimetry the presence of the thermometer on the sample would introduce an uncontrolled thermal link, thus the temperature of the sample can be determined by an indirect method. By using the circuit of Fig.5.4 (b), T_s can be calculated as:

$$T_s = T_1 - R_c q_s. \tag{5.8}$$

The thermal contact resistance, R_c, slightly changes depending on how the sample is attached to the cell of measure, thus it has to be determined each time the configuration changes. In order to do that, the rate dependence of the curves $s(T_b, \frac{dT_b}{dt})$ can be exploited. The value of the contact resistance can be set as the one for which all these curves rescale onto the same one when they are plotted as a function of T_s of Eq.(5.12). The rescaling procedure is also used to determine the thermal hysteresis of a phase transition, since it is applied to the heating and cooling curve sequences separately. In the case that the obtained rescaled curve is the same both for the heating and the cooling no thermal hysteresis is inferred. Otherwise, the procedure provides a good estimate of the thermal hysteresis of the phase transition.

Within this method, the measured quantity q_s is intergrated over all the physical processes which contribute to the change in the system internal energy. This direct measurement of the heat flux is thus appropriate for the characterization of materials with magneto structural transitions of the first order, characterized by the interplay between magnetic, lattice and/or electronic terms (see Ch. 3), hysteresis effects and irreversibility. On the other hand, due to the possibility to change the external magnetic field, the measurements of c_p and $s - s_0$ can be representative of the MCE properties of a compound (see Ch. 3) when it undegoes a reversible phase transition. In fact, the quantity c_p of Eq.(5.6) refers to equilibrium conditions while, as it was explained in Ch.2, a first order transition deals with out equilibrium processes thus also a latent heat term has to be take in to account. In the next sections this fact will be commented together with the experiments.

5.3 MCE properties of the La(Fe,Mn,Si)$_{13}$-H

A series of samples of La($Fe_xMn_ySi_z$)$_{13}$-$H_{1.65}$, in the form of granules, was produced by Vacuumschmelze GmbH & Co. La(Fe-Mn-Si)13 alloys with variable Mn content were prepared by powder metallurgy technique and hydrogenated as described in [51]. Master alloys were prepared by vacuum induction melting followed by mechanical milling steps to produce fine powders. The composition of each alloy was adjusted by blending master alloys with elemental powders. Compaction of the powder blends was performed by cold isostatic pressing. The green bodies were vacuum sintered at around 1100°C followed by an annealing treatment at 1050°C [49]. Hydrogenation was performed on a granulate material with a particle size less than 1 mm [53]. These compounds can have a first or a second order phase transition depending on several factors and are produced for MCE applications near room temperature. In fact the transition from a low T ferromagnetic phase to an high T paramagnetic phase can be tuned nicely by varying the amount of Mn from y = 0.06 to 0.46 as it is reported in the table of Fig.5.5. The characterization of their MCE properties was performed by using a commercial Power compensated DSC (Perkin Elmer series) and the home made Peltier DSC explained above based on the heat flux method. An equal amount of granules (50 mg) was inserted in an allumina pan of diameter (mm) and closed with an allumina disk. An equal empty pan was positioned on the top of the reference Peltier cell.

VAC sample code	x (Fe)	y (Mn)	z (Si)	sample mass (mg)	nominal T_c (°C)
32	11.22	0.46	1.32	61.20	-4
33	11.33	0.37	1.30	51.10	10
34	11.41	0.30	1.29	51.80	20
35	11.47	0.25	1.28	50.29	30
36	11.55	0.22	1.23	50.42	42
37	11.60	0.18	1.22	50.36	49
38	11.66	0.14	1.20	50.33	56
39	11.76	0.06	1.18	50.45	70

FIGURE 5.5: Table of the amount of the composition elements across the series La($Fe_xMn_ySi_z$)$_{13}$-$H_{1.65}$ (x + y + z = 13). The sample masses refer to the measurements performed to characterize their MCE properties.

POWER COMPENSATED DSC

With this setup, a commercial power compensated differential calorimeter of Perkin Elmer, the measurements consisted in the acquisition of the heat flux

q_s as a function of T_b under three scanning rates (25, 50 and 100 mKs $^{-1}$). The method of rescaling explained in section 5.2.2 [82] was applied to each sample, and permitted to determine the relative thermal resistance R_{c-PE} [1] and the thermal hysteresis ΔT_{hys} (values are reported in table 5.1). The reference value of

Sample	ΔT_{hys} (K)	R_{c-PE} (K W^{-1})	c_{PM} (J kg^{-1}K^{-1})
32	0.0	150	450
33	0.2	125	450
34	0.4	160	460
35	0.5	120	460
36	0.7	130	470
37	0.9	100	480
38	1.2	115	490
39	1.5	100	500

TABLE 5.1: Values obtained in zero field by using DSC calorimeter based on power compensation (Perkin Elmer). c_{PM} is the baseline specific heat, defined as the value of c_{PM}=$c_p(T_+)$ at the temperature T_+ = T_c + 20 K.

c_{PM} is magnetic field independent and represents the specific heat of the paramagnetic phase at the equilibrium which can be obtained by measuring the c_{PM} baseline specific heat. The obtained c_{PM} were used as references for the series (Table 5.1).

PELTIER DSC

Within the Peltier DSC the measurements consist in the acquisition of the heat flux, q_s, as a function of thermal bath temperature, T_b, according to Eq.(5.5).

The characteristic quantity for the Peltier cells were measured once, for all different magnetic fields and samples, as the thermal configuration is always the same. In particular S_p and τ_p were determined with an empty allumina pan on the cell of measure. With this procedure the intrinsic time constant of the Peltier cells was found to be $\tau_p = R_pC_p$ = 3.7 s and the sensitivity:

$$S_p = 0.76 \cdot (1 + 4.1 \times 10^{-3}T - 1 \times 10^{-7}T^3). \tag{5.9}$$

For each composition the following graphs reports:

- Top left: the total specific heat, c_p measured at different fields following Eq.(5.6);
- Top right: the magnetic field induced entropy change -Δs(H,T)=-(s(H,T)-s(0,T)). Lines: computed from the c_p data. Points: direct isothermal measurements.
- Bottom left: the total entropy variation s(H,T)-s$_0$ with respect a reference value s_0.

---

[1] I used the label PE which stands for Pelkin Elmer in order to differentiate this value from the thermal contact resistance which will be used in the Peltier DSC

- Bottom right: the ferromagnetic contribution to the entropy calculated as s(H,T)- s$_P$$M$($T$) where the value s_0 is set in order to have s(H,T)-s$_P$$M$($T$) = 0 at T =$T+$ and c_{PM}, is the baseline specific heat in the paramagnetic state.

On the right side of each graph the legend shows the applied magnetic field $\mu_0 H$ in Tesla (00 = 0.0 T, 05 = 0.5 T, 10 = 1.0 T and 15 = 1.5 T), where **h** stands for the heating process and **c** for the cooling process.

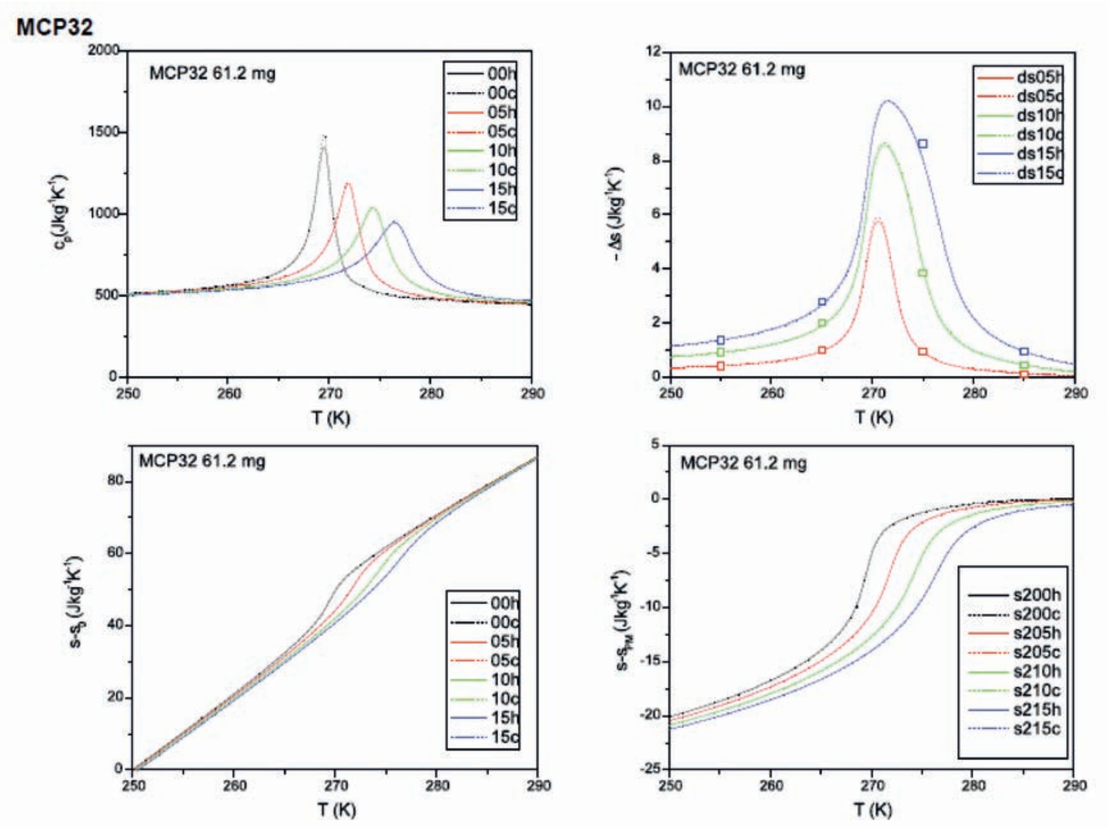

MCP33

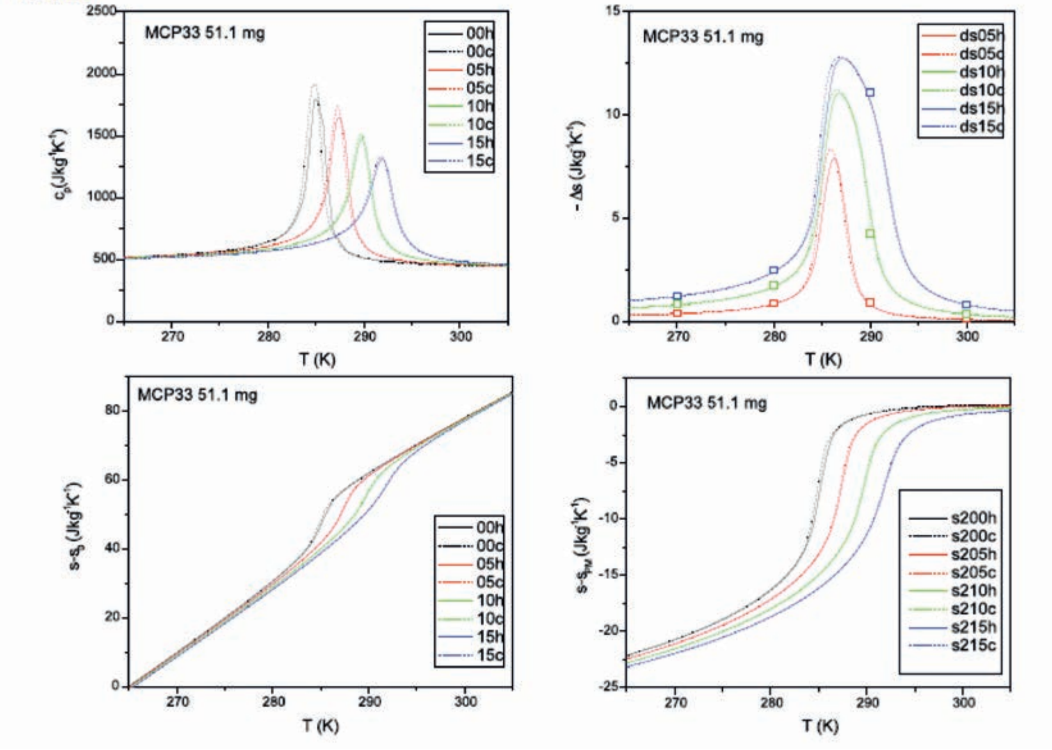
MCP33 51.1 mg
c_p (Jkg^{-1}K^{-1})
T (K)
00h
00c
05h
05c
10h
10c
15h
15c
- Δs (Jkg^{-1}K^{-1})
ds05h
ds05c
ds10h
ds10c
ds15h
ds15c
s-s$_0$ (Jkg^{-1}K^{-1})
s-s$_{PM}$ (Jkg^{-1}K^{-1})
s200h
s200c
s205h
s205c
s210h
s210c
s215h
s215c
270
280
290
300

MCP34

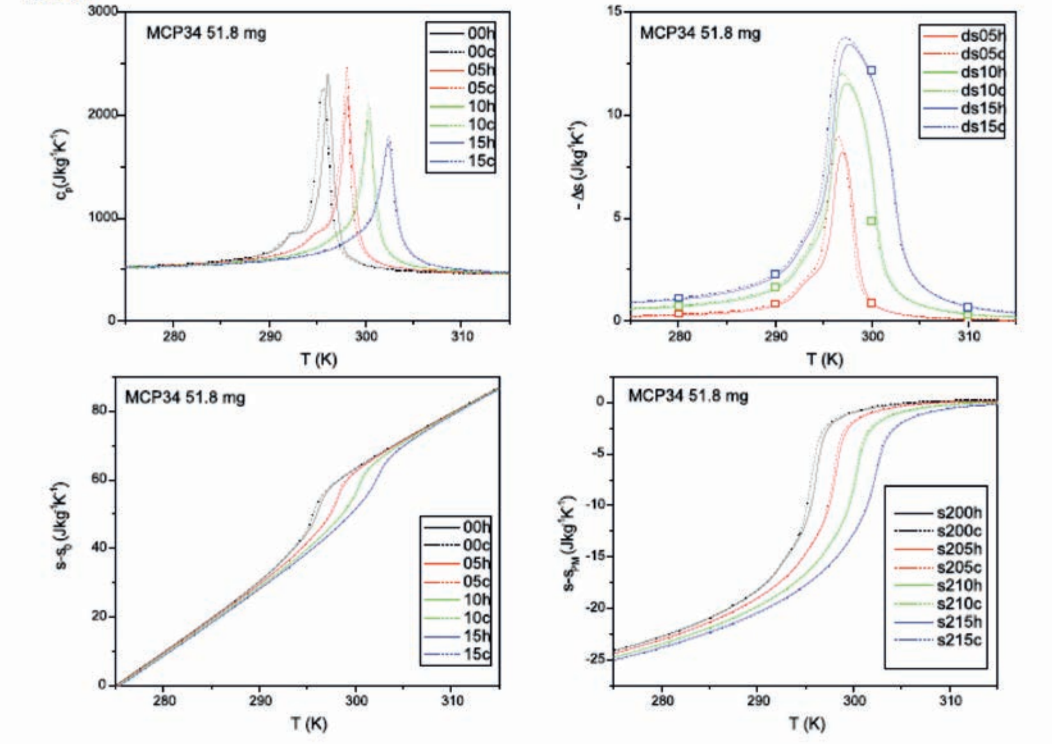
MCP34 51.8 mg
c_p (Jkg^{-1}K^{-1})
T (K)
00h
00c
05h
05c
10h
10c
15h
15c
- Δs (Jkg^{-1}K^{-1})
ds05h
ds05c
ds10h
ds10c
ds15h
ds15c
s-s$_0$ (Jkg^{-1}K^{-1})
s-s$_{PM}$ (Jkg^{-1}K^{-1})
s200h
s200c
s205h
s205c
s210h
s210c
s215h
s215c
280
290
300
310

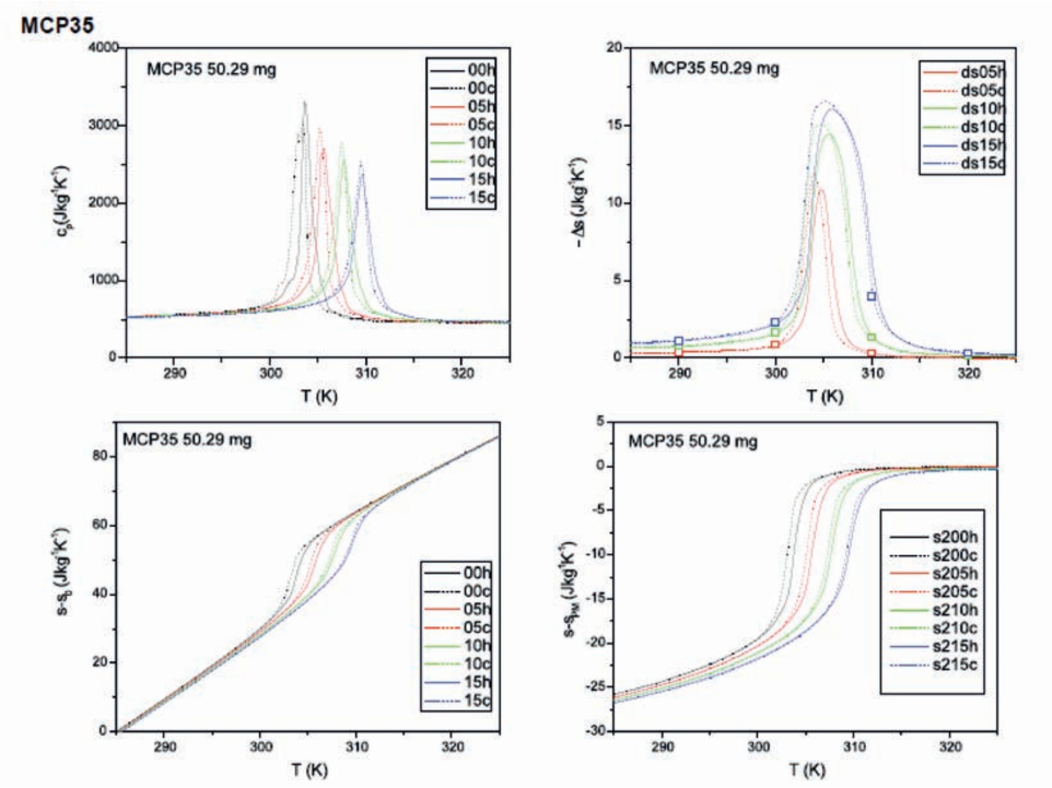
MCP35
MCP35 50.29 mg
c_p (Jkg^{-1}K^{-1})
0
1000
2000
3000
4000
290
300
310
320
T (K)
00h
00c
05h
05c
10h
10c
15h
15c
$-\Delta s$ (Jkg^{-1}K^{-1})
0
5
10
15
20
ds05h
ds05c
ds10h
ds10c
ds15h
ds15c
$s-s_0$ (Jkg^{-1}K^{-1})
0
20
40
60
80
$s-s_{PM}$ (Jkg^{-1}K^{-1})
5
0
-5
-10
-15
-20
-25
-30
s200h
s200c
s205h
s205c
s210h
s210c
s215h
s215c

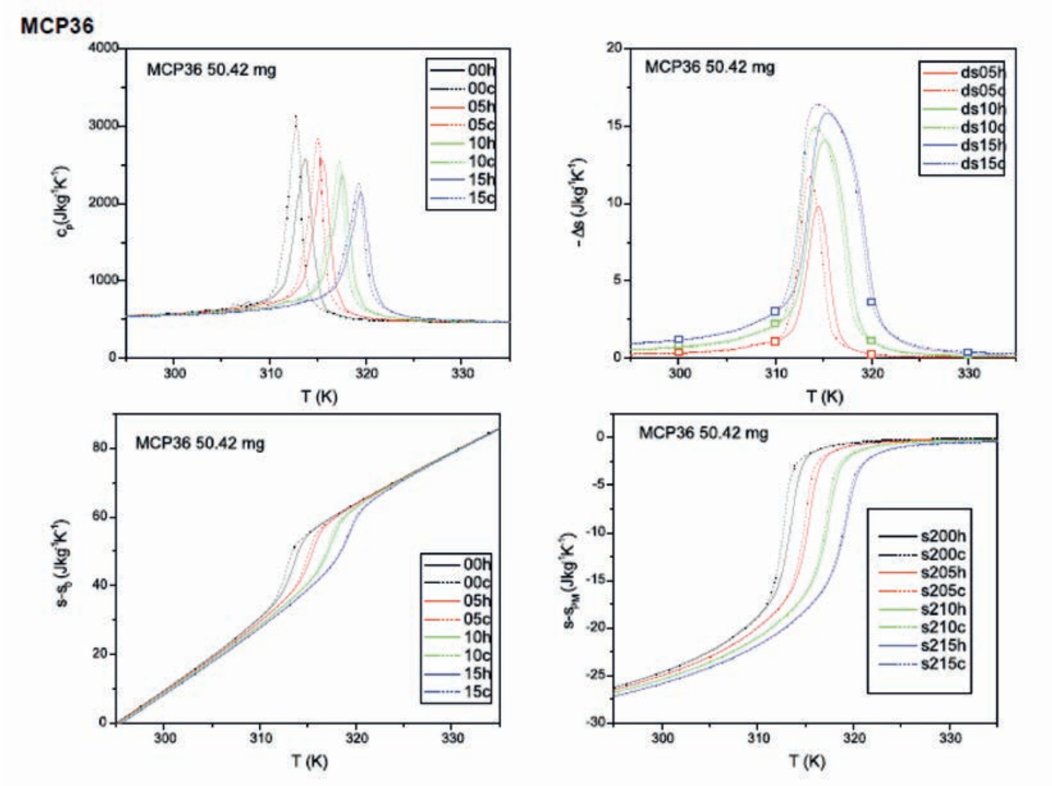
MCP36
MCP36 50.42 mg
c_p (Jkg^{-1}K^{-1})
0
1000
2000
3000
4000
300
310
320
330
T (K)
00h
00c
05h
05c
10h
10c
15h
15c
$-\Delta s$ (Jkg^{-1}K^{-1})
0
5
10
15
20
ds05h
ds05c
ds10h
ds10c
ds15h
ds15c
$s-s_0$ (Jkg^{-1}K^{-1})
0
20
40
60
80
$s-s_{PM}$ (Jkg^{-1}K^{-1})
0
-5
-10
-15
-20
-25
-30
s200h
s200c
s205h
s205c
s210h
s210c
s215h
s215c

MCP37

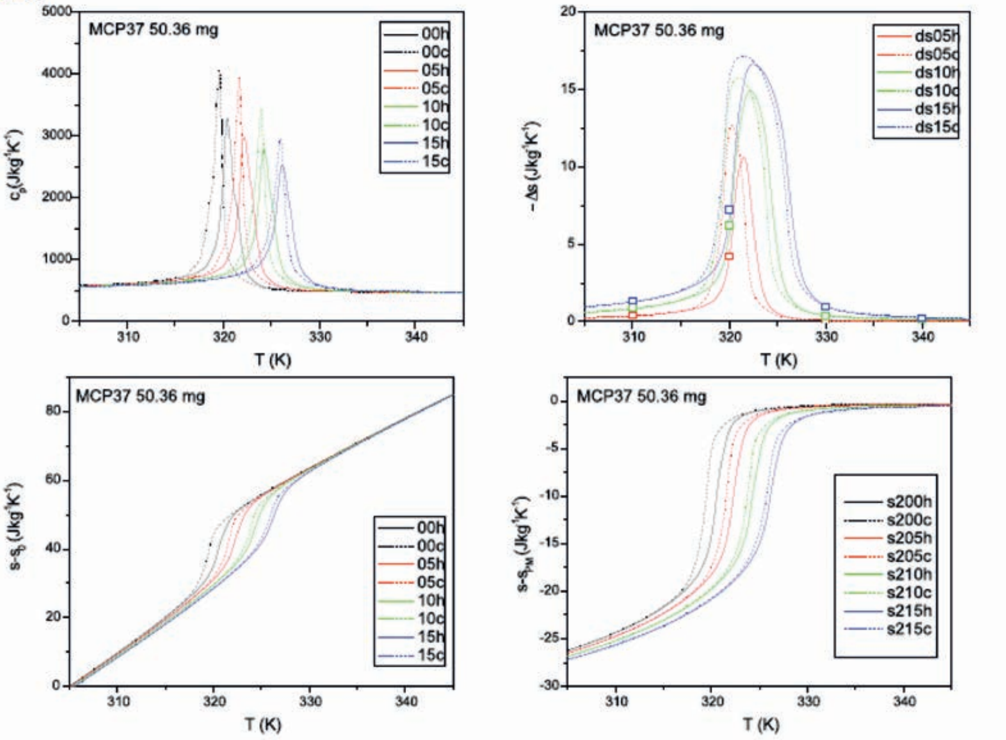
MCP37 50.36 mg
c_p (Jkg^{-1}K^{-1})
0
1000
2000
3000
4000
5000
310
320
330
340
T (K)
00h
00c
05h
05c
10h
10c
15h
15c
$-\Delta s$ (Jkg^{-1}K^{-1})
0
5
10
15
20
ds05h
ds05c
ds10h
ds10c
ds15h
ds15c
$s-s_0$ (Jkg^{-1}K^{-1})
0
20
40
60
80
$s-s_{PM}$ (Jkg^{-1}K^{-1})
0
-5
-10
-15
-20
-25
-30
s200h
s200c
s205h
s205c
s210h
s210c
s215h
s215c

MCP38

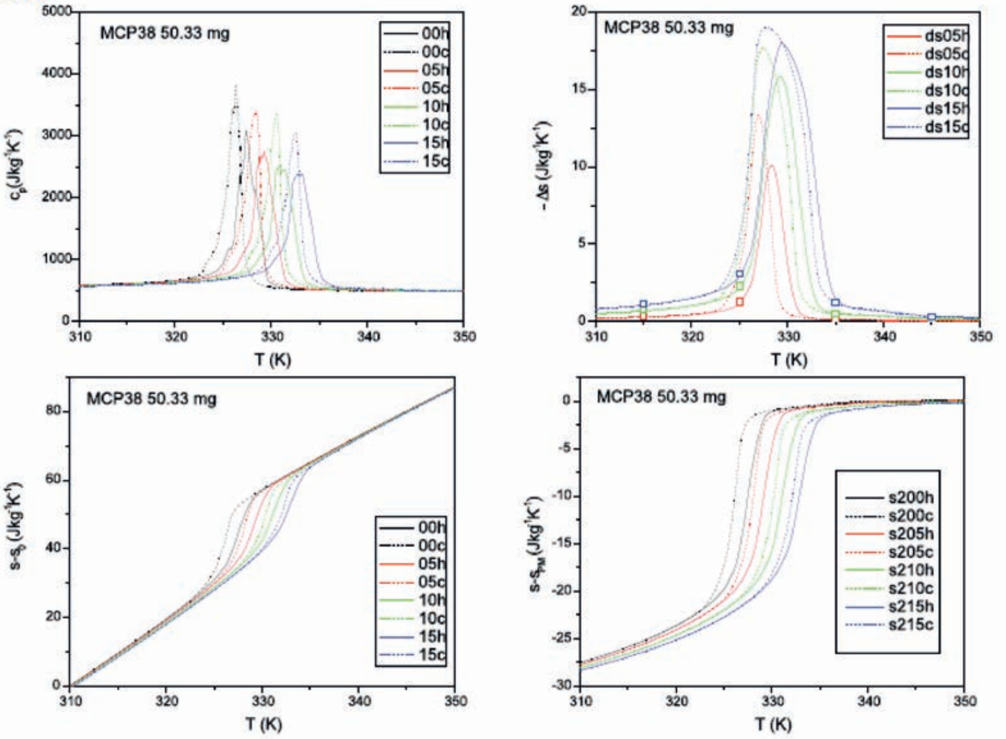
MCP38 50.33 mg
c_p (Jkg^{-1}K^{-1})
0
1000
2000
3000
4000
5000
310
320
330
340
350
T (K)
00h
00c
05h
05c
10h
10c
15h
15c
$-\Delta s$ (Jkg^{-1}K^{-1})
0
5
10
15
20
ds05h
ds05c
ds10h
ds10c
ds15h
ds15c
$s-s_0$ (Jkg^{-1}K^{-1})
0
20
40
60
80
$s-s_{PM}$ (Jkg^{-1}K^{-1})
0
-5
-10
-15
-20
-25
-30
s200h
s200c
s205h
s205c
s210h
s210c
s215h
s215c

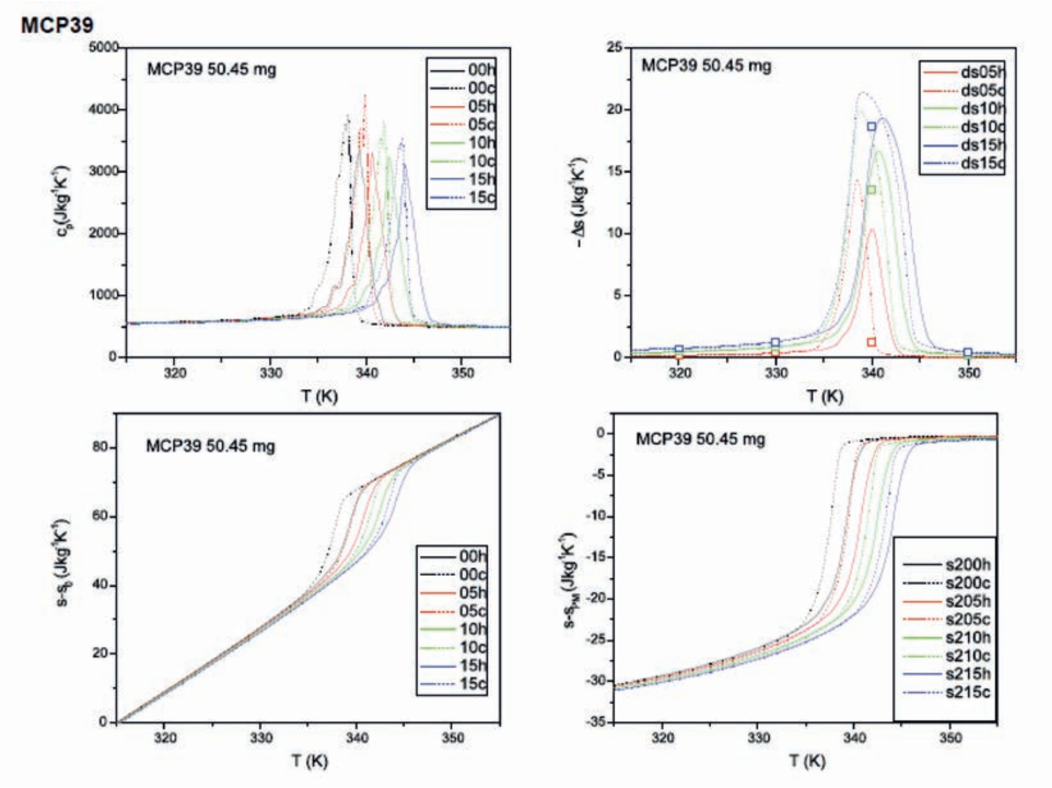

The full set of data permitted to extract some of the relevant parameters characterizing the series of compounds as a function of the Mn content; the obtained values are reported in table 5.2 and are:

- T_h is the transition temperature on heating;
- ΔT_{hys} = T_h - T_c, is the thermal hysteresis, where T_c is the transition temperature on cooling. The transition temperatures are taken at H = 0 as the temperatures values at which $s_{FM}(H,T)$ is equal to $\Delta s_0/2$;
- $(1/\mu_0)$ dT/dH is the shift of the transition temperatures with the field and it was computed on heating from the differences in T_c at H = 0 and $\mu_0 H$ = 1 T;
- Δs_{max} (1 T), the maximum of the magnetic field induced entropy change $\Delta s(T) = s(H,T) - s(0,T)$. The value reported is for $\mu_0 H$ = 1 T;
- Δs_0, the approximate entropy change associated with the transition at H = 0. From the measured entropy $s(H,T)$, the ferromagnetic contribution is calculated as $s(H,T) - s_{PM(}T)$ where

$$s_{PM} = s_0 + c_{PM} ln(\frac{T_s}{T_+}). \tag{5.10}$$

The value s_0 is set in order to have $s(H,T) - s_{PM}(T)$ = 0 at T =T_+. We approximate the entropy $s(H,T) - s_{PM}(T)$ before the transition as $-\Delta s_0 +$

$(c_f - d_f T_h)\cdot\ln(T/T_h) + d_f(T - T_h)$, with c_f = 170 Jkg^{-1}K^{-1} and d_f= 4.5 Jkg^{-1}K^{-2}. Δs_0 is taken on the curve at H = 0.

- $R_p + R_c$ is the sum of the values of the thermal resistances for the Peltier cell of measure and the contact realized between the cell and the sample.

Sample	y(Mn)	ΔT_{hys} (K)	T_h (K)	$\frac{dT}{dH}$ (K/T)	Δs_{max} (J kg^{-1}K^{-1})	Δs_0 (J kg^{-1}K^{-1})	$R_p + R_c$ (K W^{-1})
32	0.46	0.0	269.7	4.9	8.6	12	75
33	0.37	0.2	285.4	4.6	11.0	14.5	75
34	0.30	0.4	296.6	4.2	11.5	16.0	135
35	0.25	0.5	303.9	3.9	14.5	18.0	125
36	0.22	0.7	313.5	3.9	14.0	18.5	85
37	0.18	0.9	320.6	3.7	15.0	19.0	85
38	0.14	1.2	327.5	3.6	16.0	20.5	85
39	0.06	1.5	339.0	3.3	17.0	21.5	95

TABLE 5.2: MCE values obtained by using the DSC Peltier calorimeter in applied magnetic fields [Basso2015]. The peak of Δs_{iso} and ΔT_{ad} were calculated for a field change of 1.5 T.

From the values reported in Table 5.2, the introduction of Mn is found to decrease the transition temperature (from a reference value of 350 K of the Mn = 0.06) at a linear rate of 175 K/y$_{Mn}$. Mn substitution is also found to decrease the hysteresis at a rate of 4.6 y$_{Mn}$, which means that the transition is transformed from first to second order. The available isothermal entropy change and adiabatic temperature change were computed for all the samples by considering the heating curve in zero magnetic field and the cooling curve in magnetic field

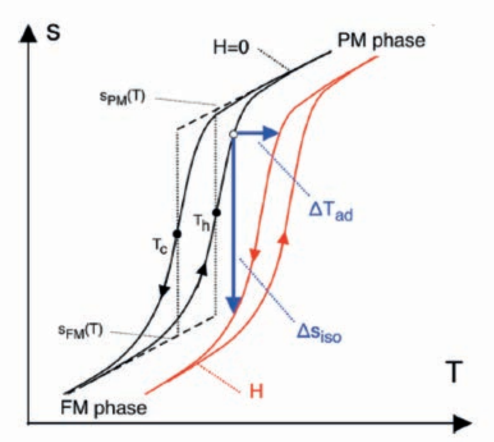

FIGURE 5.14: Sketch of the entropy versus temperature for the case of an equation of state with hysteresis. The isothermal entropy change Δs_{iso} and the adiabatic temperature change ΔT_{ad} obtained in a cooling thermodynamic cycle are indicated. Dashed lines shows the fitting functions for the entropy in the PM and FM states s$_{PM}$(T) and s$_{FM}$(T).

(cyclic processes with hysteresis). The transition temperatures upon heating and cooling, T_h and T_c, were derived from the measured $s(H,T)$ curves. In presence of first order transitions with hysteresis, their values are defined as the midpoint between the PM phase and the FM phase upon heating and cooling, respectively Fig.5.14.

In order to effectively characterize the MCE properties of the series, the resulting graph for ΔS_{iso} and ΔT_{ad} are reported in Figs.5.15 (a) and (b).

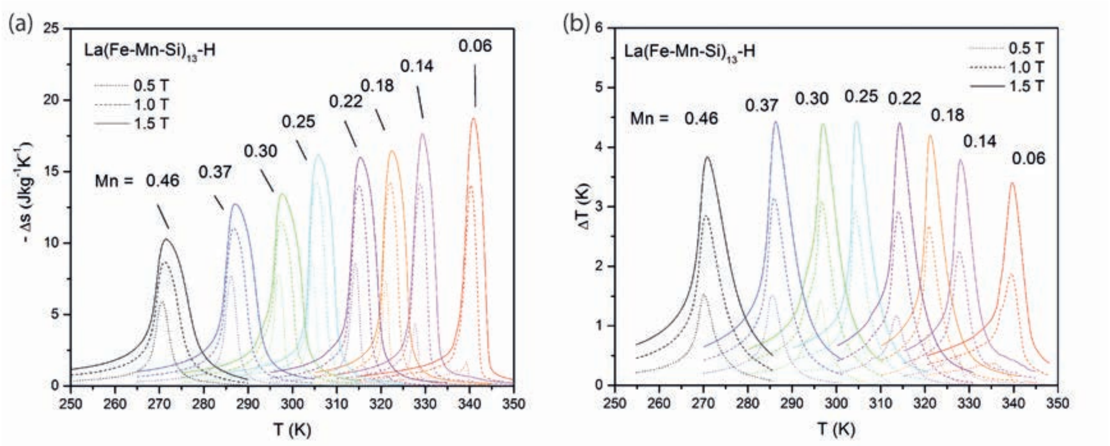

FIGURE 5.15: (a) Isothermal entropy change, (b) adiabatic temperature change of hydrogenated La(Fe-Mn-Si)13 with different Mn content.

The other relevant results, due to the effect of the Mn, can be see in Fig.5.16. The Mn content across the series produces a decrease of the height of the peak of the specific heat capacity and the disappearance of the difference between heating and cooling curves Fig.5.16 (a). At low Mn, the effect of the magnetic field is mainly to shift the peak of c_p to the right, while, at high Mn, the magnetic field also reduces the amplitude of the peaks. This observation suggests that the transition is close to a second order critical point. Information on how close the system is to the critical point can be gained by looking at the transition temperatures as a function of the magnetic field. Fig. 5.16 (b) shows the magnetic phase diagram built by taking the transition temperatures upon heating and cooling.

The graph also shows the lines corresponding to the linear fit of the heating and cooling points. The region enclosed between the two lines represents the metastability region in which both ferromagnetic and paramagnetic phase coexist. The critical point is at the intersection of the two lines. The critical magnetic field and temperature (H$_{crit}$, T$_{crit}$) are reduced as far as the Mn content is increased and it is observed that the transition is purely of the second order around the composition y(Mn) = 0.46. These observations show that Mn plays a dual role: decreasing the strength of the FM coupling and decreasing the magnetoelastic coupling. The identification of the exact position of the critical points in the phase diagram deserves a detailed experimental investigation by special methods which will be given in the next section.

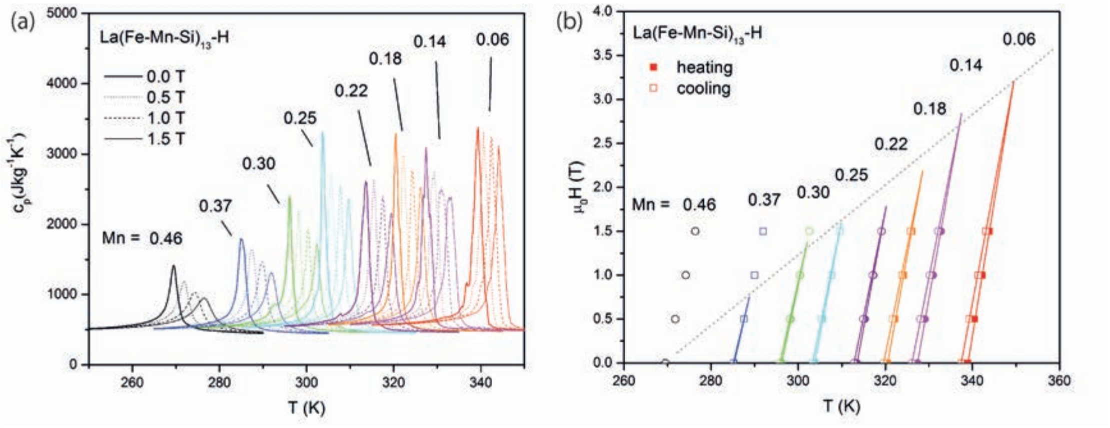

FIGURE 5.16: (a) Specific heat capacity and (b) (H, T) magnetic phase diagram of hydrogenated La(Fe-Mn-Si)13 with different Mn content.

5.4 Avalanches of heat flux in La(Fe,Mn,Si)$_{13}$-H

In Ch.4, a graph with two DSC measurements of the first order transition in the La($Fe_{0.9}Co_{0.015}Si_{0.085}$)$_{13}$ alloy was presented. Positive separated heat flux avalanches (peaks) were observed at the transition during heating, at low temperature scanning rates. The heat flux avalanches were qualitatively associated with the fast transformation of volumes observed by MOIF. In order to investigate the avalanches behaviour, the extensive dataset of the previous section is here used to evaluate the series of La(Fe-Mn-Si)-H alloys during the passage from first to second order transitions. By selecting samples, whose transitions in zero field have different thermal hysteresis, it is possible to explore different zones of the magnetic phase diagram of the compound. Heat flux measurements, at low temperature scanning rates, were performed by using both the power compensation method (Perkin Elmer calorimeter) and the Peltier differential scanning calorimeter, while sweeping the temperature across the Curie point of the compounds. The samples used for this study are single fragments with typical mass between 2 mg and 5 mg of three compositions, as it is reported in table 5.3. The choice of the three compositions has been thus based on the magnetic phase diagrams reported in Fig.5.16 (b) [27]:

x(Fe)	y(Mn)	z(Si)	m_s(mg) PE	m_s(mg) Peltier	T_c(^{o}C)
11.60	0.18	1.22	3.81	4.79	49
11.41	0.30	1.29	3.44	4.53	20
11.22	0.46	1.32	1.70	2.19	-4

TABLE 5.3: Compositions and masses of the three fragments of $LaFe_xMn_ySi_z$-$H_{1.65}$ investigated by low rate calorimetry.

- y = 0.46. The thermal hysteresis in zero applied magnetic field is null;

- y = 0.30. This composition possesses a low thermal hysteresis in zero applied magnetic field and its critical point is in the range 0-2 T;
- y = 0.18. The samples have a large thermal hysteresis in zero applied magnetic field and the critical point is above 2 T.

5.4.1 Effect of the thermal contact

A first set of samples was employed to study the effect of the thermal contact. These measurements were performed exploiting the power compensated method. The samples were positioned just in the middle of the allumina measurement pan and then covered with an allumina disk. In a second step, the samples were attached to the middle of the same pan by using Ag paste. For all the measurements, the temperature was increased across the Curie point using different scanning rates (1 K/min or 0.05 K/min). In Fig.5.17, the heat flux is reported as a function of time. The thermal resistance is defined as:

$$R_{th} = \frac{d_c}{k_{th} A_c}. \tag{5.11}$$

In our case, A_c is the contact area between the sample and the allumina pan and d_c is the thickness of the Ag paste layer. If single bulk fragments with irregular shape are used, it is not possible to quantitatively estimate the thermal contact resistance realised when using Ag paste. However, from the relation of Eq.(5.11), it is important to notice that, by substituting k_{th} of the air (k_{th}^{Air} = 0.0257 WK^{-1}m^{-1} at T= 20 °C) with the one of the Ag paste (nominal values k_{th}^{Ag} = 5-25 WK^{-1}m^{-1}), the thermal contact resistance can be improved. As it is

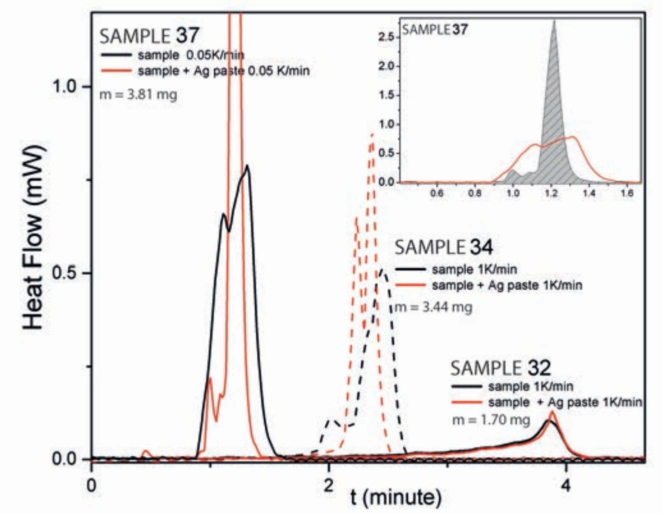

FIGURE 5.17: Effect of the thermal contact on the heat flux for three compositions (37, 34, 32) with different amount of Mn (y = 0.18, 0.30 and 0.46). The Ag paste improves the thermal contact (red curves).

shown in Fig.5.17, using the Ag paste, the endothermic FM to PM transformation of all the three compositions has a more detailed peaks structure. A weaker dependence from the thermal contact was observed in the y (Mn = 0.46) composition which, differently from the other compositions, could not be measured at rate lower than 1 K/min. This fact was attributed to the smaller mass of the sample (1.70 mg).

5.4.2 Low rate calorimetry and avalanches

The new set of fragments for the in field DSC measurements in the Peltier calorimeter is reported in table 5.3. By combining Eqs. (5.3) and (5.8) from the thermal equivalent circuit of Fig.5.4, the temperature difference between the sample and the thermal bath, during a temperature scan experiment, is given by:

$$T_s - T_b = -\tau_p(\frac{dT_b}{dt}) - R_p q_s - R_c q_s. \tag{5.12}$$

Since the value of the contact thermal resistance, R_c, can be reduced by improving the thermal contact as explained above, the samples were glued with silver paint to the measuring Peltier cell. Furthermore, in order to reduce the lag between the temperatures of the sample and the thermal bath, it is also possible to explore the effect of the scanning rate of the experiments, $\frac{dT_b}{dt}$. By using a sufficiently low rate we may expect to improve the resolution of the heat flux peaks.

In Fig.5.18 it is shown the comparison of different velocities, during heating (FM to PM phase transition), for the three sampless under investigation. In spite of the small masses and the low applied scanning rate (1 mK/s) of our experiments, the S/N (signal-to-noise ratio) was high enough to allow accurate measurements for all the selected samples. From these scans the total specific heat, c_p, was calculated by using Eq.(5.6) over the whole temperature range of the measurements. The quantity $\frac{dT_s}{dt}$ was assumed to be the same as the one relative to the thermal bath temperature controlled by the VEE program. As it is possible to see in Fig.5.18, by applying different rates, strong differences in the calculated c_p for the three samples appeared. The zero field phase transition of the sample with the lower Mn content (Mn(y) = 0.18 - Fig.5.18 (a)) is dominated by a high single isothermal peak (a unique avalanche); the number of the avalanches increases in the Mn(y) = 0.30 sample (Fig.5.18 (b)), while their maxima drop of about one order of magnitude with respect the Mn(y) = 0.18 case. For these two compositions, the avalanches behaviour appears when approaching the 1 mK/s scans (black continuous line). In this cases the total q_s at the transition has a strong irreversible component and, as a result, the calculated c_p appears as being scan rate dependent. On the contrary in the high Mn content sample (Mn(y) = 0.46 - Fig.5.18 (c)) avalanches were not detected down to 1 mK/s. In this sample the total c_p of the transition does not include any irreversible component and does not depend on the scanning rate.

When the avalanches are present, (Fig.5.18 (a)(b)), they are separated in temperature and it is possible to identify the events which are related to avalanches

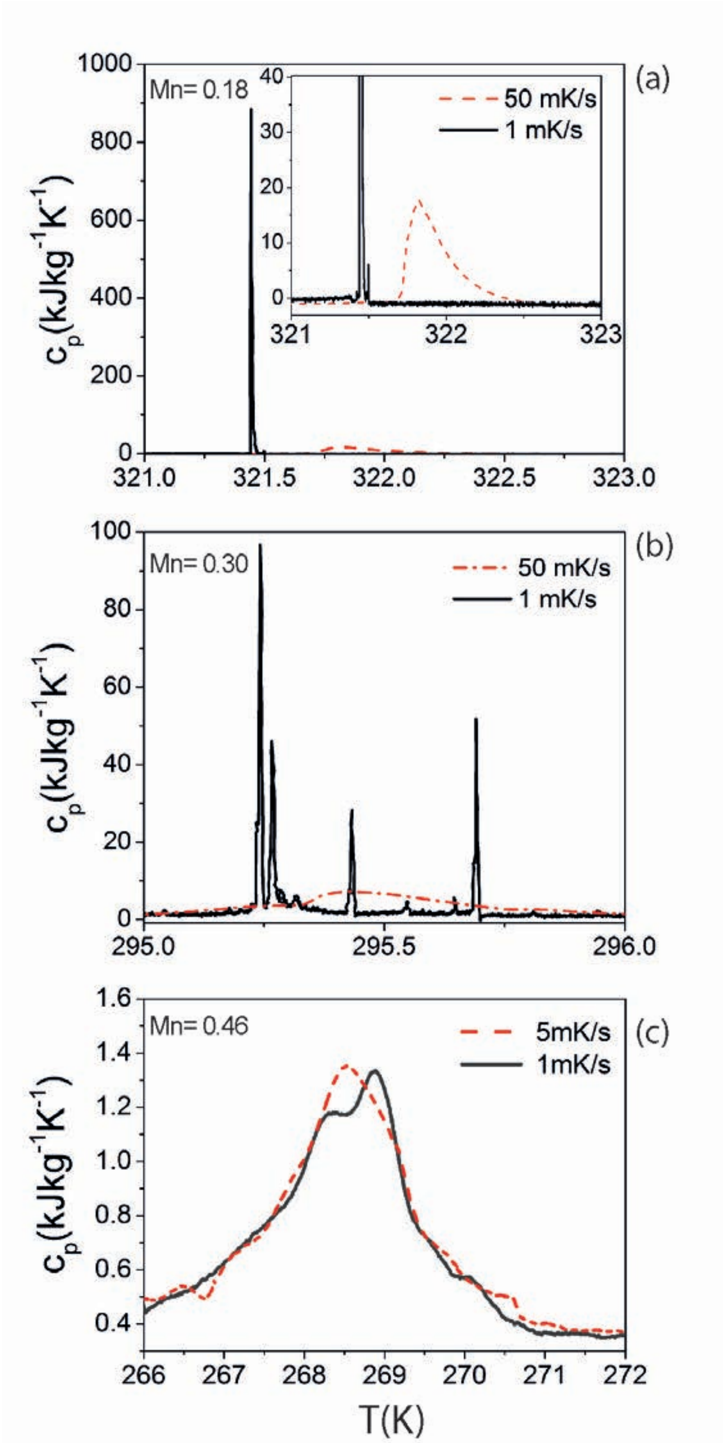

FIGURE 5.18: Specific heat at the transitions in zero magnetic field for the three composition of Mn (y = 0.18 (a), y = 0.30 (b) and y = 0.46 (c)) calculated from different temperature scanning rates from Eq.(5.6). The low rate set (black continuous lines) highlights the presence of heat flux avalanches in first order phase transitions (a)(b).

and the signal of a smooth background. It has to be considered that, at first order transitions, the total entropy variation is the sum of either a latent heat and a reversible contribution [83].

In our experiments, these two terms are well described by:

$$s - s_{PM} = \Delta s_{c_p} + \Delta s_L = \int_{T_i}^{T_f} \frac{c_p(T)}{T} dT + \sum_i \frac{m_i \Delta U_L}{T_i}. \tag{5.13}$$

Fig.5.19 reports a representative example of a heating transition in zero field when the two terms were considered. The first term in Eq.(5.13) has been calculated for a system in thermodynamic equilibrium and it counts for the specific heat (c_p) due to the background. The c_p term was extrapolated by a Gaussian fit (Fig.5.19 (b)) of the measured voltage difference, v_P (a), which was converted in q_s values following Eq.(5.5). The second term, on the right hand side of the equation has been calculated by integrating the single heat flux avalanches (after subtracting the c_p term) and represents the enthalpy of the latent heat peaks ΔU$_L$ = $\frac{q_i}{m_i}$. In the case of a multiple step transition, the index i refers to the sample fraction of mass m_i, which transforms at the temperature T_i and generates a single peak. If the transition is of the second order, no dissipative processes take place and the latter term is exactly zero, as it is observed for the y(Mn) = 0.46 composition. Fig.5.19 (d) shows the calculated entropy change from different temperature scan rates. In the graph it is presented the entropy calculated both from the total heat flux and from the sum of the different contributions of the specific heat and the latent heat. The specific heat of the paramagnetic phase is fixed at 460 Jkg^{-1}K^{-1} (5.1). The inset shows that the entropy generated by the avalanches is responsible for the isothermal steps of the total entropy change (blue curve) while, the one to the reversible processes is reflected in the specific heat (red curve). Analysing the avalanches behaviour, it is possible to observe that the number of avalanches decreases both adding or removing Mn atoms from the compounds. This fact is not expected to be caused by the presence of different defects densities since the three compositions have substantially similar micro structures. The increased quantity of Mn combined with the hydrogen should at least introduce higher amounts of impurities (i.e. α-Fe secondary phase) [53] [84], but the avalanches are visible only in the presence of lower Mn. The increasing number of peaks may have another physical explanation. Starting from a low temperature FM metastable state, the rising temperature favours the new PM metastable state. However, in the presence of a first order phase transition, the sample needs to overcome the energy barrier between the phases to effectively transform. A decrease of such barrier can be produced by defects, whose contributions overlap locally on the intrinsic double well energy landscape. In the low Mn composition of Fig.5.18 (a), the barrier is large and the sample transforms entirely due to a unique nucleation event, which is sufficient to remove a strong instability. As the Mn content increases, the barrier is lowered because the transition evolves toward the equilibrium and a gradual redistribution of the nucleation energies appears with respect the energy

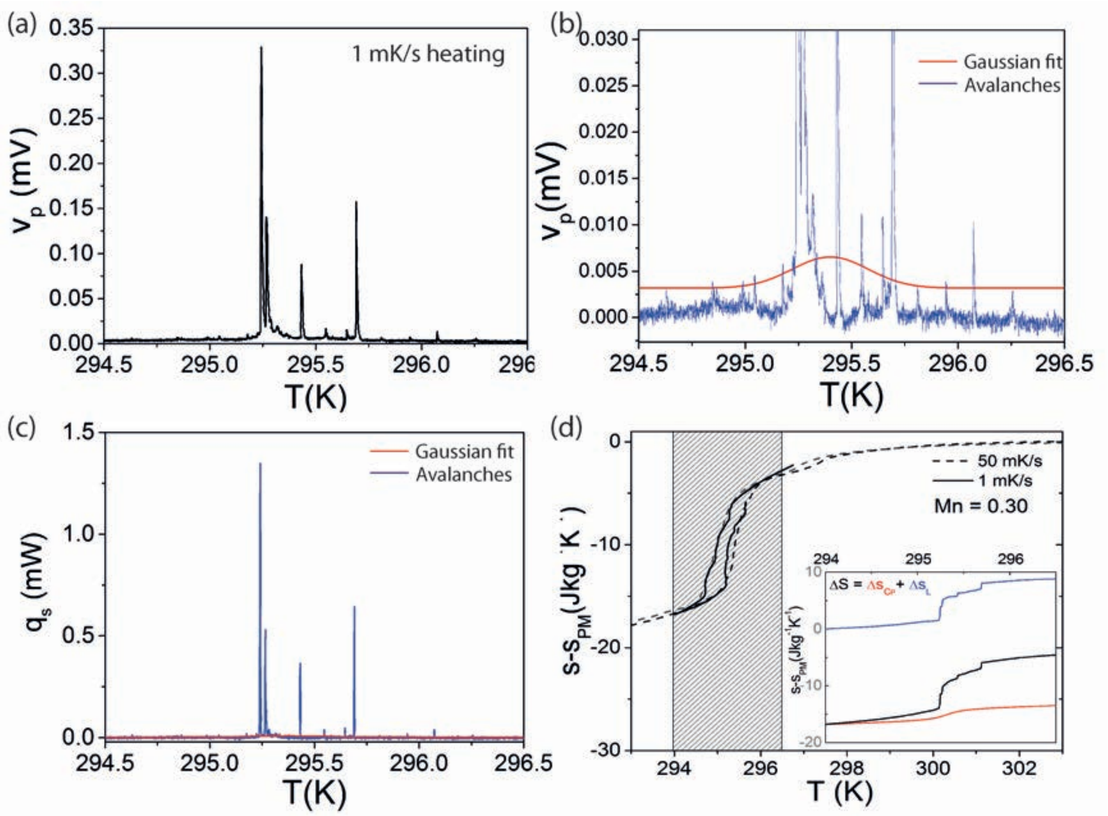

FIGURE 5.19: The voltage difference (a) has been divided in two terms with a Gaussian fit of the backgroun (b).The resultant q_s is calculated separately for the avalanches and the background (c). (d) Comparison of calculated entropy change, at H = 0, for the Mn(y) = 0.30 sample at two different rates 50 mK/s and 1 mK/s. Inset: example of the separated contributions of Eq.(5.6). for the corresponding shaded region of the main frame.

barrier between phases. A larger number of defects can then sufficiently reduce the effective energy barrier and make the transition to advance. As far, the transition become spatially separated [79] [76] and, from heat flux measurements, peaks at different temperatures and with different integral values are observed. Each heat flux avalanche well correlates with a different part of the transforming compounds, i.e. a single volume. The latent heat of the phase transformation vanishes when the energy barrier between phases approaches zero, y(Mn) = 0.46, meanwhile the energies over barriers produced by defects stop to be important for the whole process and the sample can transform continuously.

5.4.3 Avalanches in applied magnetic field

In the following, the heat flux avalanches are explored in the (H, T) magnetic phase diagram of the Mn(y) = 0.30 and Mn(y)=0.18 compositions. Their zero field transitions are of the first order and their critical fields are expected to be around 1.3 T and 2.4 T respectively (Fig.5.16).

Mn = 0.30: By increasing H, the separated avalanches of Fig.5.18(b) start to merge together, lower their heat flux values and some of them disappear. For $H > 1.1$ T all the peaks contributions are suppressed (left graph of Fig. 5.20). On the contrary, the continuous background grows and finally dominates the entire dynamics of the transition (red curve). As it was observed before for the role of the increasing content of Mn, the higher magnetic fields change the dynamics of the phase transformation, which passes from being dominated by a large number of latent heat events (activated volumes) to be fully reversible.

The results of the temperature dependence of the electrical resistivity, $\rho(T)$, of the composition Mn(y)= 0.30 are compared to the heat flux data and are plotted in the right graph of Fig. 5.20.

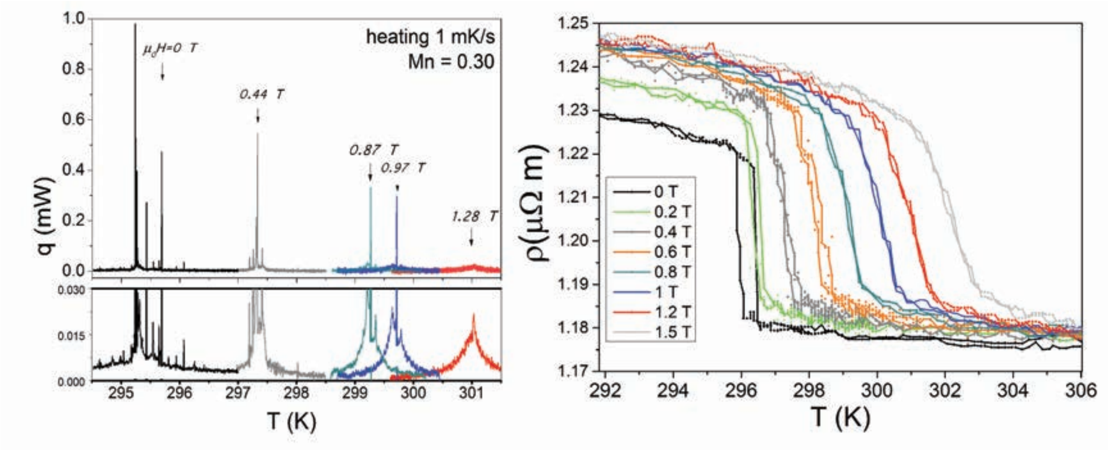

FIGURE 5.20: Left graph: Effect of the applied magnetic field on the heat flux signals at 1 mK/s sweeping rate for the sample y(Mn) = 0.30 of mass 4.53 mg: avalanches diminish in number and magnitude and then disappear above 1.1 T. Right graph: resistivity of a sample of Mn(y) = 0.30 of mass 5.26 mg as a function of temperature for different applied magnetic fields.

At zero field, a sharp negative jump in $\rho(T)$ occurs when the sample switches to the paramagnetic phase giving rise to a variation of the resistivity of about -3.7%. Although, the magnetic field slightly influences the magnitude of this jump a change of the slope of $\rho(T)$ at the phase transitions is found with increasing H. The samples used for ρ and q_s measurements were different, thus it was not possible to perform a one-by-one correlation between isofield sets of data of heat flux and resistivity, however similarities appear. At fields below 0.8 T, fast transformations of volumes give rise to sharp jumps of $\rho(T)$ and to multiple avalanches in the heat flux measurements. In both cases the number of jumps/avalanches changes with field and, as far the transition approaches the critical point, they disappear. The conduction electrons highlight the passage from a first to a second order transition produced by the magnetic field but the overall behaviour of electrical transport in La(FeSi)$_{13}$ based alloys requires further attention and a deeper discussion is postponed to the next chapter.

The magnetic phase diagram from the 50 mK/s and 1 mK/s sets of DSC measurements for the Mn(y) = 0.30 is reconstructed in Fig.5.21 (left graph). The increasing magnetic field reduces gradually the irreversible content of the transition, thus the critical point (first to second order transition) can be determined on the basis of the disappearance of thermal hysteresis for the first data set and by the disappearance of avalanches for the second data set. In particular, the temperatures of transition in the low rate scans were determined looking at the main isothermal peaks. The scheme on the right side of Fig.5.21 reports a simplified version of the avalanches transitions during FM to PM and PM to FM transitions. The heating and cooling peaks show a temperature region of intersection (yellow region of the graph) depending on the temperature hysteresis of the compound. This region is supposed to give rise to the metastability of the first order phase transitions, because the absorption/release of small quantity of heat due to the avalanches can be sufficient to transform other volumes fractions.

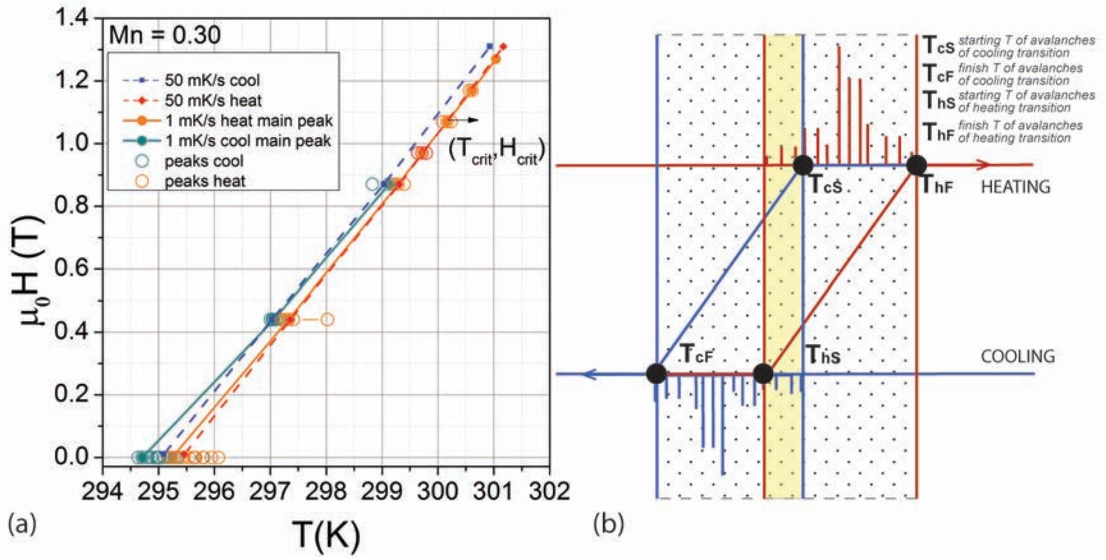

FIGURE 5.21: (a) Magnetic-phase diagram for the y(Mn) = 0.30 composition: the dots represent the temperatures of the peaks measured in the 1 mK/s scans (full dots main peaks, empty dots minor peaks). (b) Scheme of the temperatures of the avalanches in heating and cooling. The yellow region represents an intersection between the heating and cooling processes which can give rise to metastability.

From the low rate measurements we obtained lower values of critical magnetic field and temperature; this suggests a possible over estimation of the thermal hysteresis when it is computed from faster rate measurements, where the uncertainty of T is ± 0.2 K. (Fig.5.21 left graph).

Mn = 0.18: In Fig.5.23 it is shown that the single heat flux avalanche, detected at H = 0, lowers and sub divides gradually in many peaks. Far from the critical point, differently from the previous case, a single nucleation event seems to be sufficient to transform the entire volume of the sample whilst a strong energy barrier separates the two phases. As the external magnetic field is increased, the sample resumes a behaviour similar to that of the y(Mn) = 0.30 sample at zero field. This fact confirms that, although the Mn content modifies the position of the critical point, different compositions of the series can be described by very similar magnetic phase diagrams. Again, both the decrease of the peaks amplitude and the increase of the peak number suggest a re normalization of the nucleation energies involved in the transition with respect the energy barrier between the FM/PM phases. A noteworthy fact comes from the observation that the relaxation time of each avalanche changes in different applied magnetic fields. Due to the established experimental conditions, the low applied scanning rate, the small sample masses, the low thermal contact resistance and the irreversible processes at the transitions, the composed system, sample plus Peltier cell, has to be reconsidered. A new representation of the thermal equivalent circuit of the measurement Peltier cell and the sample is proposed with the aim to take in to account both the second and the first order phase transition behaviour. In the scheme of Fig.5.22, the sample is represented by its heat capacity and a heat flux generator. The latter represents those irreversible processes which are characteristic of a first order phase transition and are an intrinsic source of irreversibility. The specific heat term is embedded in the heat capacity, C_s, and it takes in to account for the reversible contribution due to a second order phase transition. The time constant related to the sample heat capacity is added to Eq.(5.5): $\tau_p \rightarrow \tau = \tau_p + \tau_s$. In the following it is explained how this is linked to the value of the reversible specific heat of the samples. After subtracting the value of τ_p = 2.6 s (calibrated for the thermal response of the setup), the time constant due to the sample becomes $\tau_s = R_s^{th} \cdot C_s^{th}$. By modifying the τ_s values with fields a better resolution of each avalanche can be obtained, even in multiple step transitions. A variation of the thermal contact resistance, R_s may be excluded due to the fact that the measurements were performed sequentially without changing the configuration: R_s mostly depends on the size of the sample and on the medium which separates it from

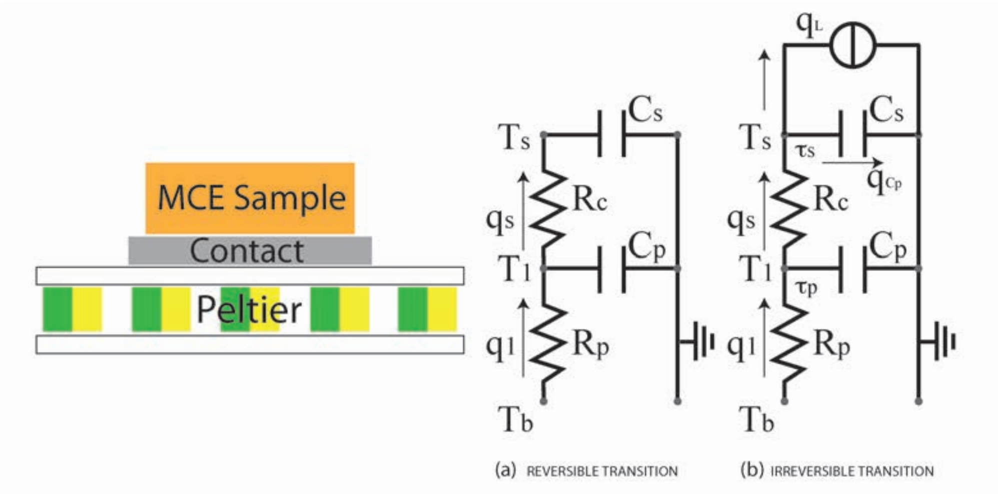

(a) REVERSIBLE TRANSITION (b) IRREVERSIBLE TRANSITION

FIGURE 5.22: Equivalent thermal circuits for the measurement Peltier cell when considering reversible (a) and irreversible (b) processes at the transition.

the Peltier measurement cell. It follows that C_s varies with field. A change of the specific heat of the sample can be inferred from the definition of thermal capacitance and its value is proportional to the filed dependent variations of τ_s.

$$\Delta C_s^{th}(H) = m_s \Delta c_p(H) = \frac{1}{R_s^{th}} \cdot \Delta \tau_s(H) \tag{5.14}$$

In order to relate the obtained values of τ_s with c_p, the whole mass of the sample was considered to be contributing to each avalanche (even in multiple step transitions), however, τ_s was calculated from the greatest or the last avalanche of each transition, because in this condition, the main part of the sample is supposed to be already transformed in the paramagnetic phase.

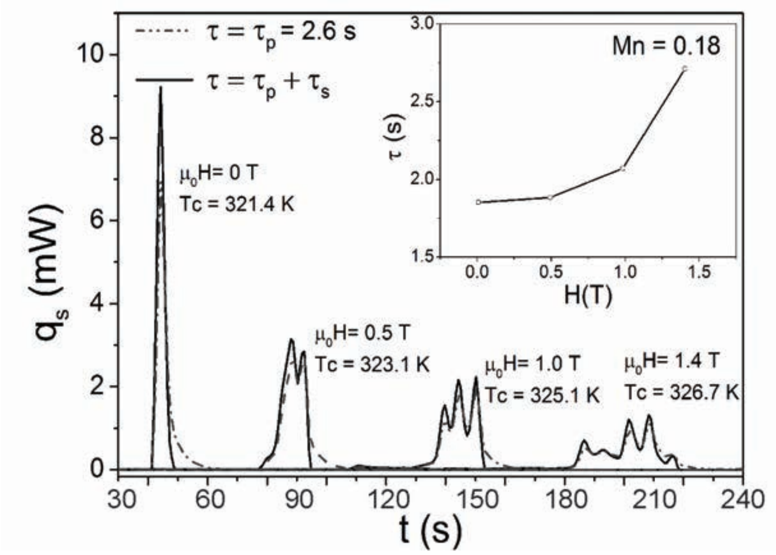

FIGURE 5.23: Effect of H on the evolution from single to a many peaked transitions (on heating) for the y(Mn) = 0.18 composition. Dashed lines represent the heat fluxes calculated without the correction of 2.6 s for the time constant of the Peltier cell (Eq.(5.5)); the continuous lines disclose the multiple peaks structures when the time constant of the sample is considered. Inset: τ dependence on the applied magnetic field, where τ_p was set at 2.6 s.

The same analysis was applied to both the y(Mn) = 0.18 and the 0.30 compositions obtaining a master curve for the reversible specific heat of transition as a function of the distance from the critical point, Fig.5.24. The value of c_p from the two data set increases of about 150% and subsequently, when avalanches stop, it tends to the value of the specific heat peak of the Mn(y)=0.46 composition (Fig.**??** (c)), whose zero field transition is of the second order. The thermal contact resistances for each sample was estimated to calculate the value of c_p. In the case of first order phase transitions with avalanches, the rescaling procedure failed, thus the thermal resistance for the y(Mn) = 0.18 composition was obtained using the value of c_{PM} in table 5.1. Since the zero field transition is fully of the first order, no specific heat of the transition is expected and the paramagnetic value can be taken as a reference. Differently, the thermal resistance for

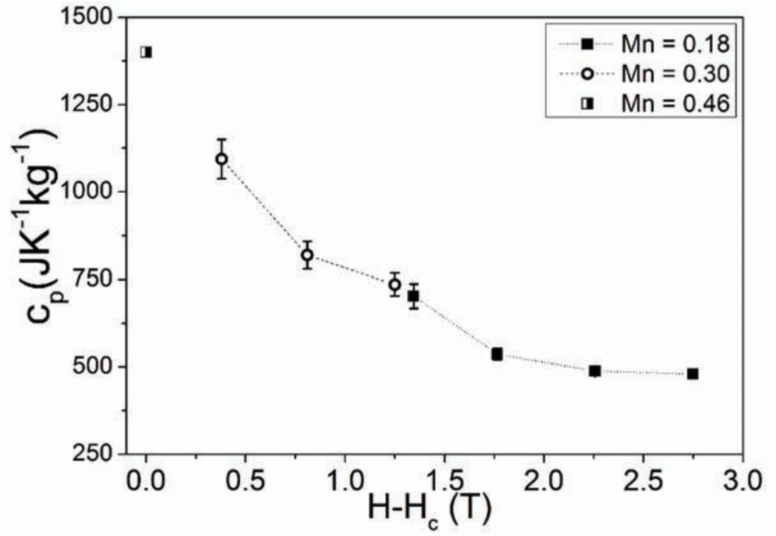

FIGURE 5.24: Master curve of the specific heat as a function of the distance from the critical field The values were extrapolated from the measurements of τ_s for the two composition y(Mn) = 0.18 and y(Mn) = 0.30.

the y(Mn) = 0.30 composition was chosen in order to match the points obtained from the y(Mn) = 0.18 and y(Mn) = 0.46 compositions. The resulting values for the thermal contact of the samples y(Mn) = 0.18 and y(Mn) = 0.30 are respectively 806 KW^{-1} and 560 KW^{-1}, these numbers can be reasonably considered as being compliant to Eq.5.11. Such c_p dependence was already pointed out in several works by Morrison et al., by the use of microcalorimetry methods. Noteworthy, in this work, the c_p of the transition was obtained by considering that the shape of the avalanches depends on the reversible specific heat of the compound.

The scanning calorimetry technique revealed the strong interplay between specific heat and latent heat terms at the PM/FM transition of La(FeSi)$_{13}$ based compounds. The reversible c$_p$, which is an intrinsic thermodynamic property of the compound, is also a parameter which governs the avalanches kinetics of the phase transitions. For what concerns the application of these class of materials, in magnetic refrigeration cycles, some important results can be considered. The time required to exchange the heat (τ_s) with the surrounding (the Peltier cell of measure here) is found to be significantly shorter in first order phase transitions, due to the smaller contribution of the heat capacity found by looking at the shape of avalanches. On the other hand, since the hysteresis is an even stronger limit for the application, and it governs the time scale for adiabatic cycles, due to the existing close relation between thermal hysteresis and heat avalanches, we may expect that the time for an avalanche to start and to end may critically depends on the hysteresis.

6

Other experimental methods applied to magnetic phase transitions

In this chapter, phase transitions in magnetic solids are investigated exploiting different experimental techniques. The electrical properties of the La(Fe,Si)$_{13}$ based compounds, presented in previous chapter, were measured at different magnetic fields and temperatures. These experiments may provide some additional information on the nature of their magneto structural phase transition. The last part of the chapter is dedicated to a very different system. A vector network analyser ferromagnetic resonance method (VNA-FMR) has been developed for in-temperature measurements of the magnetization dynamics in a Mn$_2$RhSn Heusler thin film [85]. The interest devoted to such material derives from its spin reorientation transition, taking place around 77 K, which may be favour the inset of a skyrmion topological state. The choice of the setup is ascribed to the possibility to change the direction of the applied magnetic field either perpendicular or parallel to the plane of samples, making possible to investigate the directions of magnetic subsystems in the compound.

All the in-field measurements, presented in this chapter, were performed by using cryostats opportuney designed to fit in the room temperature bore of a 6 T Cryomagnetics cryo-free magnet in use at the Politecnico of Torino.

6.1 Electrical transport

Electron transport properties can be investigated by measuring the response of conduction electrons to a temperature gradient or to external fields such as an electric field, a magnetic field, or a combination of both, applied to a specimen. By means of a standard four points techniques it is possible to measure the basic transport properties of alloys subjected to external constrains, including magnetoresistance and electron thermal conductivity. The La(Fe,Si)$_{13}$ based alloys, previously investigated by the MOIF (Ch. 4) and DSC measurements (Ch. 5), were thus selected to observe the electrical response at the first or second order magneto-structural phase transition in the presence of different applied magnetic fields, perpendicular to the sample surfaces.

6.1.1 Experimental setup

The electric transport characterization was performed in a Leybold cryogen free cryostat where the sample temperature can be varied from 10 K up to room temperature. The temperature was set and controlled by means of an Oxford ITC503 temperature controller. The measurements were performed under continuous current condition. A Keithley current sources was generating bias currents ranging from from 1 mA to 3. The data acquisition system is provided by a 2182A Keithley nanovoltmeter coupled to an 8-channel Keithley 7001 scanner, which was used to simultaneously monitor different voltages along the sample. By a standard four points probe technique, with contacts made with silver paint, it was possible to analyse the temperature dependence of the electrical resistivity, ρ, and the magneto-resistance, MR, for different compounds. The samples were inserted into a vacuum chamber and positioned on the cold finger of the cryostat.

6.1.2 Electrical resistivity of La(Fe,Si)$_{13}$ based compounds

In Ch.5, it was shown that the conduction electrons highlight the passage from a first to a second order transition produced by the magnetic fields. In particular, this variation was shown for the sample LaFe$_{11.41}$Mn$_{0.30}$Si$_{1.29}$-H$_{1.65}$ by applying a magnetic field of $\sim$ 1.3 T. The electrical resistivity of the compound was measured vaying the temperature across the Curie point at different external magnetic field (6.1 left graph).

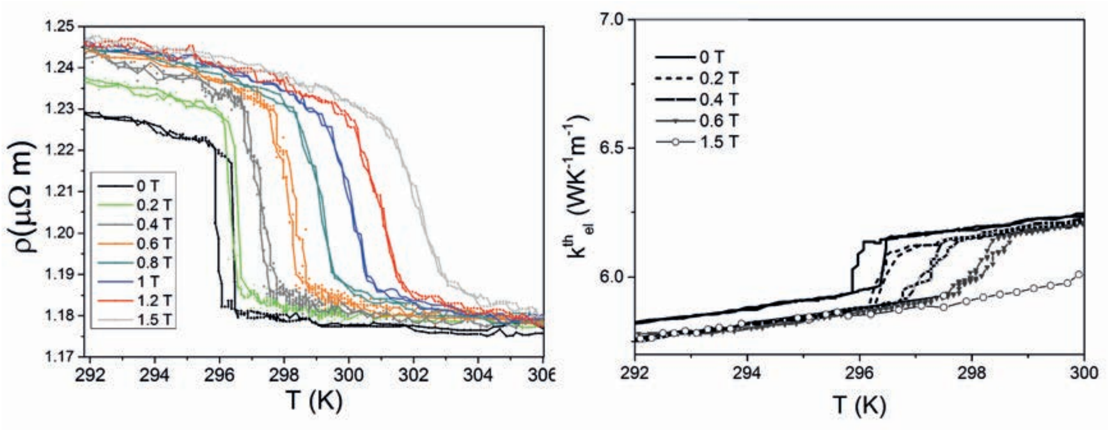

FIGURE 6.1: Left graph: electrical resistivity dependence on T of the sample with Mn(y) = 0.30. Right graph: calculated electronic thermal conductivity contribution from the Wiedemann–Franz law.

With regard to the electronic transport transition, it is known that when a system is magnetically ordered, no spin disordered scattering is expected [86] [87] and the FM phase should have a lower resistivity with respect to the PM phase. Differently, for La(FeSi)$_{13}$ based compounds, ρ experiences higher values in the FM state. It should be pointed out that this effect could be of non magnetic origin. Many works already observed a connection between ρ and the lattice contraction taking place at the phase transition [88] [89]. A first explanation for the La(FeSi)$_{13}$ based compounds was given by Palstra [90] on the basis of the work on Fe$_3$Pt alloys [91] by Viard and Gavoille, who described the phonon resistivity dependence on the specific volume. The structural transition in La(FeSi)$_{13}$ produces a reduction of the lattice parameter, thus a corresponding decrease of the scattering due to phonons is expected [92]. In the work published by Piazzi [63], the coupling between magnetic and structural degrees of freedom was modelled to reproduce the magneto-structural transition of this and others similar compounds. The nice agreement reached between theory and experiments demonstrated that the entropy depends on terms of magneto-volume coupling. A possible explanation of the anomalous behaviour of $\rho(T)$ can be ascribed to the volume contraction which lowers the electron-phonon resistivity contribution in the PM phase (i.e. the lattice entropy), according with the theoretical calculation which predicts a lower entropy contribution of the PM lattice.

The observed jumps in the electrical resistivity for the sample of LaFe$_{11.41}$Mn$_{0.30}$Si$_{1.29}$-H$_{1.65}$ also imply a change in the electronic thermal conductivity between the PM and the FM phases. The entity of such variation (right graph of Fig.6.1) has been calculated for several applied magnetic fields, on the basis of the Wiedemann–Franz law, from the resistivity data:

$$k_{el}^{th} = \frac{LT}{\rho} \tag{6.1}$$

In the formula, L is a constant having a value of 2.45 10^{-8} WK^{-2}. The k_{el}^{th} is found to be of 6.22 WK^{-1}m^{-1} in the PM phase, while the FM value is decreased of about 3.7-5 %. This is a small contribution to the overall thermal conductivity of the sample [10], but may be not negligible when looking at the details of the dynamics of first order phase transition. In fact, this behaviour corresponds to a lower capacity of the ferromagnetic phase to conduct heat, which may be considered also in refrigeration cycles in this and others materials.

Further information on the electronic response at the phase transition can be found looking at the magnetoresistance, MR, behaviour. The MR values, displaced in Fig.6.2 were obtained by subtracting a reference value of ρ in zero applied magnetic field $MR = (\rho(H) - \rho(0T))/\rho(0)$. As it is shown in the graphs, the ferromagnetic phase (at 280 K) has a MR of 1.3 %, while in the PM phase (310 K) the measured MR is almost zero. The right graph of Fig.6.2 confirms that the magnitudes of the MR jumps as a function of T are almost insensitive to the external applied magnetic field at the transition. Nevertheless, the thermal hysteresis disappears, in accordance to a second order transition.

The difference in the absolute values of ρ of the two phases, together with the different magnetic orders, which are reflected in the MR response, makes these transition observable by electrical measurements, and, the ordinary resistivity seems to reflect the transformation of different volumes inside the sample, as it was pointed out in the calorimetry experiments of Ch.5.

A further example is furnished by the measured resistance of the

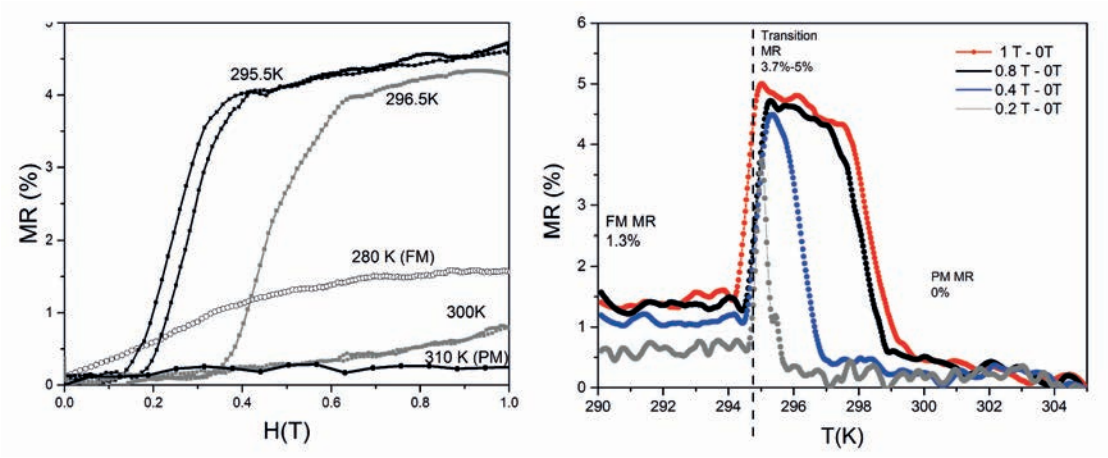

FIGURE 6.2: Magneto resistance measurements of the y(Mn) = 0.30 composition at several temperatures above, below and across the curie point. Right graph: The MR as a function of the temperature. The slope was calculated subtracting the slope of ρ vs T, measured at $H = 0$.

La(Fe$_{0.9}$Co$_{0.015}$Si$_{0.085}$)$_{13}$ alloy. This composition was observed by MOIF experiements in Ch.4. The $R(T)$ curves of Fig.6.3 show that, each time the compound

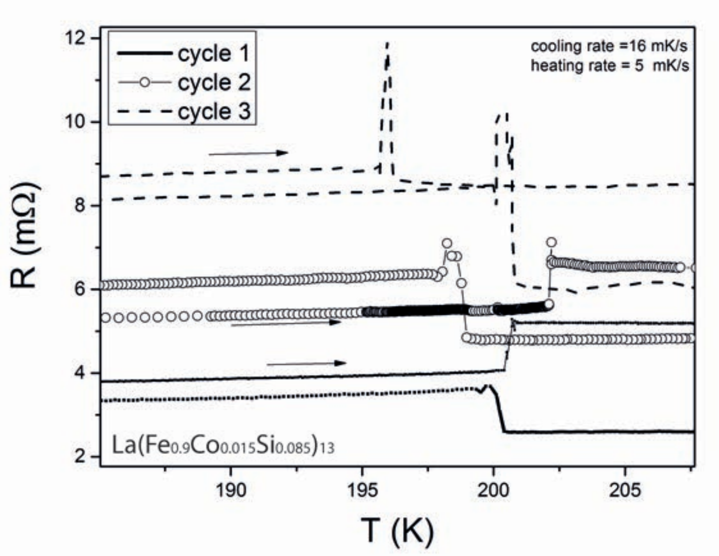

FIGURE 6.3: Induced irreversibility in resistance measurements of the La(Fe$_{0.9}$Co$_{0.015}$Si$_{0.085}$)$_{13}$ investigated by MOIF, Ch.4.

crosses the T_c, the resistance changes toward higher values, indicating that cracks are formed during the transition, causing an overall increase of the resistivity. This behaviour is attributed to the lattice expansion due to the PM to FM transition. In this case, the sample was a sintered material, thus the lattice stress at the transition may easily produced such irreversible modifications of the current path. The electrical resistivity furnished also informations about the mechanical properties of different compositions and/or preparation route, due to the high sensitivity of the conduction electrons on cracks.

6.2 Ferromagnetic resonance

The magnetization vector of a spin ordered system, $\vec{M}$, can be considered to precess uniformly around its equilibrium direction due to the torque exercised by an external magnetic field $\vec{H}$, as depicted in the scheme of Fig.6.4(a). The phenomenological equation describing this motion is the Landau-Lifshitz-Gilbert (LLG) equation, which also considers a dissipation mechanisms that pushes the magnetization in the direction of an effective field (Fig.6.4(b)).

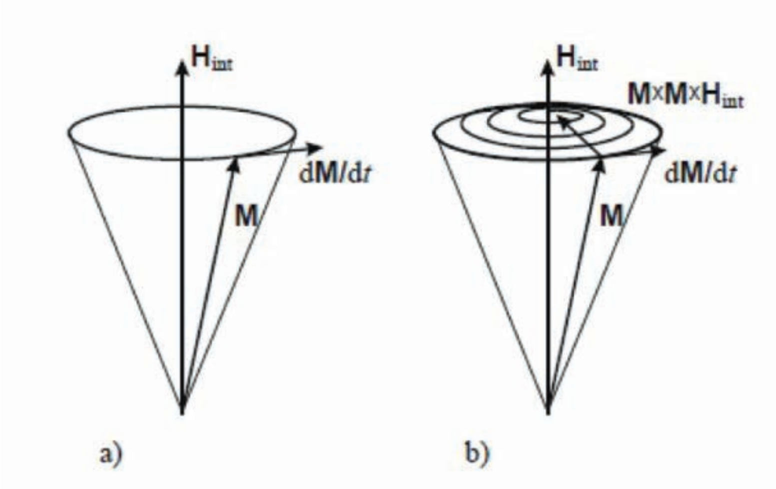

FIGURE 6.4: Undamped (a) and damped (b) gyromagnetic precession.

From this theory, the frequency with which the magnetization preceeds around the applied field is the ferromagnetic resonance (FMR) frequency $\nu_{res} = 2\pi\omega_0$ and it is the eigen frequency that is found in the solutions of the (LLG) equation:

$$\frac{\partial \mathbf{M}}{\partial t} = \gamma\mu_0 \mathbf{M} \times \mathbf{H}_{eff} + \frac{\alpha}{M_s}\mathbf{M} \times \frac{\partial \mathbf{M}}{\partial t} \tag{6.2}$$

where $\vec{H_{eff}}$ is the effective magnetic field acting on the magnetization vector, α > 0 is the Gilbert damping constant, which depends on the material and shows typical values ranging from 0.001 to 0.1, and M_s is the saturation magnetization of the sample. This equation is of fundamental importance to understand the role of structure and external constrains on the magnetization dynamics in ferromagnets, since the effective field acting on $\vec{M}$, depends on a variety of factors, comprising any magnetic anisotropy, geometrical constrains, ... A solution for the Eq(6.2) was proposed by Kittel in 1948, providing the generalized form for the field dependence of the ferromagnetic resonance frequency of a uniformly magnetized and isotropic material, taking into account the demagnetizing field due to the sample geometry (N_x, N_y, N_z):

$$\omega_0 = \gamma\sqrt{[H + (N_x - N_z)M_s][H + (N_y - N_z)M_s]}. \tag{6.3}$$

The magnetization dynamics theory can be used to perform broadband investigation of thin samples, in a wide frequency range up to several tens of GHz, in order to look at the relation among physical constrains contributing to the material spins structure, i.e. anisotropy field and saturation. On the other hand, this theory is also important for technology. Very different requirements on the FMR frequency and the Gilbert damping parameter have to be met in different devices, for example microwave absorbers based on ferromagnetic nanoparticles require large damping ($\alpha \simeq 1$), whereas in general all applications related to memory storage require a very low Gilbert damping $\alpha \simeq< 0.01$.

6.2.1 VNA-FMR experimental setup

In ferromagnetic resonance experiments, forced precession oscillations of the magnetization are excited by means of a high-frequency magnetic field. In a conventional setup, the sample is placed in a magnetic field, which creates the Zeeman splitting of energy levels. Simultaneously, a second alternating field of a fixed frequency is irradiating the sample exciting the magnetic dipole transitions between the split Zeeman levels. When the precession frequency of local magnetic moments reaches the value of the applied microwave frequency, the resonance condition is fulfilled and the microwave power is absorbed by the sample. The high frequency (hf) field can be provided by a vector network analyzer (VNA), which is an instrument that measures the amplitude and the phase of the scattering parameters (S-parameters) of a generic two port device. This instrument has a built-in frequency signal source and can perform frequency sweeps up to several GHz, measuring the complex reflection and transmission coefficients of two-port and one-port networks. Given a sample with planar geometry, it can be tested with the VNA by means of a coplanar waveguide (CPW) excitation structure. A coplanar line is a structure in which all the conductors supporting wave propagation are located on the same plane. Conventional CPW consist of a single conducting track printed onto a dielectric substrate, together with a pair of return conductors, one to either side of the track. The return conductors are separated from the central track by a small gap, which has an unvarying width along the length of the line. The sample, in this case, is placed on top of the center conductor, as shown in Fig.6.5(a), thus that the perturbation on the hf signal produced by the interaction of the electromagnetic wave with the sample is directly registered by the CPW-VNA transmission (and reflection) line. Depending on the measurement, a static bias field can be applied either in the film plane (IP), or out of plane (OOP), but, in both cases, it has to lie perpendicularly to the microwave field provided by the VNA. With this setup is possible to obtain the frequency dependence of the S-parameters at a fixed field, also referred to as frequency sweep FMR. Assuming that the dominant CPW mode is the transmission mode, reflections can be neglected in the experiments, thus that only the S_21-parameter of the measurement and the correspondent reference measurement are needed. According to the Barry model [93] [94] [95], it is possible to obtain an uncalibrated effective microwave permeability parameter u(f), which is related to the magnetic permeability μ_r of the sample:

$$u(f) = \pm j \frac{ln \frac{S_{21,H}(f)}{S_{21,ref}(f)}}{lnS_{21,ref}(f)} \tag{6.4}$$

where the sign is chosen so to make Im[u(f)] negative in the vicinity of the FMR peak. $S_{21,H}(f)$ denotes the set of S_{21} parameters measured at the given static bias field H, and $S_{21,ref}(f)$ is the set of S_{21} parameters measured for the field chosen as reference. Both the $S_{21,H}(f)$ data and the $S_{21,ref}(f)$ reference data are needed, in order to compensate for the response properties of the excitation structure, feed cables, etc., that do not relate to the sample response. Usually, the reference measurement is made in a saturation condition of the sample. It is emphasized in [94] that u(f) is related, but does not strictly correspond to the loss and dispersion profiles which are expected. One example of u(f) measured for a 50 nm thick NiFe nm is shown in Fig.6.5(b). The quantity -Im[u(f)] is related to the loss profile, while Re[u(f)] shows its dispersion profile.

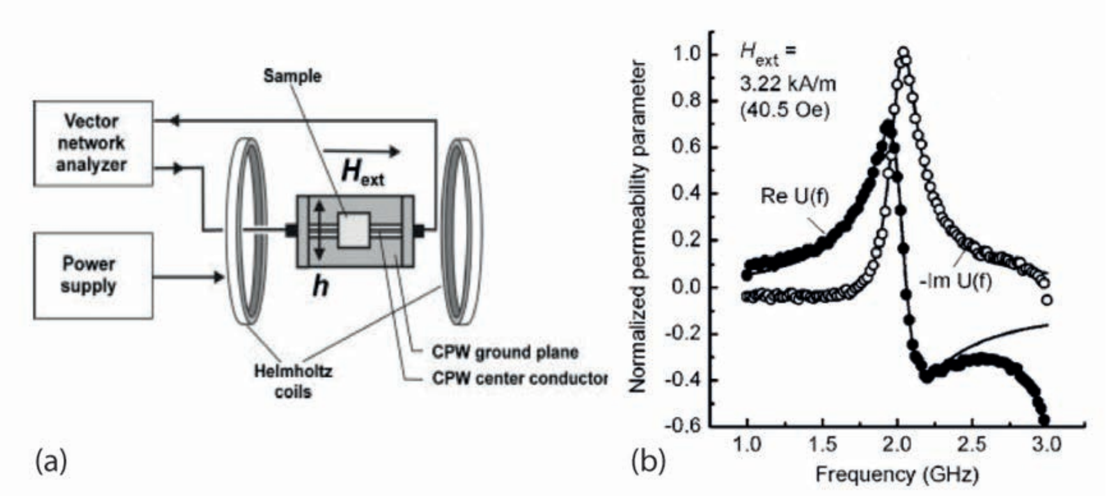

FIGURE 6.5: (a) Schematic diagram of the vector network analyzer ferromagneic resonance spectrometer. The sample is placed on the CPW structure. The mutually perpendicular static applied field H_{ext} and the microwave field h_{rf} lie in the plane of the film. (b) Representative VNA-FMR data showing the normalized permeability parameter U(f) of a 50 nm thick NiFe nm (Eq.(6.4))[95] [94]

.

The VNA-FMR setup was used to detect the behaviour of the resonance frequency peak of thin film samples when the temperature was varied from 4 K up to room temperature. The VNA can provide for hf signals up to to 40 GHz, by using low temperature cables inserted in a cryostat working in liquid helium flux. The temperature control was made by using a heater positioned close to the CPW line, which was optimized to fit in the cryostat in order to apply the external magnetic field either perpendicular or parallel to the CPW plane.

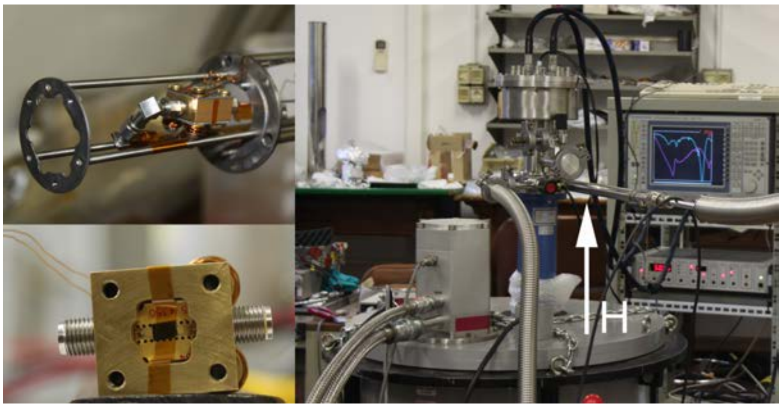

FIGURE 6.6: Picture of the VNA-FMR setup for low temperature in use at Politecnico of Torino.

6.3 Spin reorientation transition in Mn_2RhSn

The complex non collinear magnetic behaviour of Mn_2RhSn indicate the realistic possibility of engineering the skyrmion states in this and in similar Heusler systems. A detailed micromagnetic analysis which suggests this collinear regime to provide perfect conditions for the Skyrmion formation, in agreement with the earlier theoretical studies is reported in [96]. A correct combination of energy terms arising from spin and lattice interactions, shape and magnetic anisotropy needs to be choice to permit an experimental investigation of these topological states. To understand the origin of magnetic skyrmions, important steps were made in 1960 and 1961 respectively by Dzyaloshinskii [97] and Morya [98], who theorized and understood the existence and the role of a new exchange interaction energy term, the Dzyaloshinskii-Morya interaction, DM. On the basis of the Landau-Ginzurg theory of phase transitions, they considered the broken inversion symmetry contribution of spin-spin interactions in magnetic crystals arising from the spin orbit coupling term. Dzialoshinsky showed that, for a certain energy configuration, a canted state of magnetic sublattices is favoured better than an antiferromagnetic alignement. Because of the D.M. interaction, adjacent magnetic spins can thus prefer to have a fixed angle between each other and energetically stabilizes magnetic skyrmions. In this theory and its evolution, these stable states can persist in a wide range of external conditions, such magnetic fields or temperature, but it is also possible to perturb the system so to destroy, restore or slightly modify the equilibrium. The technological interest is thus motivated by the possibility to control a phase transitions and combine it with the storage potentials of magnetic media, thus that skyrmions may represent a new type of nanoscale data carriers [99].

The crystal and magnetic structures of Mn_2YZ Heusler compounds is showed in Fig.6.7(a) [96]. Due to the magneto-crystalline anisotropy induced by the tetragonal distortion, the Mn-I magnetic moments are oriented along the c-axis; the moments on Mn-II are canted in an alternating manner with respect to the c-axis. A schematic picture of the leading magnetic exchange interactions between different atomic layers in Mn_2YZ (atomic planes containing Z and Y elements are shown in blue and red, respectively) is also reported in Fig.6.7 (b). The arrows show the orientation of the spin moments on Mn and the springs show the exchange interactions between different planes. Considering only the nearest antiparallel interactions J (between Mn-I-Z and Mn-II-Y planes) leaves the magnetic structure collinear; introducing the next-nearest antiparallel coupling j (between Mn-II-Y planes) leads to the alternating canting of Mn-II moments by θ and 2π-θ. Three main temperature regions can be distinguished and are highlighted in Fig.6.7(c): Canted (red), collinear ferrimagnetic (yellow) and disordered (blue) magnetic states of Mn_2RhSn. The increase of the canting angle occurs because of the simultaneous re-alignment of the Mn-II moment and an increase in its absolute value. This, in turn, suppresses the Mn-I moment from 4.5 to 3.5 μB.

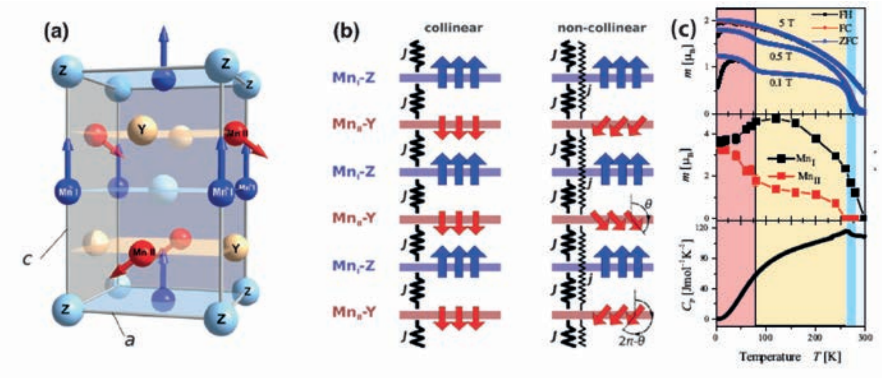

FIGURE 6.7: (a)Crystal and magnetic structures of Mn_2YZ Heusler compounds.(b) Schematic picture of the leading magnetic exchange interactions between different atomic layers in Mn_2YZ (atomic planes containing Z and Y elements are shown in blue and red, respectively).(c) Zero-field-cooled (ZFC), field-cooled (FC) and field-heated (FH) magnetization as a function of the temperature measured at induction fields of 0.1, 0.5, and 5 T.

The Heusler compound Mn_2RhSn is thus predicted to have a spin reorientation transition from an out of plane to an in plane orientation [96] of spin sublattices. In this region of the phase diagram ($\simeq$ 77 K), whit a correct balancing of terms in the energy equation of the spin structure, it should be possible to stabilize the canted spin state and manipulate it under a small applied field. An imposed anisotropy was reached by film depositions [100], and motivated the in temperature experiments with different experimental technique on the compound. In particular, a correlation between the magnetization dynamics and the static magnetic properties of a 50 nm Heusler thin film of Mn_2RhSn grown on MgO(001) substrate by magnetron co-sputtering of the constituents [85], has been initiated in this Ph.D.

6.3.1 MFM measurements

A Magnetic Force Microscope (INRiM laboratory) has been equipped with a temperature module in order to vary the temperature of the sample. The module uses a Peltier cell to obtain temperatures between -35 C and 100 °C. The sample holder and the magnetic tip were isolated from the external environment by a silicon tube, inside which it was possible to flow Ar gas in order to work in a controlled atmosphere. A water pump was used to cool the bottom side of the Peltier cell. A picture of the experimental setup is presented in Fig.6.8 (e). The images at the surface of the Heusler thin film of Mn$_2$RhSn were acquired using a hard magnetic tip without applying any external magnetic field. All the magnetic images were compared with the topology recorded in pass one. At 22.3°C no magnetic signal was detected (image not shown), after that the sample was cooled down. The first magnetic signal was detected after that the temperature reached the value of -19.8°C. At the stable temperature of -19°C, an image was recorded in a 768 X 768 px window of 30 μm lateral size. In Fig.6.8 (a) and (b), the magnetic contrast is compared to the topology (left and right frames respectively). The magnetic pattern, of Fig.6.8 (a), discloses a bubble-stripe behaviour of ferromagnetic domains, which is compatible with an out-of-plane anisotropy in the absence of external magnetic fields [65]. An image, recorded in a smaller window (10 X 10 μm), is also reported in Fig.6.8

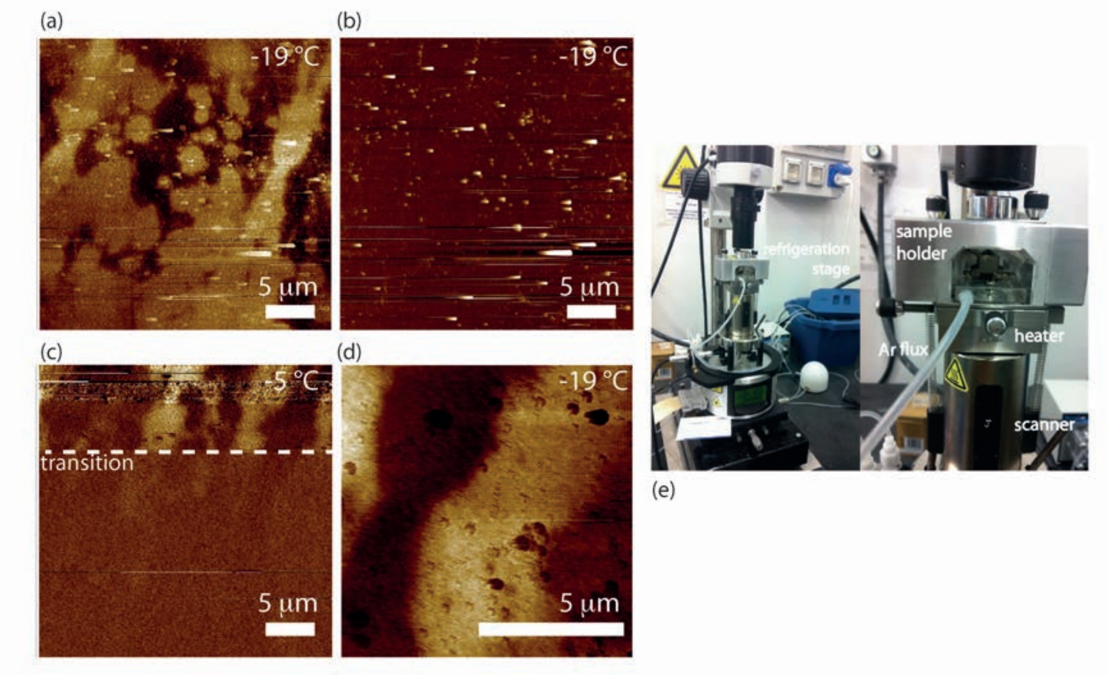

FIGURE 6.8: (a) and (b) magnetic and correspondent topology MFM images of the Mn$_2$RhSn film below the Curie temperature. (c) Magnetic images at the first order phase transition while heating the sample. The Curie temperature is predicted around 0 Celsius.(d) zoomed bubble-stripe domain structure. (e) MFM equipped with temperature module.

(d). The system was then slowly heated up to room temperature. An image, recoded at -5°C during the heating process, shows that the stable bubble-stripe domain pattern persists but gradually lowers its magnetic intensity with respect to the -19.8°C image Fig.6.8 (c). Moreover, the pattern disappeared during the acquisition (white dotted line). This behaviour was attributed to the inset of the disordered high temperature paramagnetic phase. The abrupt disappearance of the domain pattern at -5°C, together with the fact that the cooling and heating temperature of the transitions (-19.8°C and -5°C respectively) were different, suggested that the transformation is accompanied by instability and hysteresis, being of the first order. These data are in good agreement with the magnetic phase diagram of the compound, which predicts the inset of the ferrimagnetic order at temperature below 300 K with an increasing value of the out of plane component of the Mn-I atoms Fig.6.7(c).

6.3.2 VSM measurements

The magnetic hysteresis loops were measured with a vibrating sample magnetometer (VSM) in the temperature interval [20,300] K. Several hysteresis loops, at different temperatures, were recorded applying the external magnetic field either parallel and perpendicular to the film plane (IP and OOP directions).

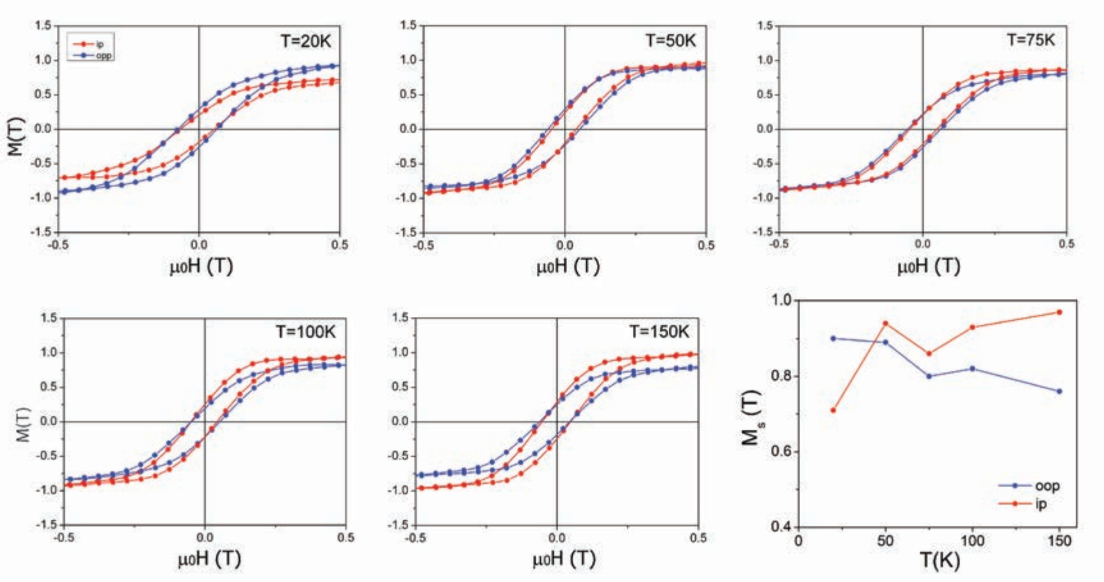

FIGURE 6.9: Hysteresis loops measured with VSM with the magnetic field applied perpendicular (OOP) and parallel (IP) to the sample surface. The geometrical demagnetizing factor is not considered due to the trivial spin structure.

From the static magnetic measurements, it was found that the OOP component did not change in the whole temperature range of measure [20-150] K, while a significant variation in the saturation magnetization of the IP component was observed. The graphs in Fig.6.9 summarize this behaviour. The coercive fields are small ($\sim$ 0.04 T) and comparable for both the directions. Due to the difficulty to estimate a demagnetizing factor of such a complex spin structure, no geometrical correction were made for the two configurations. However, for thin film geometry, the geometrical demagnetizing factor is usually very close to $N_z = 1$ [30] in the orthogonal direction. The OOP direction can thus be considered the easy axis for the system, which keeps nearly unchanged in the whole temperature range of measure. On the other hand, the IP subsystem magnetism decreased below 75 K, which may confirm the alignment of the two subsystems, but it may also counts for a certain staggered component of the magnetization, which resides in the film plane. The temperature dependence of the saturation magnetization for the OOP and IP spins components is reported in the last graph of Fig.6.9. The IP and OOP magnetization behaviour are in accordance with the predicted change of spin directions of the Mn-II atoms Fig.6.7(b).

6.3.3 FMR measurements

To probe the coupling between the magnetization vector and the crystal directions, temperature and angle dependent ferromagnetic resonance (FMR) spectroscopy [101] can be used. Thin ferromagnetic layers are perfect sample form, due to their defined orientation of crystallographic axes and the small amount of a metallic material that is exposed to microwave radiation. One more condition is that, for the homogeneous excitation, the film thickness should be smaller than the microwave skin depth. The measurements were conducted by applying external magnetic fields, produced by the superconducting magnet, in both the OOP and IP direction of the film plane. The geometry of the setup is sketched in Fig.6.10.

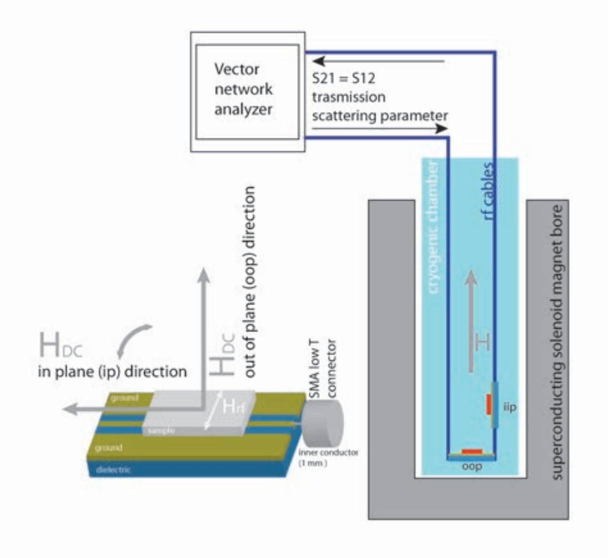

FIGURE 6.10: Scheme of the geometrical configuration for FMR experiments. A cryostat is inserted in the bore of a superconducting solenoid magnet. RF cables are cryogenic and can reach 40 GHz.

In both cases, the measurements of the thin film were analysed varying the temperature of the chamber. A frequency sweep spectra taken at T = 300 K was used as a reference. The external magnetic field was kept constant at the values of 200 mT and 100 mT for the IP and OOP directions respectively. Some representative results are shown in Fig.6.11.

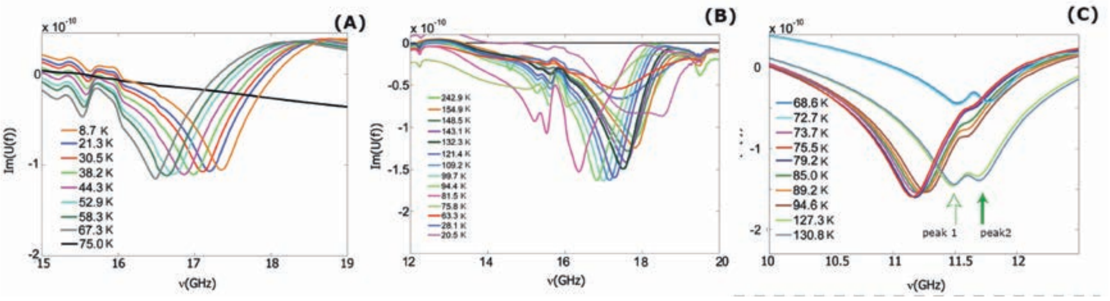

FIGURE 6.11: (a) In plane FMR spectra between 8 K and 75 K, with an applied magnetic field of 200 mT, (b) Out of plane FMR spectra between 140 K and 75 K with an applied magnetic field of 100 mT. (c) Double peak structure in the in plane component persists between 75 K to 140 K with an applied magnetic field of 200 mT.

The collected spectra are visibly disturbed, moreover, the signal arising from the ferromagnetic film is very low. In spite of the difficulty of such measurements, some observation can be done and the evolution of the resonance frequency values either of the IP and OOP components can be established in the temperature range between 20 K and 150 K. From the graph of Fig.6.12, a critical temperature region appear around [70,80] K.

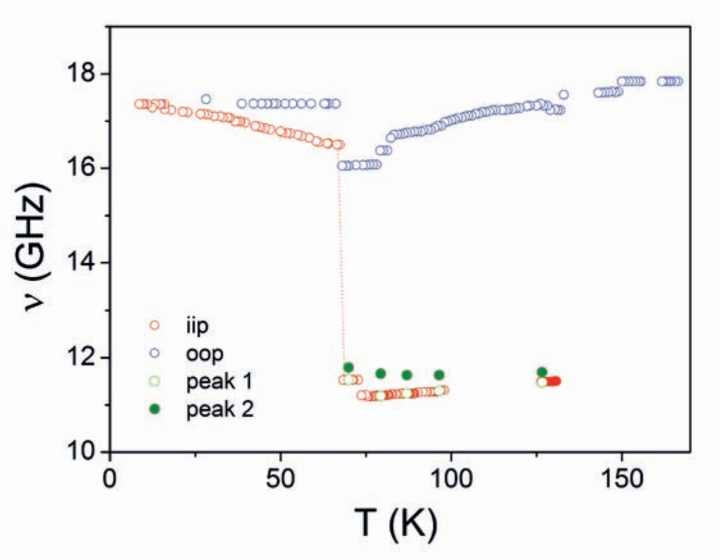

FIGURE 6.12: Temperature dependence of the resonance frequency for the two orientations, in plane (red dots) and out of plane (blue dots). A double peak structure appears in the IP component, as highlighted in figure 6.11 (C).

A phase transition arount 75-80 K may be inferred from the minimum of the OOP-FMR frequency value and from the behaviour of the IP component, which suddenly grows. The aforementioned phenomenology may be connected to the spin reorientation transition, predicted for this alloy [100]. The spin reorientation process can be accompanied by a stable canted state. The observation of a double peak structure of the IP-FMR component in the temperature interval above 70 K has been highlighted in the graphs, due to the similar behaviours observed in the metallic, semiconducting and insulating chiral magnets MnSi, $Fe_{1-x}Co_xSi$ and Cu_2OSeO_3 performed by Schwarze et al. [102]. However, in order to compare this behaviour, a theoretical calculation of the expected resonance frequency should be carried out also on the Mn_2RhSn compound.

The Kittel equation, for the out of plane geometry, can be used to relate the resonance frequency values to the magnetic properties of the sample under investigation. In this case, by combining the values of the saturation magnetizations obtained by the VSM experiments, it has been possible to reconstruct the evolution of the value of the anisotropy field H_a with temperature in the OOP direction. The resonance frequency results [103]:

$$\nu_0 = \frac{\gamma}{2\pi}(H_\perp + H_a - N_z Ms). \tag{6.5}$$

where γ is the gyromagnetic ratio (176 GHz/T). The demagnetizing factor for the thin film geometry was considered as N_z = 1, however it has to be noted that it may be smaller.

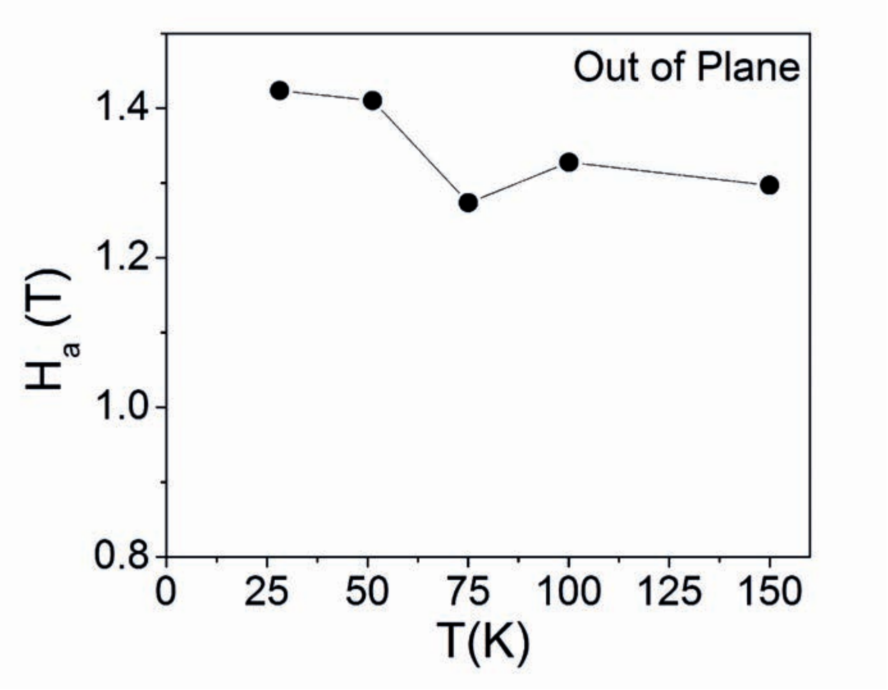

FIGURE 6.13: Calculated anisotropy field for the out of plane component from the Kittel formula of Eq.(6.5).

In Fig.6.13, the results for the OOP anisotropy field H_a reveals a high anisotropy which persists in the whole temperature range. In a small temperature window [50,100] K, the anisotropy field is lowered. This may arise from the inset of the canted state of the spin structure, which slightly lowers the strong out of plane anisotropy of the thin film, observed by the MFM images and the VSM magnetization curves. Due to the complex spin structure, the present compounds should deserve a deeper theoretical and experimental investigation. However, the experimental VNA-FMR setup here developed has been able to capture some of the feature concerning the spin reorientation transition in the Mn_2RhSn thin film. The existence of a canted state (canted angle) between the two Mn subsystems may be related to the presence of the double peak structure of the IP-FMR spectra. The concomitant deviation from a continuous behaviour either of the OOP and IP resonance frequencies is probably the most promising feature to be exploited in future investigation in this and in similar alloys characterized by an out of plane anisotropy and a reorientation of subsystems of spins.

7

Conclusions and future perspectives

This Ph.D. thesis has been devoted to the experimental study of phase transitions in magnetic solids. The main interest has been directed to La(Fe,Si)$_{13}$ based compounds, whose transition from a low temperature ferromagnetic phase to a high temperature paramagnetic phase is magneto-structural. This class of alloys is important for magneto refrigeration applications because of their unique magnetocaloric properties: low thermal and magnetic hysteresis, tunable T_c, near ambient temperature, and large MCE values, which are maxima in compositions with a first order phase transition. With the aim to achieve a proper understanding of the origin of their functional properties, the difference between a second and a first order transition have been exploited with dedicated experimental techniques and methods, producing a variety of results and seeding the possibility of further research in the field.

SPATIAL PROPAGATION OF THE TRANSITION FRONT

A magneto optical setup based on the use of indicator films (MOIF) was successfully applied to a magnetocaloric compound in Ch.4. The technique allowed to observe the magnetic response across the entire surface of La(Fe$_{0.9}$Co$_{0.015}$Si$_{0.085}$)$_{13}$ samples with typical lateral size of millimetres. In the experiments, a very low content of Co was utilized thus to preserve a first order transition around 200 K, allowing to investigate either the effect of substituted compound and the first order nature of the transition. The stray field produced by the samples was recorded in real time by varying the temperature of the cryostat chamber and by applying magnetic fields up to ± 75 mT. The experiments succeeded to obtain a different light contrast of the two phases of the compound: the paramagnetic phase was much darker with respect the ferromagnetic one. The difference in light (magnetic) contrast of the two phases clearly demarcated a phase front and, due to the magneto-structural nature of the transition, the motion of the front was observed to move across the entire sample surface at temperatures close to the Curie point. It has been thus possible to follow the advancement of the PM/FM (and vice-versa) transition, to measure its average velocity and to correlate it with the shape and the defects present at the surface of the sample. The main result obtained from this study is the evidence of two dynamics competing in the transformation process: a slow 2D growth of the new phase which advances at the velocity of 10^{-4} m/s, interrupted by fast (the time between two acquired frame of 180 ms) transformation of large area of the sample (up to 0.5 μm^2). This behaviour repeat either while cooling (PM to FM transition) and while heating the sample (FM to PM transition). The fast advance of the front (average velocity > 4 x 10^{-3} m/s) stops at reproducible pinning sites. The analysis of the images suggested that this sites are mainly cracks which propagate in the whole volume of the sample, although some phase boundaries were also not correlated with fracture. The analysis at single pixel positions across the surface (1.67 x 1.67 μm) revealed the presence of ferromagnetic grains (α-Fe secondary phases) and micro-sized holes or non magnetic phases (La-rich phases) which influenced the slow front advancement. In this case, the magneto-static interaction among defects and magnetic phases seemed to produce a magnetic friction for the slow front. The MOIF technique showed that in La(Fe,Si)$_{13}$ based compounds two extrinsic sources of hysteresis exists: on the one side the magnetic inhomogeneities which decelerates the slow (and reversible) ferromagnetic front, on the other side the structural defects which can pin (and stop) the nucleation and growth of the fast front.

Calorimetric measurements at very low temperature scanning rate, has been compared with the MOIF results. The heat flux signals, while crossing the transition, were dominated by separated heat flux spikes, almost completely reproducible when repeating the scans. During calorimetry experiments the entire volume of the sample contributed to the measured signal, it wasn't thus possible to distinguish among local behaviours. Considering both the local (MOIF) and volume (DSC) observations, the avalanches nature of the transition may be explained by the presence of different volumes inside the sample which transform in sequence.

LOW RATE CALORIMETRY AND AVALANCHES

Further calorimetry experiments, performed to investigate the avalanches behaviour in La(Fe,Si)$_{13}$ based compounds, have been presented in Ch.5. A new series of alloys based on different amount of substitution elements in LaFe$_x$Mn$_y$Si$_z$-H$_{1.65}$ compounds was exploited with a heat flux DSC Peltier calorimeter at INRiM. The magnetic phase diagram of the series was draw, either as a function of the composition (Mn atoms) and of the applied magnetic fields. The setup was use to characterize the MCE properties of the series showing that large values of the product $\Delta S_{iso} \Delta T_{ad}$ are reached by a compromise between sufficiently first order character of the transition with high ΔS_{iso} and low hysteresis ΔT_{hys}. The increasing content of manganese atoms tunes the transition from a first to a second order behaviour, thus it has been possible to investigate the different kinetics with low temperature scanning rate experiments (1 mK/s) on sample masses smaller than 5 mg. It has been found that these two conditions are sufficient to disclose the avalanche behaviour in two alloys with different amount of Mn atoms: x = 0.30 and x = 0.18. A third alloy with x = 0.46, whose hysteresis is zero with no external applied magnetic field, was measured in the same conditions and no avalanches of heat flux were detected. The presence of avalanches was thus attributed to the first order nature of the transitions, thus to the presence of thermal hysteresis in the magnetic phase diagram of the compound. With the systematic study of the avalanches behaviour in the three compositions, the interplay between a reversible and an irreversible contributions at the FM/PM transition of La(FeSi)$_{13}$ based compounds was observed clearly when the transition was close to the critical point, thus when the character of the transition is passing from a first to a second order behaviour. It has been possible to separate two sources of heat flux, both contributing to the total entropy change at the transition. One term is due to the growth of the specific heat at the Curie point of a magnetic system and is fully reversible, the second term is a latent heat contribution and characterizes the first order nature of the transition (irreversible). The avalanches of heat flux are responsible for the irreversible term and their shape depends on the transforming fraction of volume of the sample. The specific heat term of the composition x = 0.30 increase from 750 J/kg K at zero external magnetic field to 1100 J/kg K for a magnetic field of 1.3 T. This value is close to the 1450 J/kg K of the reversible x = 0.46 composition. A general trend close to the critical point of the compound shows that the specific heat is much more smaller in first order phase transition, therefore the time constant governing the heat exchange equations is faster. Considering an AMR thermodynamic cycle, the time required to exchange the heat with the surrounding (the Peltier cell of measure in the experiment) is significantly shorter in first order phase transitions (1.8 s for x=0.18 composition in zero external magnetic field) with respect a second order transitions (2.6 s for the x = 0.46 composition in zero external magnetic field). The reversible c_p term is an intrinsic thermodynamic property of the compound and is also a parameter which governs the avalanches kinetics of the phase transitions.

Future work

The application of dedicated experimental techniques has been shown to be powerful to characterize the physical behaviour and properties at the magneto-structural phase transitions of La(Fe,Si)$_{13}$ based compounds. In summary, it has been pointed out either by the MOIF experiments and by the low rate calorimetry technique that the transition in La(Fe,Si)$_{13}$ based compounds can be difficulty separated in a full first or second order character in the vicinity of the critical point. The thermo-magnetic hysteresis can survives even with a concomitant continuous and reversible change of portion the sample, which suggests a separation of volumes inside the sample. This fact may be due to the disorder which dominates the compounds. Magnetic and structural defects, together with composition inhomogeneities of the alloys may complicate the experimental observations. However, the study of the magnetic field role, in this thesis, had produced some general guide lines on the way on which it interacts with the structure, modifying the energy landscape of the transition.

In order to continue this work, the slow dynamics (reversible c_p) may be studied in alloys with a second order phase transition by changing the defects concentration, the shape and the external conditions (magnetic fields, pressure,...). On the other hand, the fast dynamics (avalanches of heat flux) still pones several questions. The size of the volumes, whose phase abruptly transforms, may be related to some intrinsic physical parameters which experience discontinuities at the first order transition. By MOIF experiments, it was possible to observe only the behaviour of the sample at its surface, thus conclusion on volumes cannot be made, however other experimental technique may be applied to investigate this feature, i.e. in-temperature tomography reconstruction with controlled shape of the samples. By looking at the details of the heat flux avalanches shape, due to their existing close relation with thermal hysteresis, it may be expected that the time for an avalanche to start and to end critically depends on the temperature hysteresis. Further investigations need to be directed to this topic, in order to find a thermodynamic model for such shapes.

In this Ph.D. project other experimental techniques have been also tested and employed to explore magnetic phase transitions. The in-temperature measurements of physical quantities such electrical resistivity or the geometry dependency of the magnetization dynamics had furnish additional informations on the interplay among different spin structures in regions of magnetic phase diagrams where the thermal equilibrium is not satisfied. The example presented in Ch.6 of the thesis, regarded the ferromagnetic resonance (FMR) measurements in Mn_2RhSn thin film. This experiment was conducted to investigate the spin reorientation transition at 77 K of the compound, in order to individuate the interaction type between subsystems of spins which may favour the formation of skyrmion topological structures. Al thought the deviation from the main thesis subject, the described FMR setup, which has been developed during the Ph.D., may be used to exploit the ferromagnetic interaction in other classes of magnetic materials. For example, due to the rising possibility to achieve thin film of $La(Fe,Si)_{13}$ based compounds, FMR could furnish information on the magnetic anisotropy field and on the damping parameter of these compound at the transition, which still lack of literature attention.

8

Ph.D. activities and publications

Schools

[1] **Scuola Nazionale SCS SCIENZA, COMUNICAZIONE, SOCIETÁ, Il ricercatore visibile: Strumenti per comunicare la scienza**, promoted by Agorà Scienza, Pollenzo (CN), September 1-6, 2013 at Università degli Studi di Scienze Gastronomiche.

[2] **School on Magnetic Materials for Energy Applications**, promoted by the Italian Association of Magnetism (AIMagn), Parma, February 11th-14th, 2014 at IMEM-CNR Institute.

[3] **Marie Curie School on Spintronic: theory, devices and applications** organized by Paris Sud University and the Marie Curie Initial Training Network "WALL" and funded by Marie Curie Actions within the Seventh Framework Program from the European Commission. Parigi, September 16th-18th, 2014 at Réfectoire des Cordeliers.

Conferences and workshop

[1] **DRREAM 24-month progress meeting**, promoted by DRREAM [1], a collaborative research project funded by the EC under the Seventh Framework Programme, Torino, January, 22-23, 2015 at INRiM.

Oral presentation: CALORIMETRIC STUDY OF THE MAGNETOCALORIC COMPOUNDS $\mathrm{LaFe}_x\mathrm{Mn}_y\mathrm{Si}_z\text{-}\mathrm{H}_{1.65}$ NEAR THE CRITICAL POINT C. Bennati, G. Ghigo, F. Laviano, M. Kuepferling and V. Basso

[2] **MAGNET 2015**, promoted by the Italian Association of Magnetism (AIMagn), Bologna, February, 17-19, 2015 at IMEM-CNR Institute.

Poster presentation: ELECTRICAL AND CALORIMETRIC STUDY AT THE TRANSITIONS OF THE MAGNETO-CALORIC COMPOUNDS $\mathrm{LaFe}_x\mathrm{Mn}_y\mathrm{Si}_z\text{-}\mathrm{H}_{1.65}$ C.Bennati, V.Basso, L.Gozzelino, M.Kuepferling, F.Laviano, G.Ghigo

[3] **International Conference on Magnetism, ICM2015** Barcellona, July 5th to 10th, 2015.

Oral presentation: LOCAL MAGNETIC BEHAVIOR ACROSS THE FIRST ORDER PHASE TRANSITION OF THE $\mathrm{La(Fe}_{0.9}\mathrm{Co}_{0.015}\mathrm{Si}_{0.085})_{13}$ MAGNETO CALORIC COMPOUND. C. Bennati, G. Ghigo, V. Basso, E. Olivetti, M. Kuepferling and F. Laviano

Poster presentation: TEMPERATURE DEPENDENCE OF THE FERROMAGNETIC RESONANCE AT THE SPIN REORIENTATION TRANSITION OF MN2RHSN THIN FILMS C. Bennati, A. Caprile, O. Meshcheriakova, C. Felser, G.Ghigo, M.Coisson and M.Pasquale

[4] **Delft Days on Magnetocalorics (DDM2015)** organized by TU Delft Univesity of Technology in collaboration with BASF New Business GmbH. Delft, November 02-03, 2015 at Science Centre Delft.

Oral presentation: TEMPERATURE HYSTERESIS AND LATENT HEAT AVALANCHES IN $\mathrm{LaFe}_x\mathrm{Mn}_y\mathrm{Si}_z\text{-}\mathrm{H}_{1.65}$ C. Bennati, G. Ghigo, L. Gozzelino, F. Laviano, M.Kuepferling and V. Basso

List of pubblications

[1] M. Kuepferling, C. Bennati, F. Laviano, G. Ghigo, V. Basso, **Dynamics of the magneto structural phase transition in La($Fe_{0.9}Co_{0.015}Si_{0.085}$)$_{13}$ observed by magneto-optical imaging**. Journal of Applied Physics, 115.17 (2014) 17A925.

We investigate the temperature induced ferromagnetic to paramagnetic phase transition in Co substituted La($Fe_xCo_ySi_{1-x-y}$)$_{13}$ with x=0.9 and low Co content of y = 0.015 ($T_c \sim$ 200 K) by means of magneto optical imaging with indicator film and by calorimetry at very low temperature rates. We were able to visualize the motion of the ferromagnetic (FM)/paramagnetic (PM) front which is forming reproducible patterns independently of the temperature rate. The average velocity of the FM/PM front was calculated to be 10^{-4} m/s during the continuous propagation and 4 10^{-3} m/s during an avalanche. The heat flux was measured at low temperature rates by a differential scanning calorimeter and shows a reproducible sequence of individual and separated avalanches which occurs independently of the rate. We interpret the observed effects as the results of the a thermal character of the phase transition.

[2] C. Bennati, F. Laviano, G. Durin, E.S. Olivetti, V. Basso, G. Ghigo and M. Kuepferling, **Local magnetic behaviour across the first order phase transition in La($Fe_{0.9}Co_{0.015}Si_{0.085}$)$_{13}$ magneto caloric compound**, Journal of Magnetism and Magnetic Materials 400 (2015) 339-343

We visualize, with a magneto optical imaging technique with indicator film, the local magnetic response of the compound La($Fe_{0.9}Co_{0.015}Si_{0.085}$)$_{13}$ during its first order magneto structural transition. The technique allowed us by comparing the stray fields of the main magneto caloric phase and of secondary phases present in the sample to obtain the magnetic behavior of each phase above and below the Curie temperature with respect to the surrounds. Computing the change in the total magnetic flux, when the sample crosses the Curie point, both in cooling and heating, we are able to correlate the average thermal hysteresis of the transition with the local magnetic properties at single sites and analyze the influence of defects on the transition dynamics.

[3] M. Piazzi, C. Curcio, C. Bennati, M. Kuepferling, V. Basso, **Modeling specific heat and entropy change in La(Fe–Mn–Si)13–H compounds**, Journal of Magnetism and Magnetic Materials 400 (2015) 349-355

In this paper we model the magnetocaloric effect of LaFexMnySiz–H1.65 compound (x+y+z=13), a system showing a transition temperature finely tunable around room temperature by Mn substitution. The thermodynamic model takes into account the coupling between magnetism and specific volume as introduced by Bean and Rodbell. We find a good qualitative agreement between experimental and modeled entropy change -Δs(H,T). The main result is that the magnetoelastic coupling drives the phase transition of the system, changing it from second to first order by varying *a model parameter η. It is also responsible for a decrease of -Δs at the transition, due to a small lattice contribution to the entropy counteracting the effect of the magnetic one. The role of Mn is reflected exclusively in a decrease of the strength of the exchange interaction, while the value of the coefficient β, responsible for the coupling between volume and exchange energy, is independent on the Mn content and it appears to be an intrinsic property of the La(Fe–Si)13 structure.*

[4] V. Basso, M. Kuepferling, C. Curcio, C. Bennati, A. Barzca, M. Katter, M. Bratko, E. Lovell, J. Turcaud, L.F. Cohen, **Specific heat and entropy change at the first order phase transition of La(Fe-Mn-Si)13-H compounds**, Journal of Applied Physics, 118.5 (2015) 053907.

In this paper, we present the results of an experimental investigation on the magnetocaloric properties of hydrogenated La(Fe-Mn-Si)13-H with Mn substituting Fe to finely tune the transition temperature. We measured the specific heat under magnetic field c_p(H, T) and the magnetic field induced isothermal entropy change Δs(H, T) of a series of compounds by direct Peltier calorimetry. Results show that increasing Mn from 0.06 to 0.46 reduces the transition temperature from 339 K to 270 K whilst the total entropy change due to a 1.5 T field is depressed from 18.7 J kg-1K-1 to 10.2 Jkg-1K-1 and the thermal hysteresis similarly is reduced from 1.5 K to zero. In the paper, we interpret the results in terms of a magnetic phase transition changing from the first to the second order with increasing Mn content, and we discuss the value of the results for magnetic cooling applications.

[5] C. Bennati, G. Ghigo, L. Gozzelino, M. Kuepferling and V. Basso, **Hysteresis and avalanches in the magnetocaloric compounds $\mathbf{LaFe_xMn_ySi_z\text{-}H_{1.65}}$ near the critical point**, submitted paper (2015).

The effect of substitution elements and of applied magnetic fields on the nature and on the dynamics of the phase transition in La(Fe,Si)$_{13}$ based compounds is investigated through a low rates differential scanning calorimetric technique and electrical resistivity measurements in the series of the magnetocaloric candidates $LaFe_xMn_ySi_z\text{-}H_{1.65}$. The transition from a low temperature ferromagnetic phase to a high temperature paramagnetic phase can be tuned both by the magnetic field and by the amount of manganese atoms from the first to the second order. In the calorimetric measurements we show that, when the transition is of first order, the growth of the new phase is accompanied by heat flux avalanches which reflect the absorption/release of latent heat at the transitions. As the transition approaches the critical point, the avalanche peaks modify and gradually disappear, moreover their shape reveals the growth of the specific heat, up to 150% at the critical field, which counts for the reversible exchange of heat of second order phase transitions. On the basis of that, a competition between irreversible/reversible processes is established depending on the energy barrier between the ferromagnetic/paramagnetic phases. As the two phases possess different electrical properties, the change from step-like to smooth transition is reflected also in the electrical resistance dependence on the temperature and on the magnetic field, the latter is responsible of the increase from 3.7% to 5% of the magnetoresistance at the transition.

Bibliography

[1] European Union Seventh Framework Programme for Research (FP7). *Drastically Reduced use of Rare Earths in$_Applications of Magnetocalorics$*. Jan. 2013. URL: `http://www.drream.eu/Drastically_Reduced_use_of_Rare_Earths_in_Applications_of_Magnetocalorics.html`.

[2] Toshiba Corp Chubu Electric Power Co. *Magnetic freezing system developed A world-first, next-generation freezing technology that uses no CFCs is developed*. Jan. 2000. URL: `http://www.chuden.co.jp/english/corporate/rd/20001003_1.html`.

[3] Camfridge. *The second generation magnetic cooling engine achievements*. Aug. 2015. URL: `http://www.camfridge.com`.

[4] Cooltech. *Magnetic Refrigeration System*. Jan. 2015. URL: `http://www.cooltech-applications.com/magnetic-refrigeration-system.html`.

[5] Andrej Kitanovskia, Jaka Tusekb, and Alojz Poredosc. *Magnetocaloric Energy Conversion*. 2015.

[6] BASF. *Premiere of cutting-edge cooling appliance at CES 2015*. Jan. 2015. URL: `https://www.basf.com/en/company/news-and-media/news-releases/2015/01/p-15-100.html`.

[7] KA Gschneidner and VK Pecharsky. "Thirty years of near room temperature magnetic cooling: Where we are today and future prospects". In: *International journal of refrigeration* 31.6 (2008), pp. 945–961.

[8] DJ Silva et al. "Solid state magnetic refrigerator". In: *Applied Energy* 93 (2012), pp. 570–574.

[9] Jian Liu et al. "Giant magnetocaloric effect driven by structural transitions". In: *Nature materials* 11.7 (2012), pp. 620–626.

[10] K Fukamichi, A Fujita, and S Fujieda. "Large magnetocaloric effects and thermal transport properties of La (FeSi) 13 and their hydrides". In: *Journal of alloys and compounds* 408 (2006), pp. 307–312.

[11] Meghmalhar Manekar and SB Roy. "Reproducible room temperature giant magnetocaloric effect in Fe–Rh". In: *Journal of Physics D: Applied Physics* 41.19 (2008), p. 192004.

[12] Vitalij K Pecharsky and Karl A Gschneidner Jr. "Giant magnetocaloric effect in Gd 5 (Si 2 Ge 2)". In: *Physical Review Letters* 78.23 (1997), p. 4494.

[13] Sindhunil Barman Roy. “First order magneto-structural phase transition and associated multi-functional properties in magnetic solids”. In: *Journal of Physics: Condensed Matter* 25.18 (2013), p. 183201.

[14] Herbert B Callen. *Thermodynamics & an Intro. to Thermostatistics*. John wiley & sons, 2006.

[15] CP Bean and DS Rodbell. “Magnetic disorder as a first-order phase transformation”. In: *Physical Review* 126.1 (1962), p. 104.

[16] A Fujita, Y Akamatsu, and K Fukamichi. “Itinerant electron metamagnetic transition in La (FexSi1-x) 13 intermetallic compounds”. In: *Journal of Applied Physics* 85 (1999), pp. 4756–4758.

[17] Feng-xia Hu et al. “Magnetic entropy change in La (Fe0. 98Co0. 02) 11.7 Al1. 3”. In: *Journal of Physics: Condensed Matter* 12.46 (2000), p. L691.

[18] Hu Feng-Xia et al. “Great magnetic entropy change in La (Fe, M) 13 (M= Si, Al) with Co doping”. In: *Chinese Physics* 9.7 (2000), p. 550.

[19] S Fujieda, A Fujita, and K Fukamichi. “Large magnetocaloric effect in La (Fe x Si 1-x) 13 itinerant-electron metamagnetic compounds”. In: *Applied Physics Letters* 81.7 (2002), pp. 1276–1278.

[20] Edmund Lovell et al. “Dynamics of the First-Order Metamagnetic Transition in Magnetocaloric La (Fe, Si) 13: Reducing Hysteresis”. In: *Advanced Energy Materials* 5.6 (2015).

[21] Julia Lyubina. “Recent advances in the microstructure design of materials for near room temperature magnetic cooling (invited)”. In: *Journal of Applied Physics* 109.7, 07A902 (2011), pp. –.

[22] Jian Liu et al. “Systematic study of the microstructure, entropy change and adiabatic temperature change in optimized La–Fe–Si alloys”. In: *Acta Materialia* 59.9 (2011), pp. 3602–3611.

[23] Feng-xia Hu et al. “Influence of negative lattice expansion and metamagnetic transition on magnetic entropy change in the compound LaFe11.4Si1.6”. In: *Applied Physics Letters* 78.23 (2001), pp. 3675–3677.

[24] A Fujita et al. “Itinerant-electron metamagnetic transition and large magnetovolume effects in La (Fe x Si 1- x) 13 compounds”. In: *Physical Review B* 65.1 (2001), p. 014410.

[25] ME Gruner et al. “Element-Resolved Thermodynamics of Magnetocaloric LaFe 13- x Si x”. In: *Physical review letters* 114.5 (2015), p. 057202.

[26] Francesco Laviano et al. “An improved method for quantitative magneto-optical analysis of superconductors”. In: *Superconductor Science and Technology* 16.1 (2003), p. 71.

[27] Vittorio Basso et al. “Specific heat and entropy change at the first order phase transition of La (Fe-Mn-Si) 13-H compounds”. In: *Journal of Applied Physics* 118.5 (2015), p. 053907.

[28] Christopher Jarzynski. “Diverse phenomena, common themes”. In: *Nature Physics* 11.2 (2015), pp. 105–107. ISSN: 1745-2473.

[29] H Eugene Stanley. "Introduction to phase transitions and critical phenomena". In: *Oxford University Press* 1 (1987).

[30] John MD Coey. *Magnetism and magnetic materials*. Cambridge University Press, 2010.

[31] Giorgio Bertotti. *Hysteresis in magnetism: for physicists, materials scientists, and engineers*. Academic press, 1998.

[32] Aleksandr M Tishin and Youry I Spichkin. *The magnetocaloric effect and its applications*. CRC Press, 2003.

[33] Mark Waldo Zemansky and Richard H Dittman. *Heat and thermodynamics*. McGraw-Hill, 1997.

[34] E Brück et al. "Magnetocaloric refrigeration near room temperature". In: *Journal of Magnetism and Magnetic Materials* 310.2 (2007), pp. 2793–2799.

[35] C Zimm et al. "Design and performance of a permanent-magnet rotary refrigerator". In: *International journal of refrigeration* 29.8 (2006), pp. 1302–1306.

[36] Steven L Russek and Carl B Zimm. "Potential for cost effective magnetocaloric air conditioning systems". In: *International Journal of Refrigeration* 29.8 (2006), pp. 1366–1373.

[37] BF Yu et al. "Review on research of room temperature magnetic refrigeration". In: *International Journal of Refrigeration* 26.6 (2003), pp. 622–636.

[38] Karl A GschneidnerJr, VK Pecharsky, and AO Tsokol. "Recent developments in magnetocaloric materials". In: *Reports on Progress in Physics* 68.6 (2005), p. 1479.

[39] GV Brown. "Magnetic heat pumping near room temperature". In: *Journal of Applied Physics* 47.8 (1976), pp. 3673–3680.

[40] Vitalij K Pecharsky and KA Gschneidner. "Gd5 (SixGe1-x) 4: An extremum material". In: *Advanced Materials* 13.9 (2001), pp. 683–686.

[41] AO Pecharsky et al. "The room temperature metastable/stable phase relationships in the pseudo-binary Gd5Si4–Gd5Ge4 system". In: *Journal of alloys and compounds* 338.1 (2002), pp. 126–135.

[42] Ekkes Brück. "Developments in magnetocaloric refrigeration". In: *Journal of Physics D: Applied Physics* 38.23 (2005), R381.

[43] M Kuepferling, CP Sasso, and V Basso. "Rate dependence of the magnetocaloric effect in La-Fe-Si compounds". In: *EPJ Web of Conferences*. 2013.

[44] XX Zhang et al. "Magnetic entropy change in Fe-based compound LaFe10. 6Si2. 4". In: *Applied physics letters* 77.19 (2000), pp. 3072–3074.

[45] TTM Palstra et al. "Study of the critical behaviour of the magnetization and electrical resistivity in cubic La (Fe, Si) 13 compounds". In: *Journal of magnetism and magnetic materials* 36.3 (1983), pp. 290–296.

[46] Chen Yuan-Fu et al. "Large magnetic entropy change near room temperature in the LaFe11. 5Si1. 5H1. 3 interstitial compound". In: *Chinese Physics* 11.7 (2002), p. 741.

[47] PI Kripyakevich, OS Zarechnyuk, and EI Gladyshevsky. "0. I. Bodak". In: *Z. Anorg. Chem* 358 (1968), p. 90.

[48] BG Shen et al. "Recent progress in exploring magnetocaloric materials". In: *Advanced Materials* 21.45 (2009), pp. 4545–4564.

[49] Matthias Katter et al. "Magnetocaloric Properties of Bulk Material Prepared by Powder Metallurgy". In: *Magnetics, IEEE Transactions on* (2008).

[50] Julia Lyubina et al. "La (Fe, Si) 13-based magnetic refrigerants obtained by novel processing routes". In: *Journal of Magnetism and Magnetic Materials* 321.21 (2009), pp. 3571–3577.

[51] A Barcza et al. "Stability and Magnetocaloric Properties of Sintered La (Fe, Mn, Si) H Alloys". In: *Magnetics, IEEE Transactions on* 47.10 (2011), pp. 3391–3394.

[52] Zsolt Gercsi. "Magnetic coupling in transition-metal–doped LaSiFe11. 5 TM0. 5 (TM= Cr, Mn, Co and Ni)". In: *EPL (Europhysics Letters)* 110.4 (2015), p. 47006.

[53] Maria Krautz et al. "Systematic investigation of Mn substituted La(Fe,Si)$_{13}$ alloys and their hydrides for room-temperature magnetocaloric application". In: *Journal of Alloys and Compounds* 598.0 (2014), pp. 27 –32. ISSN: 0925-8388.

[54] Kelly Morrison and Lesley F Cohen. "Overview of the Characteristic Features of the Magnetic Phase Transition with Regards to the Magnetocaloric Effect: the Hidden Relationship Between Hysteresis and Latent Heat". In: *Metallurgical and Materials Transactions E* 1.2 (2014), pp. 153–159.

[55] JD Moore et al. "Reducing the operational magnetic field in the prototype magnetocaloric system Gd5Ge4 by approaching the single cluster size limit". In: *Applied physics letters* 88.7 (2006), p. 072501.

[56] JD Moore et al. "Reducing extrinsic hysteresis in first-order La (Fe, Co, Si) 13 magnetocaloric systems". In: *Applied Physics Letters* 95.25 (2009), p. 252504.

[57] FX Hu et al. "Particle size dependent hysteresis loss in La0. 7Ce0. 3Fe11. 6Si1. 4C0. 2 first-order systems". In: *Applied Physics Letters* 100.7 (2012), p. 072403.

[58] Julia Lyubina. "Recent advances in the microstructure design of materials for near room temperature magnetic cooling". In: *Journal of Applied Physics* 109.7 (2011), 07A902.

[59] Anja Waske et al. "Asymmetric first-order transition and interlocked particle state in magnetocaloric La (Fe, Si) 13". In: *physica status solidi (RRL)-Rapid Research Letters* 9999 (2015).

[60] H Saito, T Yokoyama, and K Fukamichi. "Itinerant-electron metamagnetism and the onset of ferromagnetism in Laves phase compounds". In: *Journal of Physics: Condensed Matter* 9.43 (1997), p. 9333.

[61] A Fujita et al. "Itinerant-electron metamagnetic transition and large magnetocaloric effects in La (Fe x Si 1- x) 13 compounds and their hydrides". In: *Physical Review B* 67.10 (2003), p. 104416.

[62] L Jia et al. "Influence of interstitial and substitutional atoms on the crystal structure of La (FeSi) 13". In: *Journal of Alloys and Compounds* 509.19 (2011), pp. 5804–5809.

[63] Marco Piazzi et al. "Modeling specific heat and entropy change in La (Fe–Mn–Si) 13–H compounds". In: *Journal of Magnetism and Magnetic Materials* 400 (2015), pp. 349–355.

[64] Francis Bitter. "On inhomogeneities in the magnetization of ferromagnetic materials". In: *Physical review* 38.10 (1931), p. 1903.

[65] Alex Hubert and Rudolf Schäfer. *Magnetic domains: the analysis of magnetic microstructures*. Springer Science & Business Media, 2008.

[66] Rostislav Grechishkin et al. "Magnetic imaging films". In: *Magnetic Nanostructures in Modern Technology*. Springer, 2008, pp. 195–224.

[67] Michael Faraday. "Experimental researches in electricity. Nineteenth series". In: *Philosophical Transactions of the Royal Society of London* 136 (1846), pp. 1–20.

[68] Francesco Laviano. "Magneto-optics: Imaging and Quantitative Analysis". PhD thesis. Politecnico di Torino, 2005.

[69] Nobuyasu Adachi et al. "Synthesis of Bi–Lu-Substituted Iron Garnet Films for Visualization of Magnetic Flux in High-Tc Superconductors". In: *Japanese journal of applied physics* 41.10R (2002), p. 5986.

[70] LE Helseth. "Theoretical model for magnetooptic imaging". In: *arXiv preprint cond-mat/0201494* (2002).

[71] Naoyuki Kawamoto et al. "In Situ TEM Observation of Thermally-Induced First-Order Magnetic Transition in Itinerant-Electron Metamagnetic La (FexSi1-x) 13 Compounds". In: *Materials transactions* 46.8 (2005), pp. 1764–1767.

[72] N Kawamoto et al. "Magnetic domains in a metamagnetic La (Fe0. 90Si0. 10) 13 refrigerant". In: *Journal of applied physics* 100.4 (2006), p. 3913.

[73] N Kawamoto et al. "Magnetic domain analysis by in-situ TEM observation of magnetic refrigerant La (Fe 0.90 Si 0.10) 13". In: *Journal of Magnetism and Magnetic Materials* 310.2 (2007), pp. 2815–2817.

[74] V Lollobrigida et al. "Chemical, electronic, and magnetic structure of LaFeCoSi alloy: Surface and bulk properties". In: *Journal of Applied Physics* 115.20 (2014), p. 203901.

[75] K Morrison et al. "Capturing first-and second-order behavior in magnetocaloric CoMnSi 0.92 Ge 0.08". In: *Physical Review B* (2009).

[76] C Bennati et al. “Local magnetic behavior across the first order phase transition in La (Fe0. 9Co0. 015Si0. 085) 13 magneto caloric compound”. In: *Journal of Magnetism and Magnetic Materials* (2015).

[77] Xiang Chen, Yungui Chen, and Yongbo Tang. “High-temperature phase transition and magnetic property of LaFe 11.6 Si 1.4 compound”. In: *Journal of Alloys and Compounds* (2011).

[78] LA Dorosinskii et al. “Studies of HTSC crystal magnetization features using indicator magnetooptic films with in-plane anisotropy”. In: *Physica C: Superconductivity* (1992).

[79] M Kuepferling et al. “Dynamics of the magneto structural phase transition in La (Fe0. 9Co0. 015Si0. 085) 13 observed by magneto-optical imaging”. In: *Journal of Applied Physics* 115.17 (2014), 17A925.

[80] F. X. Hu et al. “Magnetic entropy change and its temperature variation in compounds La(Fe1âÂÂxCox)11.2Si1.8”. In: *Journal of Applied Physics* 92.7 (2002), pp. 3620–3623.

[81] Fang Wang et al. “The effect of Mn substitution in LaFe 11.7 Si 1.3 compound on the magnetic properties and magnetic entropy changes”. In: *Journal of Physics D: Applied Physics* 36.1 (2003), p. 1.

[82] Vittorio Basso, Carlo Paolo Sasso, and Michaela Kpferling. “A Peltier cells differential calorimeter with kinetic correction for the measurement of cp(H,T) and of magnetocaloric materials”. In: *Review of Scientific Instruments* 11 (), pp. –.

[83] K Morrison et al. “Contributions to the entropy change in melt-spun LaFe 11.6 Si 1.4”. In: *Journal of Physics D: Applied Physics* 45.17 (2012), p. 179501.

[84] Song Sun et al. “Effect of Mn Substitution on Microstructure Evolution and Magnetic Phase Transition in La (Fe1- x Mn x) 10.8 Co0. 7Si1. 5 Compounds”. In: *Metallurgical and Materials Transactions A* 44.13 (2013), pp. 5782–5787.

[85] Olga Meshcheriakova. “Noncollinear magnetism in Mn2RhSn Heusler compound”. eng. PhD thesis. Johannes Gutenberg-Universitat, 2014.

[86] IA Campbell and A Fert. “Transport properties of ferromagnets”. In: *Ferromagnetic materials* 3 (1982), pp. 747–804.

[87] Uichiro Mizutani. *Introduction to the electron theory of metals*. Cambridge University Press, 2001.

[88] Hu Feng-Xia et al. “Magnetoresistances and magnetic entropy changes associated with negative lattice expansions in NaZn13-type compounds LaFeCoSi”. In: *Chinese Physics* 14.11 (2005), p. 2329.

[89] FX Hu et al. “Magnetoresistance in LaFe 11.2 Co 0.7 Si 1.1 compound”. In: *Magnetics, IEEE Transactions on* 40.4 (2004), pp. 2754–2756.

[90] TTM Palstra et al. “Study of the critical behaviour of the magnetization and electrical resistivity in cubic La (Fe, Si) 13 compounds”. In: *Journal of magnetism and magnetic materials* 36.3 (1983), pp. 290–296.

[91] M Viard and G Gavoille. “Anomalous critical behaviour of the electrical resistivity of iron-platinum invar alloys”. In: *Journal of Applied Physics* 50.B3 (1979), pp. 1828–1830.

[92] Nevill Francis Mott and Harry Jones. *The theory of the properties of metals and alloys*. Courier Corporation, 1958, pp. 271–272.

[93] Walter Barry. “A broad-band, automated, stripline technique for the simultaneous measurement of complex permittivity and permeability”. In: *Microwave Theory and Techniques, IEEE Transactions on* 34.1 (1986), pp. 80–84.

[94] Sangita S Kalarickal et al. “Ferromagnetic resonance linewidth in metallic thin films: Comparison of measurement methods”. In: *Journal of Applied Physics* 99.9 (2006), p. 093909.

[95] Claus Bilzer. “Microwave susceptibility of thin ferromagnetic films: metrology and insight into magnetization dynamics”. PhD thesis. Université Paris Sud-Paris XI, 2007.

[96] O. Meshcheriakova et al. “Large Noncollinearity and Spin Reorientation in the Novel Mn 2 RhSn Heusler Magnet”. In: *Physical Review Letters* 113.8 (2014). ISSN: 1079-7114.

[97] I. Dzyaloshinsky. “A thermodynamic theory of “weak” ferromagnetism of antiferromagnetics”. In: *Journal of Physics and Chemistry of Solids* 4 (1958), pp. 241–255.

[98] T. Moriya. “Anisotropic Superexchange Interaction and Weak Ferromagnetism”. In: *Physical Review* 120 (Oct. 1960), pp. 91–98.

[99] Albert Fert, Vincent Cros, and João Sampaio. “Skyrmions on the track”. In: *Nature nanotechnology* 8.3 (2013), pp. 152–156.

[100] Structural, electronic, and magnetic properties of perpendicularly magnetised Mn2RhSn thin. “Home Search Collections Journals About Contact us My IOPscience”. In: 2015.

[101] Michael Farle. “Ferromagnetic resonance of ultrathin metallic layers”. In: *Reports on Progress in Physics* 61.7 (1998), p. 755.

[102] T. Schwarze et al. “Universal helimagnon and skyrmion excitations in metallic, semiconducting and insulating chiral magnets”. In: *Nature Materials* 14.5 (2015), 478???483. ISSN: 1476-4660.

[103] Ambra Caprile et al. “Microwave Properties and Damping in [Pt/Co] Multilayers With Perpendicular Anisotropy”. In: *Magnetics Letters, IEEE* 5 (2014), pp. 1–4.